UC San Diego

UC San Diego Electronic Theses and Dissertations

Title

Investigation of the limits of broadband robust matched- field processing

Permalink

https://escholarship.org/uc/item/9f69q80f

Author

Debever, Claire

Publication Date

2011

Peer reviewed|Thesis/dissertation

eScholarship.org Powered by the California Digital Library
University of California

UNIVERSITY OF CALIFORNIA, SAN DIEGO

Investigation of the limits of broadband robust matched-field processing

A dissertation submitted in partial satisfaction of the
requirements for the degree
Doctor of Philosophy

in

Oceanography

by

Claire Debever

Committee in charge:

William A. Kuperman, Chair
Michael J. Buckingham
William A. Coles
Bruce D. Cornuelle
William S. Hodgkiss
Heechun Song

2011

Copyright
Claire Debever, 2011
All rights reserved.

The dissertation of Claire Debever is approved, and it is acceptable in quality and form for publication on microfilm and electronically:

_____

_____

_____

_____

_____

_____

Chair

University of California, San Diego

2011

DEDICATION

To my family...

TABLE OF CONTENTS

LIST OF FIGURES

ACKNOWLEDGEMENTS

I would like to thank my advisor, Professor William A. Kuperman for his kind guidance and endless patience throughout my Ph. D. work. I am very grateful for his continuous support, wealth of great ideas and unequaled humor, making this journey a truly pleasant one. I genuinely hope that I can one day be the caring, available and inspirational advisor that he is.

I am also thankful to my committee members, Professor William S. Hodgkiss, Dr. Heechun C. Song, Professor Michael J. Buckingham, Dr. Bruce D. Cornuelle and Professor William A. Coles for their valuable comments and time.

I would like to thank everybody at the Marine Physical Laboratory, and my fellow graduate students for creating such a wonderful work environment. I wish to express a very special "thank you" to Evelyn Doudera who not only resolved any administrative problem along the way with astonishing efficiency, but also wisely discovered that the best cure to any research set back is a slice or two of chocolate cake. Please do not disclose I might have taken seconds.

I am also deeply grateful to Nicholas Gilbert, Jeannie Pan, Naseem Kerendian, Cecilia Aparis, Benjamin Maurer and his whole family for their affection and support throughout my thesis.

Finally, I would like to dedicate this work to my family, my parents and sisters, without whom it would not have been possible to write this doctoral thesis. I am very appreciative for their understanding and endless encouragements.

This work was supported by the Office of Naval Research under Contract No. N00014-06-1-0198.

This dissertation is a collection of papers that were published or about to be submitted for publication. The text of chapter Three is in full a reprint of the of the material as it appears in Claire Debever and William A. Kuperman, "Robust matched-field processing using a coherent broadband white noise constraint processor", J. Acoust. Soc. Am., vol. 122, Number 4, pp. 1979-1986.

The text of Chapter Four is in full a reprint of the material soon to be submitted to the J. Acoust. Soc. Am., Claire Debever, William A. Kuperman and William S. Hodgkiss, "Fully coherent matched-field processing using a source

phase estimation technique".

The text of Chapter Five is in full a reprint of the material soon to be submitted to the J. Acoust. Soc. Am., Claire Debever and William A. Kuperman "Mitigating the effect of environmental fluctuations on higher frequency matched-field processing".

The dissertation author was the primary researcher and author, and the co-authors listed in these publications directed and supervised the research which forms the basis of this dissertation.

VITA

2003	M. S. in Physics - wave physics, micro-electronic, mechanical and fluid mechanics, applied mathematics, Ecole Superieur de Physique et de Chimie Industrielle, Paris, France
2011	Ph. D. in Oceanography, University of California, San Diego, CA
Feb. - May 2002	Intern at the Laboratoire d'Ondes et Acoustique (LOA) of Paris.
Jun. - Dec 2002	Research assistant at NOAA's Southwest Fisheries Science Center, La Jolla, CA
2003-2010	Graduate Student Research Associate Marine Physical Laboratory, Scripps Institution of Oceanography, University of California, San Diego, CA

PUBLICATIONS

Journals

1. Claire Debever and W. A. Kuperman, Robust matched-field processing using a coherent broadband white noise constraint processor, *J. Acoust. Soc. Am.*, vol. 122, number 4, pp. 1979-1986, October 2007.
2. Julien de Rosny, Claire Debever, Stephane Conti and Philippe Roux, Diffuse reverberant acoustic wave spectroscopy with absorbing scatterers, *Applied Physics Letters*, vol. 87, issue 15, 2005.

Conferences

1. Claire Debever and W. A. Kuperman, Exploring the limits of matched-field processing, *J. Acoust. Soc. Am.*, vol. 128, number 4, October 2010.
2. Claire Debever and W. A. Kuperman, Broadband high frequency matched-field processing, *J. Acoust. Soc. Am.*, vol. 124, number 4, October 2008.
3. Claire Debever and W. A. Kuperman, Effect of array element location on coherent inter-array processing, *J. Acoust. Soc. Am.*, vol. 123, number 5, May 2008.
4. Claire Debever and W. A. Kuperman, Broadband, coherent inter-array processing of horizontal arrays, *J. Acoust. Soc. Am.*, vol. 122, number 5, November 2007.

5. Claire Debever and W. A. Kuperman, Coherent-broadband, white noise constraint, matched-field processing, *J. Acoust. Soc. Am.*, vol. 121, number 5, May 2007.

6. Claire Debever and W. A. Kuperman, Higher Frequency matched-field processing, *J. Acoust. Soc. Am.*, vol. 120, number 5, November 2006.

ABSTRACT OF THE DISSERTATION

Investigation of the limits of broadband robust matched-field processing

by

Claire Debever

Doctor of Philosophy in Oceanography

University of California, San Diego, 2011

William A. Kuperman, Chair

Localizing and tracking underwater targets is of interest to the study of sound emitting marine life, physical or chemical phenomena affecting acoustic wave's propagation or to naval SONARS, to cite a few applications. Matched-field processing (MFP) is a passive localization method based on comparing the pressure fields received on an hydrophone array with synthesized fields coming from hypothetical source locations. The best match between modeled and received signals yields an estimate of the source's position. Successful localization requires a number of conditions to be met. Low-frequency, loud signals propagating in a steady well studied environment without presence of loud interferers have been tracked over tens to hundreds of kilometers in the literature.

This dissertation addresses MFP's localization and tracking performance at low signal-to-noise ratios, in the presence of environmental mismatch between modeled and real propagating environments and/or for high frequency scenarios. The issue of robustness and snapshot deficiency are addressed by implementing the white noise constraint adaptive processor. Throughout most of the dissertation, a comparison between conventional, minimum variance distortionless response and white noise constraint algorithms' localization performance is provided.

Broadband algorithms, processing frequencies both in a coherent and incoherent way are introduced to enhance MFP's ability to detect low signal-to-noise ratio sources. A technique to estimate and include the unknown source phase to the processing is developed, and the extra-gain it provides is determined.

The enhanced sensitivity of MFP to environmental variability in high-frequency scenarios is investigated using data emitted from multiple sources to create replica vectors. A combination of robust adaptive MFP using the white noise constraint method and coherent broadband processing was shown to yield promising localization results in high-frequency scenarios for which MFP is typically problematic.

Chapter 1

Introduction

Understanding sound propagation in a media has received considerable attention over the last fifty years and shown to be a valuable tool in a wide array of disciplines ranging from biomedical [1, 2, 3, 4, 5], quality control [6, 7], communication [8, 9, 10] and astrophysics [11, 12, 13], to name a few. Typically, an array of sensors is deployed in or on the media and its output signal is processed using knowledge of the environment and a propagation model to infer parameters of interest. Since sound waves undergo much less dissipation than electromagnetic ones in the water, acoustic naturally imposed itself as the method of choice to communicate or study underwater phenomena [14, 15].

One important area of interest is the inverse problem of source detection, characterization and localization. Beamforming methods were developed to estimate the angle of arrival of a signal [16, 17, 18]. The array is "steered" in a particular look direction by modeling an incoming plane wave signal at that angle. The best match between various impinging angles and the received pressure field yields an estimate of the source direction. In the ideal case of perfect knowledge of the environment, the phases of the signal's Fourier transform at the frequency of interest match the ones of the synthetic plane wave at each element only when the array is steered in the true source direction. The sum of the phase-corrected elements' response consequently reaches its maximum value, corresponding to a peak in a beamformer power versus angle-of-arrival plot. A number of signal processing techniques, called adaptive in that they incorporate the signal itself in the modeling of the synthetic field are available to improve the signal's detectability by widening the main lobe, lowering the sidelobe level and canceling out interfering signals [19, 20, 21, 22, 23].

Plane wave beamforming has been shown to experimentally detect acoustic sources in somewhat simple, uniform, unbounded environments [24, 25, 26]. But because of the presence of the reflective air/water/sediment interfaces, the ocean is a bounded acoustic waveguide in which sound propagation from source to sensors is altered by reflection, refraction and scattering. In effect, the wavefront is distorted and plane wave picture is modified by multipath phenomena. Matched-field processing (MFP) is a generalization from plane wave beamforming in which

the complexity of the full field structure is taken into account in the propagation model, and therefore exploited to better detect the source this time in range, depth and azimuth [27, 28]. The array output can be visualized as a color plot of power versus range and depth for fixed azimuth, called the ambiguity surface. The main peak gives an estimate of the expected position of the source. Adaptive techniques translate directly from plane wave beamforming to MFP.

Matched-field processing in realistic environments, being more often than not complicated but somewhat predictable, can be used as a way to localize sources but also infer information about the oceanic waveguide itself such as sound speed profile or seafloor parameters [29, 30, 31]. The process can be done passively, meaning that it uses the sound generated by the target itself to get an estimate of its position, and is as a result minimally invasive. This processing is applicable to concerns such as global warming by monitoring underwater temperature patterns, detecting military threats, earthquakes, structural monitoring, leak testing, biomedical imaging [2, 5, 3, 6, 7, 32, 33], etc.

While shown to successfully localize sources with great accuracy under the right circumstances [28, 34, 35], MFP's performance is highly dependent on a number of factors. The most obvious one is probably the inevitable mismatch between true and modeled fields. Mismatch can come from the propagation model differing from the actual signal's characteristics, and an environment too simplified or erroneously estimated. Further, the aperture of the array may be too small to sample the whole multipath structure. Low frequency signals are much more forgiving to environmental errors. Higher frequency signals of the order of a couple kilohertz only, on the other hand are typically problematic and subject to current research [36, 37]. The strength of the source and its distance from the receivers is also critical in the success of MFP. Both conventional and adaptive techniques exhibit a signal-to-noise ratio (SNR) threshold, or minimum detectable level under which localization becomes erroneous. The depth of the water column also affects MFP's performance, as shallow water environments lead to more complicated multipath structures than deep water ones [38]. Finally, a more insidious source of failure is linked to the concept of time scales. Indeed, the ocean is a variable environment.

Internal waves, tides, biological processes, circadian temperature changes to name a few are associated with a respective time scale. Monitoring and processing acoustic data beyond those times requires an explicit treatment of those phenomena in the model to properly reproduce the received signals. Sources and interferers also come with a time scale of their own. Targets are rarely static, and the faster they move, the faster they cross the range-depth array processing resolution cells, reducing the time length of data available to localize the source within a cell and therefore degrading the signal processing performance.

Those factors limit the range-depth localization performance of MFP in difficult scenarios, however an alternative but important application of the technique is the more forgiving classification of surface versus submerged sources, along with an estimate of the receiver-source distance. Indeed, this information is not available using techniques like plane wave beamforming but is essential for many naval applications, for example.

Scope of this thesis

A number of techniques are applied to mitigate the effects of unfavorable factors, and extend MFP's performance domain, making it more suited to real life applications. These modifications to the algorithm are the subject of current research, and the focus of this thesis project. Some alterations might help reduce the sensitivity to a particular factor, but render it worse in another area. Care must therefore be taken in assessing the potential main causes of failure first to better choose the right compromise suited to the situation. For instance, applying an adaptive method like the minimum variance directionless response (MVDR) algorithm will dramatically improve the detectability of the signal by lowering the background noise level and canceling out interferers. Unfortunately, the sensitivity to any kind of mismatch is also greatly enhanced in the process, making it hardly usable outside of the simulated world [17].

Chapter 2 introduces the relevant aspects of matched-field processing. Conventional and adaptive techniques are introduced, as well as narrowband and

broadband incoherent and coherent methods. All the possible combinations obtained are compared using simulated and experimental data. The white noise constraint adaptive method is shown to be more robust to environmental mismatch and snapshot deficiency, while coherent broadband techniques increase the detectability of a weak signal.

Chapter 3 is a published study on coherent broadband white noise constraint processing using simulated and experimental data to validate the algorithm. The dynamic range bias obtained in snapshot deficient scenarios is investigated and shown to be consistent with narrowband results presented in the literature.

Chapter 4 presents a soon-to-be-submitted paper on fully coherent matched-field processing. A technique to extract the source signal spectrum's phases from the data is presented and the added processing gain offered is validated through theory, simulation and experimental data.

Chapter 5 provides a soon-to-be-submitted study on how to mitigate the effect of environmental fluctuations on high-frequency matched-field processing. A singular value decomposition technique to extract the most stable features of sound-speed perturbed replica vectors gave promising results on experimental data.

Finally, Chapter 6 presents the results obtained and provides related future areas of research.

Bibliography

[1] M. L. Hughes. A re-evaluation of the relation between physiological channel interaction and electrode pitch ranking in cochlear implants. *J. Acoust. Soc. Am.*, 124(5):2711–2714, November 2008.

[2] J. Condliffe, H. A. Schiffter, R. O. Cleveland, and C. C. Coussios. An acoustic microscopy technique to assess particle size and distribution following needle-free injection. *J. Acoust. Soc. Am.*, 127(4):2252–2261, April 2010.

[3] Feng-Yi Yang and Shing-Hwa Liu. Effect of ultrasound contrast agent dose on the duration of focused-ultrasound-induced blood-brain barrier disruption. *J. Acoust. Soc. Am.*, 126(6):3344–3349, December 2009.

[4] Jean-Luc Robert, M. Burchner, and C. Cohen-Bacrie. Time reversal operator decomposition with focused transmission and robustness to pseckle noise: Apllication to microcalcification detection. *J. Acoust. Soc. Am.*, 119(6):3848–3859, June 2006.

[5] J. Mamou and J. A. Ketterling. Subharmonic analysis using singular-value decomposition od ultrasound contrast agents. *J. Acoust. Soc. Am.*, 125(6):4078–4091, June 2009.

[6] F. B. Cegla, P. Cawley, and M. J. S. Lowe. Material property measurement using the quasi-scholte mode - a waveguide sensor. *J. Acoust. Soc. Am.*, 117(3):1098–1107, March 2005.

[7] V. M. Keppens, J. D. Maynard, and A. Migliori. Listening to materials: From auto safety to reducing the nuclear arsenal. *Acous. Roday*, 6(2):6–13, April 2010.

[8] A. Al-Kurd. Coherent underwater digital communication during lwad 99-1 experiment: Performance and analysis (a). *J. Acoust. Soc. Am.*, 107(5):2859–2860, May 2000.

[9] K. G. Kebkal and R. Bannasch. Sweep-spread carrier for underwater communication over acoustic channels with strong multipath propagation. *J. Acoust. Soc. Am.*, 112(5):2043–2052, November 2002.

[10] D. Roussef, M. Badley, and A. song. Effect of reflected and refracted signals on coherent underwater acoustic communication: Results from the kauai experiment (kauaiex 2003). *J. Acoust. Soc. Am.*, 126(5):2359–2366, November 2009.

[11] D. C. Braun, C. Lindsey, Y. Fan, and S. M. Jefferies. Local acoustic diagnostics of the solar interior. *Astrophysical Journal, Part 1 (ISSN 0004-637X)*, 392(2):739–745, June 1992.

[12] A. Burrows, E. Livne, L. Dessart, C. D. Ott, and J. Murphy. Features of the acoustic mechanism of core-collapse supernova explosions. *The Astrophysical Journal*, 655:416–433, January 2007.

[13] P. Ulmschneider, J. theurer, and Z. E. Musielak. Acoustic wave energy fluxes for late-type stars. *Astonomy and Astrphysics*, 315:212–221, 1996.

[14] A. H. Quazi and W. L. Konrad. Underwater acoustic communications. *IEEE communications magazine*, 20(2):24–30, March 1982.

[15] A. A. Winder. Ii. sonar system technology. *IEEE Trnsactions on Sonics and Ultrasonics,*, 22(5):291–332, September 1975.

[16] L. C. Godara. Application of antenna arrays to mobile communications. ii. beam-forming and direction-of-arrival considerations. *Proceedings of the IEEE*, 85(8):1195–1245, August 1997.

[17] H. L. Van Trees. *Optimum Array Processing, part IV of Detection, Estimation, and Modulation Theory*. Wiley-interscience, 2002.

[18] B. D. Van Veen and K. M. Buckley. Beamforming: a versatile approach to spatial filtering. *ASSP Magazine, IEEE*, 5(2):4–24, April 2002.

[19] J. N. Maksym. A robust formulation of an optimum cros-spectral beamformer for line arrays. *J. Acoust. Soc. Am.*, 65(4):971–975, April 1979.

[20] H. S. Schmidt, A. B. Baggeroer, W. A. Kuperman, and E. K. Scheer. Environmentally tolerant beamforming for high-resolution matched-field processing: Deterministic mismatch. *J. Acoust. Soc. Am.*, 73:813–825, 1979.

[21] J. L. Krolik. Matched-field minimum variance beamforming in a random ocean channel. *J. Acoust. Soc. Am.*, 92:1408–1419, 1992.

[22] J. V. Candy and J. Sullivan. Model-based identification: An adaptive approach to ocean-acoustic processing. *IEEE Journal of Oceanic engineering*, 21:273–289, 1996.

[23] H. Cox, R. M. Zeskind, and M. M. Owen. Robust adaptive beamforming. *IEEE Transactions on Acoustics, Speech and Signal Processing*, 35(10):1365–1376, October 1987.

[24] A. Aubry, A. derode, P. Roux, and A. Tourin. Coherent backscattering and far-field beamforming in acoustics. *J. Acoust. Soc. Am.*, 121(1):70–77, January 2007.

[25] A. B. Gershman, V. I. turchin, and V. A. Zverev. Experimental results of localization of moving underwater signal by adaptive beamforming. *IEEE Transactions on Signal Processing*, 43(10):2249–2257, October 1995.

[26] B. G. Ferguson. Improved time-delay estimates of underwater acoustic signals using beamforming and prefiltering techniques. *IEEE Journal of Oceanic engineering*, 14(3):238–244, July 1989.

[27] F. B. Jensen, W. A. Kuperman, M. B. Porter, and H. Schmidt. *Computational Ocean Acoustics*. Springer-Verlag New York, Inc., 2000.

[28] A. B. Baggeroer, W. A. Kuperman, and P. N. Mikhalevsky. An overview of matched field methods in ocean acoustics. *IEEE Journal of Oceanic engineering*, 18(4):401–424, october 1993.

[29] M. D. Collins and W. A. Kuperman. Inverse problems in ocean acoustics. *Inverse Problems*, 10(5):1023, 1994.

[30] S. E. Dosso, M. L. Yeremy, J. M. Ozard, and N. R. chapman. Estimation of ocean-bottom properties by matched-field inversion of acoustic field data. *IEEE Journal of Oceanic engineering*, 18(3):232–239, July 1993.

[31] M. I. Taroudakis and M. G. Markaki. On the use of matched-field processing and hybrid algorithms for vertical slice tomography. *J. Acoust. Soc. Am.*, 102(2):885–895, August 1997.

[32] P. N. Mikhalevsky, A. B. Baggeroer, A. Gravilov, and M. Slavinsky. Experiment tests use of acoustics to monitor temperature and ice in the artic ocean. *EOS, Transactions, Americen Geophysical Union*, 76(27):265–268, July 1994.

[33] D. H. Salzberg, K. E. Votaw, and M. E. Marshall. Seismic source locations and parameters for sparse networks by matching observed seismograms to semi-empirical synthetic seismograms. In *27th Seismic Research Review: Ground-Based Nuclear Explosion Monitoring Technologies*. SAIC Ocean Sciences Division, 2005.

[34] Renhe Zhang, Zhenglin Li, Jin Yan, Zhaohui Peng, and Fenghua Li. Broadband matched-field source localization in the east china sea. *Journal of Oceanic Engineering, IEEE*, 24(4):1049–1054, October 2004.

[35] G. C. Chen and W. S. Hodgkiss. Vlf source localization with a freely drifting acoustic sensor array. *Journal of Oceanic Engineering, IEEE*, 18, issue 3:209–223, July 1993.

[36] P. Hursky, M. B. Porter, and M. Siderius. High frequency (8-16 hz) model-base source localization. *J. Acoust. Soc. Am.*, 115:3021–3032, 2004.

[37] cristiano Soares, Martin Siderius, and Sergio M. Jesus. Source localization in a time-varying ocean waveguide. *J. Acoust. Soc. Am.*, 112(5):1879–1889, Nov 2002.

[38] Z. Li and J. Yan. *The effects of Internal Waves on Broadband Source Localization in Shallow water*. world Wcientific Publishing Co., national Laboratory of Acoustics, Chinese Academy of Sciences, Beijing, China, 2001.

Chapter 2

Linear and non linear broadband matched-field processing techniques

In this chapter, the concept and implementation of matched-field processing (MFP) is briefly reviewed. The notation and terminology used throughout the remainder of the document is introduced. A description of the signal, array, waveguide and propagation model is also provided. We then develop the formulations describing the conventional MFP and two types of adaptive methods, the minimum variance distortionless response (MVDR) and white noise constraint method (WNCM). Simulated and real data outputs are presented to compare the different methods' ability to locate an acoustic source.

2.1 Measured and modeled acoustic field

2.1.1 Characterization of the measured field and environment

Acoustic targets are modeled as point sources emitting a usually broadband signal from one point (R_s, Z_s) in the waveguide, R_s being the horizontal distance between the source and the array, and Z_s the depth of the source. The origin of the range axis is set at the receiver array's position. The depth axis is pointing downward, its origin being the water surface. Figure (2.1) displays the simplified range-independent oceanic waveguide, where the fluid halfspace is infinite in the horizontal direction and the surface and bottom planes are parallel. The air-sea interface is considered to be a perfectly reflecting boundary, as opposed to the semi-infinite bottom halfspace, where energy is allowed to be transmitted and lost. The acoustic waves travel away from the source, undergoing reflections, refraction, dissipation until they reach the vertical line array (VLA) where each element will record the corresponding time series. Each time series is then Fourier transformed and the data in the frequency bins associated to the signal's bandwidth is extracted.

Let $x_\omega^{(i)}$ denote the complex field received on the hydrophone i at angular frequency ω, N the number of hydrophones in the array, and L the number of individual frequencies considered.

$$x_\omega^{(i)} = S(\omega)G^{(i)}(0, z_i, R_s, Z_s, \omega) + Q^{(i)}(\omega), \tag{2.1}$$

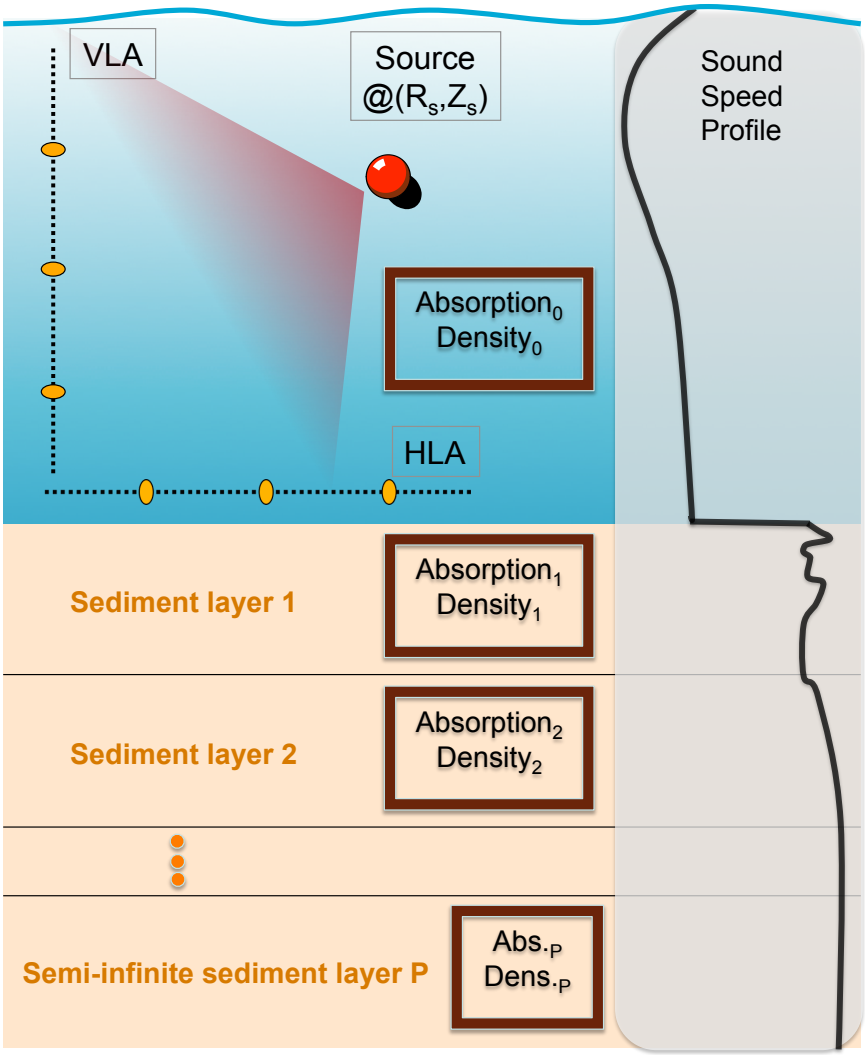

Figure 2.1: A typical ocean environment. The fluid halfspace and sediment layers are infinite in the horizontal direction. A source is present at range R_s from the vertical line array (VLA) or center of horizontal line array (HLA) and depth Z_s, where the origin of the depth axis is the air-sea interface. Each layer is characterized by its density, sound speed and absorption as a function of depth.

where $S(\omega)$ is the frequency dependent complex source spectrum, the expression $G^{(i)}(0, z_i, R_s, Z_s, \omega)$ the ocean waveguide's Green's function between the source location and the element i of the receiving array, and $Q^i(\omega)$ the complex noise component corrupting the signal. This noise is a combination of sensor noise and ambient noise.

For narrowband signals, the mean input signal-to-noise ratio (SNR) at the array elements is defined as [1]:

$$SNR_{Input} = 10log\left(\frac{\frac{1}{N}\sum_{i=1}^{N}|S(\omega)G^{(i)}(0, z_i, R_s, Z_s, \omega)|^2}{\frac{1}{N}\sum_{i=1}^{N}|Q^{(i)}(\omega)|^2}\right). \tag{2.2}$$

To improve the signal's detectability over noise, an array of hydrophones is deployed instead of a single element. The amount by which the signal is enhanced over the noise at the output of the array is referred to as array gain (AG):

$$AG = \frac{SNR_{Output}}{SNR_{Input}}. \tag{2.3}$$

When the array is steered in the right direction, the signal is summed coherently along the receivers, while the incoherent part of the noise adds incoherently. The SNR at the output of the array becomes:

$$SNR_{Output} = 10log\left(\frac{\sum_{i=1}^{N}|S(\omega)G^{(i)}(0, z_i, R_s, Z_s, \omega)|^2}{\frac{1}{N}\sum_{i=1}^{N}|Q^{(i)}(\omega)|^2}\right),$$

and the array gain is

$$AG = 10log\,(N)\,. \tag{2.4}$$

2.1.2 Generation of the synthetic field

The Green's function is the signature of the acoustic wave propagation from one point in the waveguide to another, or in other words the impulse response of the ocean channel between the two points. It includes the contribution attributed to both direct-path and multipath components of the field.

In order to properly characterize and localize the source, the Green's functions between every point of the waveguide and each array elements must be

constructed. This requires a comprehensive understanding of energy propagation along a waveguide, and a detailed knowledge of the environment itself. For instance, a proper propagation model requires an estimate of the shape of the ocean/sediment and sub-bottom interfaces, as well as the density, attenuation and sound speed profiles in each layer. While a range independent stratified environment is often good enough to properly model the pressure field on the array, higher frequencies, internal waves or sub-surface structures may require an estimate of those parameters as a function of range as well. Additionally, the array elements position has to be known with a precision of about $\lambda/10$, λ being a characteristic wavelength of the signal sent.

Computing the Green functions of a system involves solving the frequency domain wave equation, also known as the Helmoltz equation [2, 3]:

$$\Delta^2 G\left(r,z\right) + k^2\left(z\right) G\left(r,z\right) = -\delta\left(r - R_s\right)\delta\left(z - Z_s\right), \tag{2.5}$$

where the wavenumber is defined as

$$k^2\left(z\right) = \frac{\omega^2}{c^2\left(z\right)}. \tag{2.6}$$

The forcing term (delta functions) corresponds to a monochromatic point source at (R_s, Z_s).

For a range-independant environment unbounded in the horizontal direction, the wave equation can be separated, and the solution expressed as a product of the depth dependent Green's function $g\left(k_r, z, Z_s\right)$ and horizontally traveling plane waves $e^{ik_r r}$, where k_r represents the horizontal wavenumber.

$$G\left(r,z\right) = \frac{1}{4\pi^2} \int_{-\infty}^{\infty} g\left(k_r, z, Z_s\right) e^{ik_r\left(r - R_s\right)}\,\mathrm{d}k. \tag{2.7}$$

By substituting Eq. 2.7 into the wave equation Eq. 2.5, one can show that the depth dependent Green's function obeys:

$$\frac{\mathrm{d}^2 g}{\mathrm{d}z^2} + \left(k^2\left(z\right) - k_r^2\right) g = -\delta\left(z - Z_s\right). \tag{2.8}$$

The homogeneous version of Eq. 2.8 is an eigenvalue problem whose eigenvectors are called the vertical normal modes of the waveguide, U_n. Hence the solution of the wave equation is a product of standing waves in the vertical bounded

direction and traveling waves in the infinite horizontal one. The modal functions satisfy:

$$\frac{\mathrm{d}^2 U_n}{\mathrm{d}z^2} + \left(k^2(z) - k_{r_n}^2\right) U_n = 0, \tag{2.9}$$

subject to the pressure release surface and the boundary condition at the water-bottom interface.

The normal mode representation of the wave equation's far field solution in a cylindrical coordinate system is written as:

$$G(r,z) = \frac{i\rho(Z_s)}{(8\pi r)^{1/2}} e^{-\frac{i\pi}{4}} \sum_n \frac{U_n(Z_s)\, U_n(z)}{\sqrt{k_{r_n}}} e^{ik_{r_n} r}. \tag{2.10}$$

The eigenvectors or modes are orthogonal, and normalized according to:

$$\int_0^\infty \frac{U_m(z)\, U_n(z)}{\rho(z)} \mathrm{d}z = \delta_{m,n}, \tag{2.11}$$

where $\delta_{m,n}$ is the Kronecker symbol.

The associated eigenvalues are real and smaller than ω/c_{min}, where c_{min} is the lowest sound speed in the water column. The number of propagating modes in the waveguide is thus dependent on frequency, high frequencies involving more modes than low frequencies.

Each mode travels along the waveguide at its own phase and group velocities, both functions of frequency as well. This implies that the normal modes will disperse as they propagate. Hence, an array positioned several water depths away from a source emitting an impulse signal will receive a smeared version of the signal, longer than the original pulse due to dispersion in the waveguide.

The phase velocity of a mode is the horizontal velocity at which its phase is displaced [3]. It is defined as

$$v_n = \frac{\omega}{k_{r_n}}. \tag{2.12}$$

It may not correspond to a particular physical entity, and is not the speed at which the energy is propagating. The steeper the propagation angle the larger the phase speed. For a horizontal propagation, the phase speed equals the speed of sound.

The group speed, on the other hand, is the horizontal velocity at which the information and energy actually propagates down the channel. It is defined as

$$u_n = \frac{\mathrm{d}\omega}{\mathrm{d}k_{r_n}}. \tag{2.13}$$

The group speed is always less than or equal to the maximum speed of the sound speed profile.

Equation 2.10 allows us to model the monochromatic acoustic field at (r, z) coming from a point source at (R_s, Z_s) provided that the layer depths, sound speed, density and attenuation are known. Those field estimates can now be matched to the received signal, giving its name to the matched-field processing technique.

2.2 Narrowband conventional MFP

2.2.1 Formulation of the algorithm

Matched-field processing is essentially performing a sum of correlations between modeled and measured acoustic fields over elements. Typically, the complex field received on each hydrophone is stacked in a (Nx1) vector:

$$\boldsymbol{x}_\omega = \left[\; x_\omega^{(1)}, x_\omega^{(2)}, \ldots, x_\omega^{(N)} \; \right]^T, \tag{2.14}$$

where the notation ^{T} denotes the transpose operator.

This section introduces the basis of matched-field processing techniques at a single frequency. The angular frequency dependance ω is therefore dropped from the notation for clarity purposes, but will be reinstated in section 2.4 when multiple frequencies are taken into account.

The modeled field on the array from a hypothetical source at (r, z) can be written in a (Nx1) vector as well, commonly called the replica vector, or weight vector $\boldsymbol{w}$.

$$\boldsymbol{w}\left(r, z\right) = \left[\; w^{(1)}, w^{(2)}, \ldots, w^{(N)} \; \right]^T. \tag{2.15}$$

The expression of the weight vector varies depending on the type of algorithm, but the matched-field processor output is always expressed as:

$$\begin{aligned} P\left(r, z\right) &= \left| \boldsymbol{w}^H\left(r, z\right) \boldsymbol{x} \right|^2 \\ &= \boldsymbol{w}^H\left(r, z\right) \boldsymbol{x}\boldsymbol{x}^H \boldsymbol{w}\left(r, z\right), \end{aligned} \tag{2.16}$$

where ^{H} refers to the Hermitian transpose, or complex conjugate transpose operation. When the received time series are long enough, a better estimate of the signal

can be obtained by averaging data segments. To do so, the received signal at each element is divided into K 50% overlapped segments of data, and each segment is Fourier transformed. If the source and environment are relatively stationary for the whole duration of the K time segments, averaging the snapshots should enhance the signal and average the noise down.

Therefore, the output of the matched filter is estimated in practice according to:

$$\begin{aligned} P(r,z) &= \boldsymbol{w}^H \left[\frac{1}{K} \sum_{q=1}^{K} \boldsymbol{x}_q \boldsymbol{x}_q^H \right] \boldsymbol{w} \\ &= \boldsymbol{w}^H \boldsymbol{R} \boldsymbol{w}. \end{aligned} \tag{2.17}$$

where $\boldsymbol{R}$ is the cross-spectral density matrix (CSDM) of the ambient field. Its rank is the number of snapshots K involved in the average. Since adaptive algorithms often involve the inverse of the CSDM, $\boldsymbol{R}$ needs to be well defined. A number of snapshots equal or bigger than twice the number of elements is usually enough for the matrix to be invertible. When the ocean variability or source motion prevents the acquisition of $2N$ segments, we are in a non-optimal, "snapshot deficient" scenario for which the inverse of the CSDM has to be estimated using diagonal loading or subspace methods via singular value decomposition of $\boldsymbol{R}$ [4, 5].

Conventional MFP, introduced by Bucker [6, 7], is the most intuitive of all algorithms. It compares the received data to the modeled one by correlating them, or equivalently taking the inner product of the complex conjugated synthetic field and measured one in the frequency domain.

The weight vector is given by the modeled Green's function from Eq. 2.10 between a source at (r,z) and the array elements at $(0,z_i)$:

$$\begin{aligned} \boldsymbol{w}_{Conv}(r,z) &= \boldsymbol{d}(r,z) \\ &= \frac{\left[\, G(r,z_1,z), G(r,z_2,z), \ldots, G(r,z_N,z) \, \right]^T}{\left\| \left[\, G(r,z_1,z), G(r,z_2,z), \ldots, G(r,z_N,z) \, \right] \right\|}. \end{aligned} \tag{2.18}$$

The conventional MFP output at one frequency is described as:

$$P_{Conv}(r,z) = \boldsymbol{d}^H(r,z) \, \boldsymbol{R} \boldsymbol{d}(r,z). \tag{2.19}$$

2.2.2 Simulated and real data example using the SWellEx-96 Experiment

Let us consider a relatively straightforward case of a strong source in a shallow water environment emitting a low frequency single tone to a vertical array. The SWellEx-96 experiment data set [8, 9] is a prime choice to study and compare various MFP algorithms, in part because of the extensive study of the environment conducted, providing us with an accurate description of the media, but also because of the low ocean variability during the scope of the experiment. This data set will be used later on in Chapter 4.

The experiment was conducted between May 10 and 18, 1996 near San Diego, California. Two acoustic sources were towed along an isobath in 216 m of water, transmitting multitones at various strength between 50 and 400 Hz. Three types of arrays were deployed in the water to receive the signal. A vertical line array (VLA), and a tilted line array (TLA) recorded 75 minutes of data, while two horizontal line arrays (HLA North and South) recorded the last 50 minutes only.

The deep source ($Z_s = 54m$) transmitted five sets of 13 tones simultaneously. The "High Tonal Set" was projected at about 158 dB per frequency, the second tonal set at 132 dB and each subsequent set 4 dB down from the previous one. Having multiple frequencies available in the signal sent is an asset, as illustrated in Chapter 4, since it allows us to apply incoherent or coherent broadband processing techniques. Having several frequencies at various projected level at hand is a particularly nice feature of this data set. This data gives the user an unique opportunity to compare the algorithms' ability to detect weaker and weaker sources, which will be especially useful in Chapter 4.

Figure (2.2), extracted from [9] shows the experimental setup overlaid on the site bathymetry. The various arrays' position are given by the green stars, and the source track by the blue line, marked at 5 min intervals. The source moved in a straight line towards then away from the arrays. As apparent on Fig. (2.5), the track passed about a km away from each array, and as far as 7 km for HLA North and South and 8.5 km for VLA and TLA.

Figure (2.4) gives a schematic representation of the environmental parame-

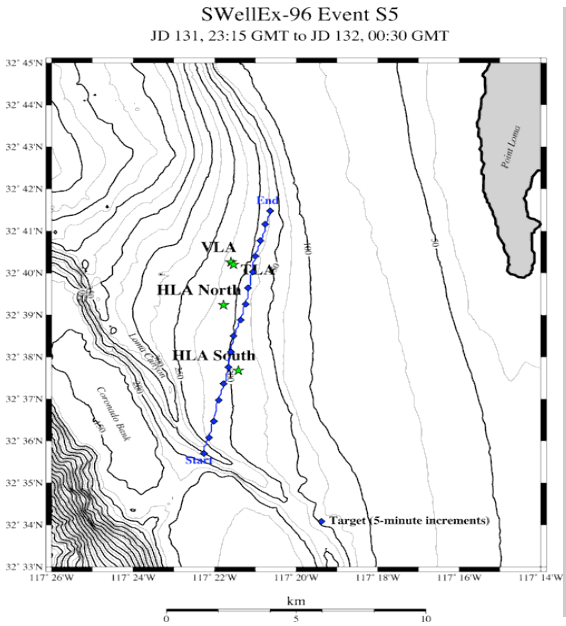

Figure 2.2: Source track and arrays' position along the 75 min long transect. Each blue dot represents the source's position every 5 min.

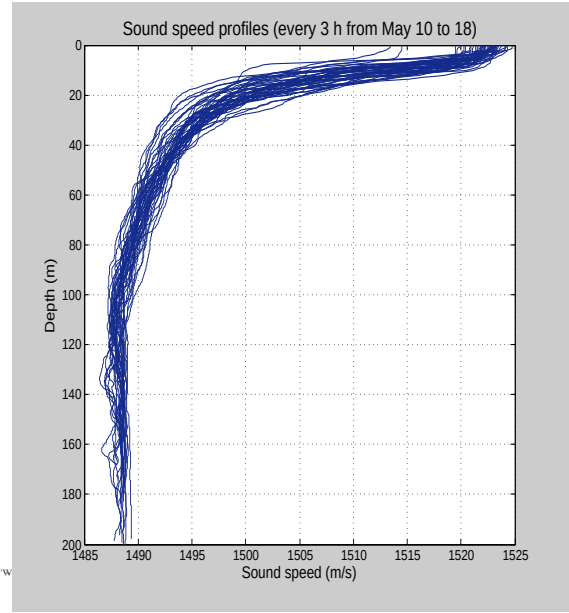

Figure 2.3: Sound speed variability over a week obtained from conductivity temperature depth (CTD) measurements.

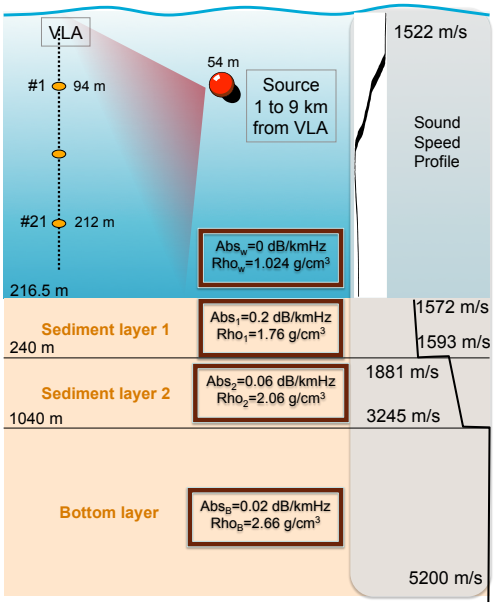

Figure 2.4: The SWellEx environment.

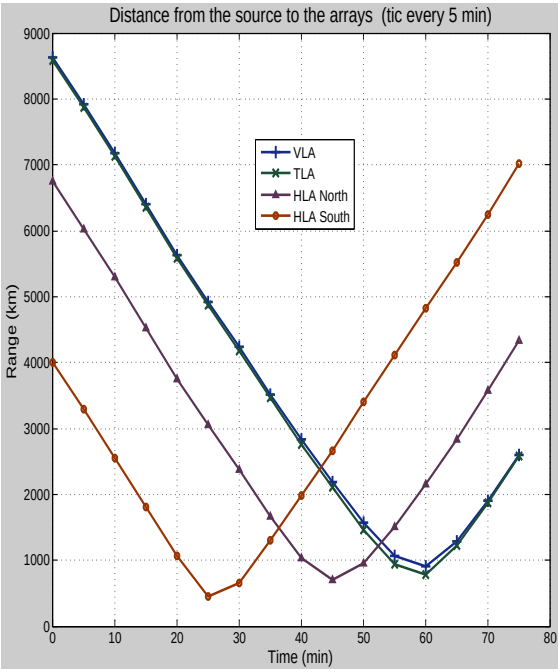

Figure 2.5: Distance between the source and arrays in km.

ters available to model the acoustic field. The VLA spanned the second half of the 216.5m deep water column, with 21 elements equally spaced by 5.6 m between 94 m and 212 m depths. The seafloor is composed of three sediment layers. The first one of 23.5 m thick has a compressional attenuation of 0.2 $dB/kmHz$, a linearly increasing sound speed from 1572.368 m/s to 1593.016 m/s and a density of 1.76 g/cm^3. It overlays a 800 m thick mudstone layer with a density of 2.06 g/cm^3, an attenuation of 0.06 $dB/kmHz$ and sound speed from 1881 m/s to 3245 m/s. Finally, the bottom halfspace has a 2.66 g/cm^3, 0.02 $dB/kmHz$ attenuation and sound speed of 5200 m/s.

A conductivity-temperature-depth (CTD) survey was conducted to assess the ocean's variability during the week long experiment. Fifty-one CTD casts are available, about one every 3 hours. Figure (2.3) shows the resulting sound speed profiles in the water column versus depth. The thermocline is around 20 m depth. The sound speed spread is only a couple m/s wide under the thermocline, and at most 10 m/s in the surface layer over a week. The ocean environment is therefore not only very well studied over the duration of the experiment, but also stable enough to be well suited to low frequency MFP.

To demonstrate the feasibility of matched-field source localization and illustrate the performance of conventional MFP at a single frequency, a simulated SWelleX data set and environment is first implemented. The synthetic results obtained will then be compared to the corresponding experimental results.

The lowest frequency of the high level set of tones (49 Hz) is chosen to implement MFP. The simulated monochromatic source signal is created by adding isotropic noise to the modeled acoustic field obtained from the normal mode equation Eq. 2.10 at $R_s = 4250m$ and $Z_s = 54m$. We set the number of snapshots to be twice the number of elements, *ie* 42 snapshots. Therefore, we need to create 42 noise realizations and add them to the signal. The noise level is set such that the signal-to-noise ratio at each element is 12.5 dB. The noise created is complex, with a random phase and an amplitude following the Rayleigh distribution at each element. The snapshots are then combined to create the cross spectral density matrix, according to Eq. 2.17.

We then set a grid in range and depth to study the match between the simulated data and the replica field at each point. Typically, a spacing of at least $\lambda/10$ in depth and a couple λ in range, where λ is the signal's wavelength is required to sample the search space adequately. In our case, $\lambda = 30.6m$, and the grid points are set to be 0.5 m apart in depth ($\approx \lambda/60$) and 25 m apart in range ($\approx 0.8\lambda$) up to 10 km from the array. The waveguide is therefore densely sampled. The replica field is constructed for each grid point using the normal mode solution to the wave equation Eq. 2.10, and matched to the data according to Eq. 2.17.

Figure (2.6) shows the simulated ambiguity surface obtained. The main lobe is normalized to zero dB, and the dynamic range is set to display the results between 0 and 10 dB down the maximum. The circle represent the position of the simulated source, and the square the position of the conventional algorithm's maximum. As apparent on the figure, the MFP processor does localize the source. However, some of the sidelobes are so high that it renders the localization ambiguous, which is a typical result using conventional, narrowband MFP.

This simulated output is now compared to the real data one. The received time series at each element are extracted at $T = 30min$ and divided into 42 - 50% overlapped segments. The length of the snapshots must be chosen long enough such that the spread of modes (due to dispersion) propagating at the frequency of interest has fully travelled from the source to the array, and that the frequency bin of the snapshot's Fourier transform is small enough to limit the signal's contamination by noise. But the snapshots cannot be too long either, since the environment, receivers and source have to remain somewhat stationary during the total duration of the 42 - 50% overlapped segments. In our case, by inspection of the lowest and highest group speeds of the modes at 49 Hz (1188 m/s and 1488 m/s respectively), the spread in time of arrival of the modes at the array is $t = 1.7s$, or 2550 points sampled at $f_s = 1500Hz$. We chose a snapshot length of $2^{13} = 8192$ points, well above the time needed to capture the modes spread and have a discriminating frequency bin, but small enough for the environment to remain stable. The cross-spectral density matrix is then constructed the usual way, and conventional MFP is applied to the data to determine the source's position in

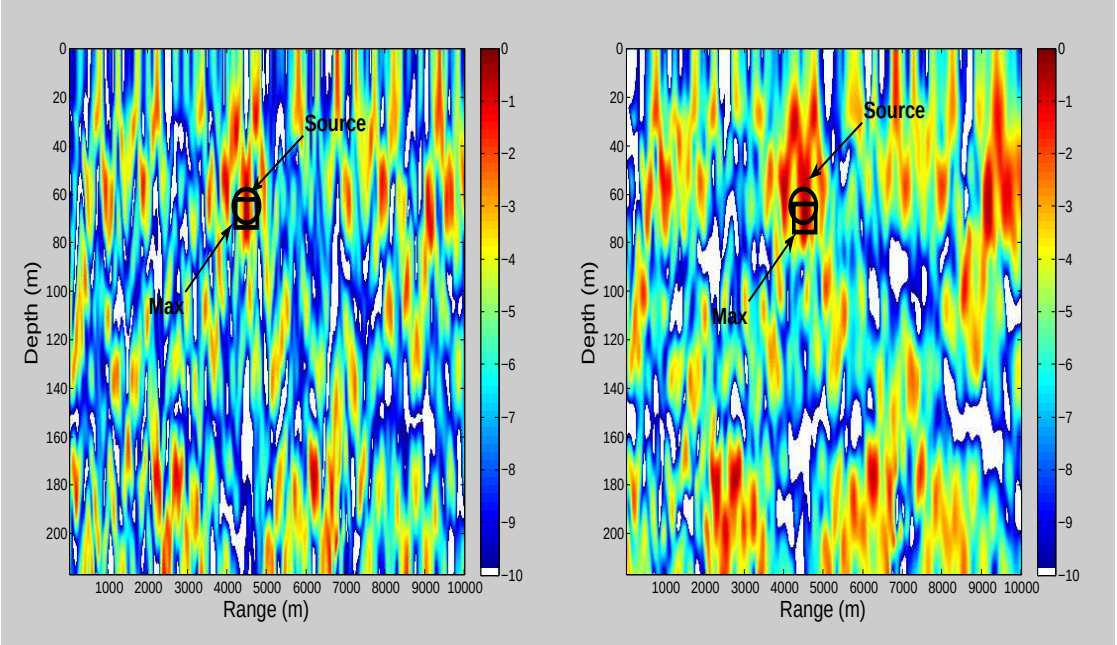

Figure 2.6: Simulated conventional MFP at 49 Hz. The circle represent the position of the simulated source, and the square the position of the conventional algorithm's maximum.

Figure 2.7: Real data conventional MFP at 49 Hz.The circle represent the position of the source, and the square the position of the conventional algorithm's maximum.

range and depth.

Figure (2.7) displays the experimental ambiguity surface obtained, also normalized such that the maximum is at 0 dB, and showing a 10 dB dynamic range. The real data output is really close to the simulated one. The source is successfully localized, demonstrating the robustness of the conventional algorithm to presence of environmental mismatch between modeled and real scenarios. But as for the simulated case, the presence of high sidelobes prevents an unambiguous source localization.

While conventional MFP is relatively robust to the presence of mismatch between the environment used to propagate the modeled pressure field and the actual environment, it lacks resolution and displays sidelobes often too high to localize the position of the source without ambiguity. This has been dealt in the

narrowband beamforming/MFP literature by introducing adaptive algorithms.

2.3 Narrowband adaptive MFP

In this section, the minimum variance distortionless response (MVDR) and white noise constraint method (WNCM) are presented, and their localization performance is evaluated on modeled and experimental data obtained from the SWellEx-96 experiment.

2.3.1 The minimum variance algorithm

Adaptive processors are non linear methods obtained by solving a constrained optimization problem. They use the data itself to construct optimum weights. The Minimum Variance Distortionless Response (MVDR) [3, 10] processor is the most widely known and used adaptive algorithm. As with every matched-field processor, the MVDR output takes the form:

$$P(r,z) = \boldsymbol{w}^H \boldsymbol{R} \boldsymbol{w}. \tag{2.20}$$

The weight vector is determined by solving

$$\min_{\boldsymbol{w}} \boldsymbol{w}^H \boldsymbol{R} \boldsymbol{w} \quad subject\ to\ \boldsymbol{w}^H \boldsymbol{d} = 1, \tag{2.21}$$

where $\boldsymbol{d}$ is the conventional weight vector at (r,z).

This optimization problem can be interpreted as a filter which passes the look direction signal undistorted while rejecting noise and interferers.

Using the method of the Lagrange multiplier, we obtain the well known solution:

$$\boldsymbol{w}_{mvdr} = \frac{\boldsymbol{R}^{-1}\boldsymbol{d}}{\boldsymbol{d}^H \boldsymbol{R}^{-1} \boldsymbol{d}}. \tag{2.22}$$

Substitution into Eq. 2.20 yields the final expression of the MVDR power output:

$$P_{mvdr}(r,z) = \frac{1}{\boldsymbol{d}(r,z)^H \boldsymbol{R}^{-1} \boldsymbol{d}(r,z)}. \tag{2.23}$$

This algorithm enhances the resolution considerably in comparison to the conventional processor, however this exceptional resolution capability comes with

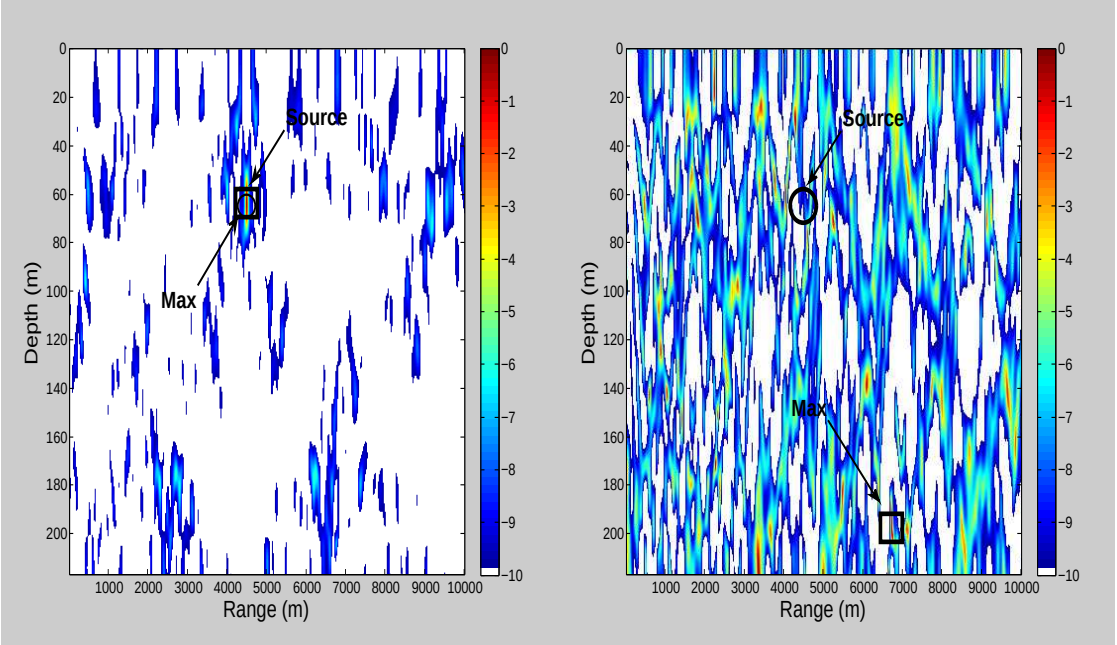

Figure 2.8: Simulated MVDR MFP at 49 Hz. The circle represent the position of the simulated source, and the square the position of the conventional algorithm's maximum.

Figure 2.9: Real data MVDR MFP at 49 Hz. The circle represent the position of the source, and the square the position of the conventional algorithm's maximum.

an increased sensitivity to slight mismatch between the modeled and actual environment [2, 11, 12].

For comparison purposes, the same portion of simulated and received signal as in Sec. 2.2.2 is used to generate the MVDR ambiguity surfaces. Since enough snapshots are involved in the creation of the CSDM (twice the number of elements), the matrix is well conditioned and invertible.

Figure (2.8) shows the simulated MVDR ambiguity surface obtained. As expected, the optimization process allows the signal to pass undistorted while minimizing the amount of noise and interferers. The background level has been greatly reduced, and the median value of the ambiguity surface went from -6.7 dB for the conventional to -10.4 dB for the MVDR. The sidelobe level is also lower (6 dB down the maximum for the simulated MVDR compared to less than a dB

down for the simulated conventional), rendering the algorithm more discriminating. However, this increase in resolution also means that the environment needs to be known with more accuracy. In fact, the MVDR algorithm is so sensitive to any kind of mismatch that it is often not practical for experimental localization purposes. Figure (2.9) shows the MVDR ambiguity surface obtained from real data at 49 Hz. The sidelobes and background noise are indeed lowered and the median value of the power output is now -9.3 dB instead of -5.7 dB obtained with the conventional algorithm. But the source is now incorrectly localized, due to imperfect reproduction of the pressure field.

A number of adaptive techniques inspired from the MVDR have been proposed in the literature [13, 14, 15, 11, 16]. The concept is to modify the algorithm such that the noise and interferers level are still reduced, but the high resolution is relaxed, making the process more forgiving to uncertainties in the model. Robustness has been enhanced by either (1) enlarging the search space or providing some sort of environmental blurring [13, 17, 15, 16] or (2) constraining the algorithmic cause of the instability [14, 11]. The white noise constraint method, described in the next section belongs into the second category and is a good candidate for robust experimental source localization.

2.3.2 White noise constraint method

Many sources of errors are uncorrelated from sensor to sensor, and hence appear to the array like spatially white noise. Cox *et al* [14] showed that the gain against uncorrelated noise is a measure of robustness, or in other words the sensitivity of the algorithm to signal mismatch is equal to the reciprocal of the white noise gain. This observation led them to introduce an inequality constraint on the gain against spatially white noise. This modified MVDR, called White Noise Constraint Method (WNCM) algorithm, consequently lost some of its high-resolution characteristics along with its requirement for very precise knowledge of the environment.

The white noise gain is defined as:

$$\boldsymbol{G_w} = \frac{|\boldsymbol{w}^H \boldsymbol{d}|}{\boldsymbol{w}^H \boldsymbol{w}}. \tag{2.24}$$

The new optimization problem maximizes the gain against white noise in an effort to reduce the sensitivity of the MVDR processor to mismatch:

$$\min_{\boldsymbol{w}} \boldsymbol{w}^H \boldsymbol{R} \boldsymbol{w} \;\; \textit{subject to} \;\; \boldsymbol{w}^H \boldsymbol{d} = 1 \;\; \textit{and} \;\; \boldsymbol{w}^H \boldsymbol{w} \leq \delta^{-2}, \tag{2.25}$$

which yields:

$$\boldsymbol{w_{wncm}}(r,z) = \frac{(\boldsymbol{R} + \epsilon \boldsymbol{I})^{-1} \boldsymbol{d}}{\boldsymbol{d}^H (\boldsymbol{R} + \epsilon \boldsymbol{I})^{-1} \boldsymbol{d}}. \tag{2.26}$$

The value of ϵ is such that the third inequality of Eq. 2.25 is satisfied.

For each position (r, z), the MVDR weight vector is implemented. If its norm satisfies the inequality condition, no modification is made and the WNCM weight vector is just the MVDR one. If on the other hand, the norm of the MVDR weight vector is bigger than the constraint, increasing values of epsilon are added to the diagonal of the CSDM, which corresponds to adding white noise to the system, until the inequality constraint is satisfied.

Note that as ϵ gets bigger and bigger, $\boldsymbol{R}$ becomes negligible compared to $\epsilon \boldsymbol{I}$, and the WNCM weight vector approaches the conventional weight vector $\boldsymbol{d}/\left(\boldsymbol{d}^H \boldsymbol{d}\right)$. In effect, the WNCM processor is dynamically transitioning between the MVDR and conventional outputs at a different rate for each grid point. In essence, it takes advantage of the conventional algorithm's wide main lobe rendering it robust to mismatch while keeping the high resolution and low sidelobes of the MVDR elsewhere.

A graphical illustration of the conventional, MVDR and WNCM weight vectors implementation has been worked out by Maksym [11]. Let us assume that the array is composed of two receivers only so all vectors are 2-dimensional, and that the components are real for simplicity of visualization. Each vector can then be mapped in the real $(\boldsymbol{w}_1, \boldsymbol{w}_2)$ space. The signal vector received from the source $\boldsymbol{d_s}$ on each element is represented as the pink vector on Fig. (2.10).

Now consider the normalized weight vector of the conventional beamformer $\boldsymbol{d}$ at (r, z) different from (R_s, Z_s), represented in green on the figure. Since the look position is different from the source location, those two vectors are not collinear.

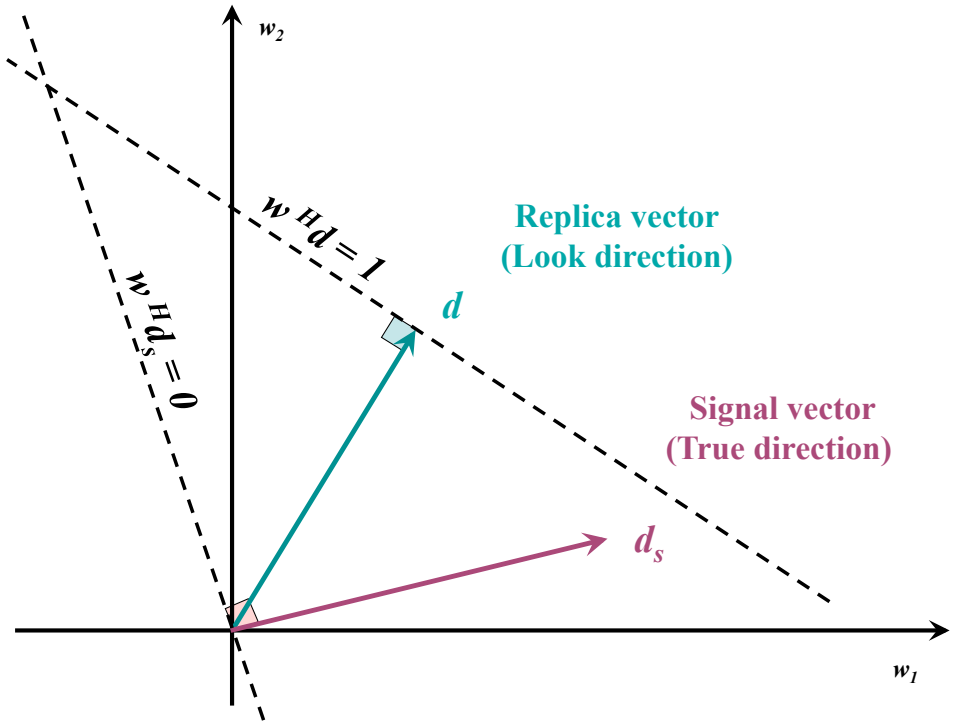

Figure 2.10: Construction of the MVDR weight vector. From the formulation of the MVDR's optimization problem in Eq. 2.21, the tip of the weight vector is constrained to be along the dotted line such that its projection onto the look "direction" is the conventional weight vector itself (in green) to satisfy $\boldsymbol{w}^H \boldsymbol{d} = 1$, but also such that its projection onto the data (in pink) is minimized.

The aim is to find the location of the MVDR's weight vector. To do so, we look back to the formulation of the MVDR's optimization problem, given in Eq. 2.21. The constraint $\boldsymbol{w}^H\boldsymbol{d} = 1$ constrains the tip of the MVDR vector to be along the dotted line such that its projection onto the look "direction" is the conventional weight vector itself. The first part of the optimization minimizes the projection of the weight vector onto the data. Hence the tip of the MVDR weight vector is found to be at the intersection between the two dotted lines $\boldsymbol{w}^H\boldsymbol{d_s} = 0$ and $\boldsymbol{w}^H\boldsymbol{d} = 1$.

Let us consider the case of the WNCM processor. If the norm of the MVDR weight vector for the specific look position (r, z) is smaller than the constraint set by the user, then the WNCM weight vector is just the MVDR one. But if it is bigger than the constraint, the right amount of white noise will be added to the CSDM such that $\boldsymbol{w}^H\boldsymbol{w} \leq \delta^{-2}$. The tip of the weight vector is still constrained to be on the dotted line $\boldsymbol{w}^H\boldsymbol{d} = 1$, but the condition $\boldsymbol{w}^H\boldsymbol{d_s} = 0$ is relaxed and the WNCM weight vector's tip is at the position along the $\boldsymbol{w}^H\boldsymbol{d} = 1$ line which guarantees the norm of the weight vector to be just under the value of the constraint, represented in blue in the Fig. (2.11).

Let us now consider the case when the look position is chosen to be at the closest grid point from the source location (R_s, Z_s). In the presence of mismatch between the modeled environment and the actual environment, and/or discrepancy between the signal and model used to recreate its propagation, and/or use of a grid which doesn't coincide with the source's position, the modeled conventional weight vector will not be exactly collinear to the data one. As apparent on Fig. (2.11), the closer the conventional weight vector gets to the signal vector (*ie*, the closer the look position to the true source position), the bigger the norm of the MVDR's weight vector needs to be to still ensure its orthogonality to the signal. Because of the presence of mismatch, the algorithm doesn't recognize the signal as the information of interest anymore, but interprets it as an interfering signal instead and proceeds to cancel it. Restricting the growth of the weight vector's norm is therefore an efficient way to avoid the signal's suppression, since the WNCM weight vector does not lie on the line $\boldsymbol{w}^H\boldsymbol{d_s} = 0$ anymore. As a result, the WNCM's processor

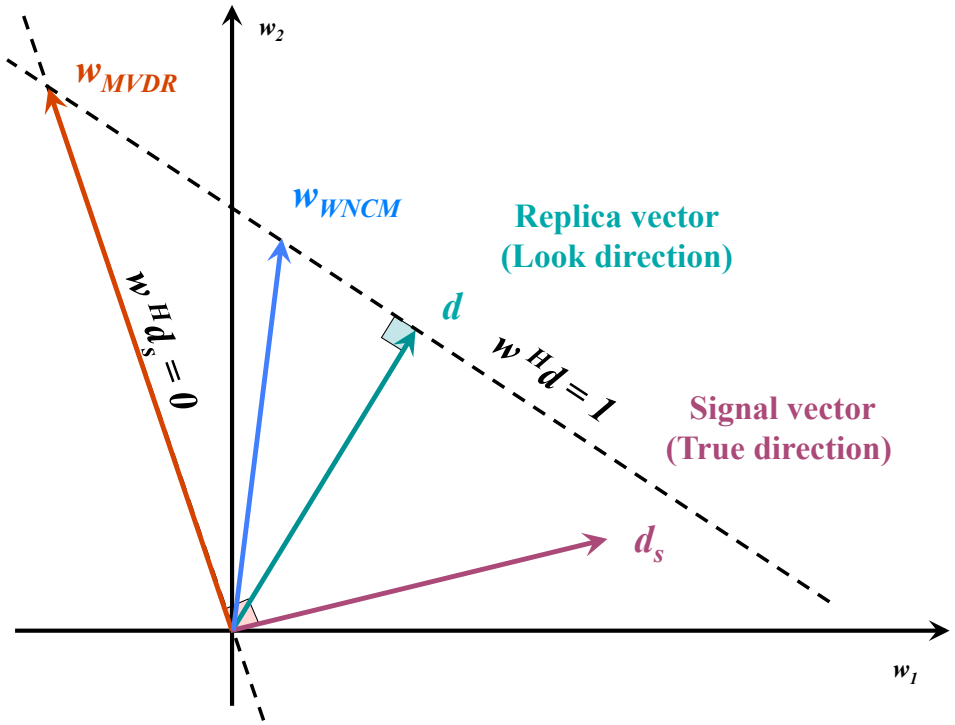

Figure 2.11: Construction of the WNCM weight vector. If the norm of the MVDR weight vector is bigger than the constraint set by the user, the right amount of white noise will be added to the CSDM such that $\boldsymbol{w}^H\boldsymbol{w} \leq \delta^{-2}$, and the WNCM weight vector's tip is found at the position along the $\boldsymbol{w}^H\boldsymbol{d} = 1$ line which guarantees the norm of the weight vector to be just under the value of the constraint, represented in blue. Signal suppression is therefore avoided in presence of environmental mismatch.

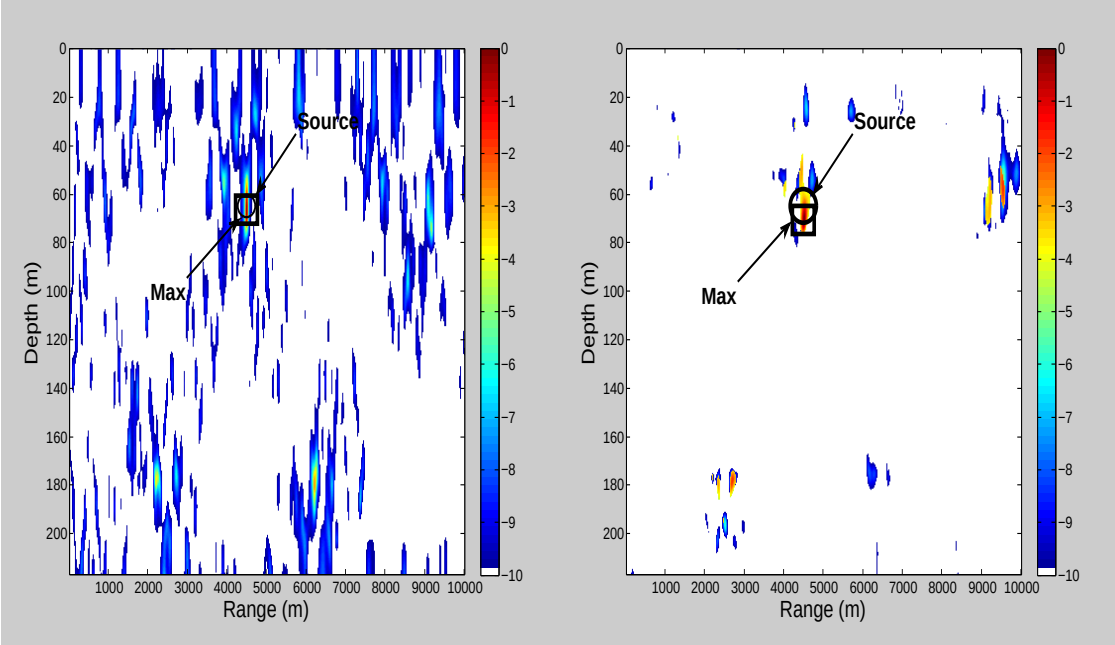

Figure 2.12: Simulated WNCM MFP at 49 Hz, constraint set at 7 dB down the maximum. The circle represent the position of the simulated source, and the square the position of the conventional algorithm's maximum.

Figure 2.13: Real data WNCM MFP at 49 Hz, constraint set at 7 dB down the maximum. The circle represent the position of the source, and the square the position of the conventional algorithm's maximum.

is more robust to mismatch than the MVDR one.

The performance of the algorithm is estimated using the same simulated and real data as in Sections 2.2.2 and 2.3.1. The value of the constraint δ^2 is set 7 dB down the maximum. The simulated WNCM ambiguity surface obtained is displayed on Fig. (2.12). The source is successfully localized and the simulated output is really close to the MVDR's one on Fig. (2.8). The median value of the ambiguity surface, -10.9 dB is nearly equal to the MVDR's one. Closer inspection show that some of the sidelobes are a little higher than in the MVDR's case, because of the CSDM's diagonal loading at those positions. In any case, both MVDR and WNCM processors perform comparably in this case and are able to locate the source.

The application of the WNCM's algorithm to experimental data is the real test, since the MVDR processor failed to localize the source on Fig. (2.9), and the conventional one did correctly assess its position, but with sidelobes so high that it precluded confident localization (see Fig. (2.7)).

The WNCM's output obtained using the data received on the array is given on Fig (2.13). This time the low sidelobe characteristic of the MVDR processor was not only maintained but improved (the median value is -15.8 dB). The widening of the main lobe due to the inequality constraint on the weight vector's norm allows the signal to pass through the algorithm, instead of being seen as an interfering signal and cancelled out as in the MVDR case. As a result, the WNCM is shown to be the most desirable method, since it is more robust to presence of environmental mismatch than the MVDR processor, and more discriminating than the conventional one.

The next section will extend these techniques to the broadband scenario, and investigate the difference in performance between combining the multiple frequencies coherently versus incoherently.

2.4 Broadband matched-field processing

Acoustic signals propagating in the ocean, would they be of natural or man-made nature are rarely narrowband. Usually, a wideband signal or a set of single-frequency tonals are received on the hydrophone array. This broadband information is then available to enhance MFP's localization performance.

There typically are two ways to combine information across frequency.

1. One can do an incoherent broadband processing [18, 19, 20], where single frequency power outputs are averaged in an effort to lower the sidelobes and increase the robustness of MFP to environmental uncertainties,

2. or one can exploit the cross-frequency complex information enlarging the data space and providing an extra-processing gain, with the drawback that these processors have to deal with the typically unknown complex spectral properties of the signal sent.

This section will present both techniques: incoherent and coherent, and compare the results obtained using simulated and experimental SwellEx-96 data. Different broadband processing methods, both in time and frequency domain will be presented.

2.4.1 Incoherent MFP

When the source broadcasts a broadband signal, one can create an ensemble of single-frequency ambiguity surfaces. Some of those power outputs might localize the source correctly, while other frequencies might be more sensitive to mismatch and show a maximum at the wrong position. In any case, those erroneous narrowband results still contain useful information since a high sidelobe often occurs at the true source position. Because the position of noise and signal sidelobes is usually frequency dependent, as opposed to the main lobe, a common approach proposed by Baggeroer *et al* is to incoherently average single-frequency ambiguity surfaces to suppress ambiguous sidelobes [18].

The incoherent processing can be done in two ways. One can perform a linear summation:

$$P_{IC\_linear}(r,z) = \frac{1}{L}\sum_{k=1}^{L} \boldsymbol{w}^H(k)\,\boldsymbol{R}(k)\,\boldsymbol{w}(k), \tag{2.27}$$

where L is number of single tones processed, or an addition in dB:

$$P_{IC\_dB}(r,z) = \frac{1}{L}\sum_{k=1}^{L} 10log\left[\boldsymbol{w}^H(k)\,\boldsymbol{R}(k)\,\boldsymbol{w}(k)\right]. \tag{2.28}$$

Since the dB scale produces comparable sidelobe powers [18], the summation in dB is favored and will be used in the rest of the document.

Note that the frequency dependent phases of the source spectrum $S(\omega)$ in Eq. 2.1 cancel out in the process of forming the narrowband CSDMs, and do not need to be included in the replica vector for single-frequency and incoherent MFP in order to match the data.

When the frequencies used in the averaging ensure that sidelobes have migrated by a distance equal to their half width, the sum provides a $5log(L)$ gain in

detectability [21] (as defined in Chapter 4) over narrowband results.

Czenszak and Krolik [22] have also shown through simulation that incoherent averaging increases robustness to mismatch over single frequency MFP when the environmental uncertainties caused a frequency-independent shift of the main lobe. Errors in channel depth and sediment parameters typically produce peak shifts independent of frequency while incorrect sound speed profiles lead to frequency-dependent ones.

2.4.2 Coherent MFP

Incoherent methods have been shown to lower sidelobe levels and increase robustness to environmental mismatch in cases. But despite enlarging the data space available to the processing, they still discard useful information by ignoring coherence across frequencies. When considering frequencies coherently, we increase the complexity of the impulse response between the source and receivers in the waveguide, and thus decrease the source localization ambiguity. Consequently, finding a way to combine the information across frequencies in a coherent way is the subject of current research. Broadband coherent methods, however are undoubtedly less computationally efficient than incoherent ones and have to overcome the difficulty of accurately predicting the phases of the acoustic field.

The first papers on broadband coherent MFP considered time-domain type of algorithms. Frequency domain methods were later developed in the literature. This section will present an overview of time and frequency domain processors at hand.

Time domain methods

C. S. Clay The earliest time-domain matched-field work has been credited to Clay [23]. He proposed to match measured and modeled impulse responses of transmission between the source and a receiver to estimate the source position. He also extended the method to multiple receivers by cross-correlating filter outputs of pairs of hydrophones. His technique however requires knowledge of the source function, or $S(\omega)$ in Eq. 2.1.

The method was applied to experimental data by Clay and Li [24, 25]. They successfully located a source using a single receiver in an almost ideal laboratory rigid waveguide [25]. They then added an hydrophone and introduced a deconvolution technique [24]. A map of cross correlations of the deconvolved signals by a theoretical impulse response gave the source location.

L. N. Frazer and P. I. Pecholcs Frazer and Pecholcs built on the already existing work and introduced five new types of single hydrophone algorithms [26]. They noted that localization is possible with a unique sensor as long as a large bandwidth of data is processed, suggesting a trade-off between number of elements and frequencies available.

They considered different types of norms and presented new localizer families, some of them requiring no *a priori* knowledge of the source function, instead estimating it as well as the source position. Simulated results showed that the processors worked best when the spectrum of the source was smooth. An extension to multiple hydrophones is also provided.

R. K. Brienzo and W. S. Hodgkiss Clay's time domain matched-field processor was successfully applied to experimental data coming from a short range (about 9 km) explosive source [27, 28]. Since low frequency acoustic energy has been shown to be least attenuated when propagating through water [29, 30], the direct arrival path was used as an estimate of the source waveform.

The effect of the experimental source waveform being very short (about 0.1s) but not quite an impulse function was investigated through simulations. It was shown to produce additional structure in the processor output, not sufficient to affect the source localization results in their case.

Y. P. Lee A couple years later, Lee successfully localized a long range broadband source (21 km away) as well, using experimental data on a single hydrophone [31]. Using a frequency domain representation of the matched-filtered data for different time delays, and estimating the singular value decomposition of the covariance matrix obtained, the author was able to isolate the source's impulse response from

the dominant surface scattered energy.

P. Hursky, M. B. Porter and M. Siderius More recently, Hursky *et al* investigated the performance of time domain MFP at high frequency (above 1 kHz) [32]. Since high frequencies are increasingly sensitive to fluctuations and model uncertainties, a number of techniques have been applied to overcome those limitations and track sources up to several kilometers in range.

Two data sets were used to demonstrate high frequency localization feasibility using one or two transducers. The source waveform is first assumed known and correlated to the received signal to retrieve the channel impulse response. This matched-filtered signal is then compared to a set of range/depth modeled impulse responses to infer the position of the source. Recognizing that in most cases the source waveform is not available for processing, the authors extended the method by cross-correlating the signals received on two hydrophones, canceling out by design the unknown source signature.

It was shown that tracking the source successfully required averaging successive experimental impulse responses, using the envelope of the data (discarding the phase information) and artificially increasing the bandwidth of the synthetic signal to minimize the effect of mismatch.

Frequency domain methods

E. K. Westwood Westwood was the first to introduce a coherent broadband matched-field processor operating in the frequency domain [33]. Similarly to the time domain techniques, cross-correlated measured impulse responses between pairs of receivers are matched against modeled ones, and the resulting complex function is summed coherently over frequencies. It differs from the time domain method introduced by Clay [23] in the sense that the output is not the maximum of the time-domain cross-correlation anymore, but the coherent summation of the single-frequency cross-correlations. The bandwidth on which the summation is performed can be chosen so as to maximize SNR.

In the frequency domain, cross-correlating the receivers 1 and 2's measured

signals at angular frequency ω is written as:

$$X_{\omega}^{(12)} = x_{\omega}^{(1)} x_{\omega}^{(2)*}, \tag{2.29}$$

where $*$ is the complex conjugate operation. Similarly, the modeled cross-correlation takes the form:

$$D_{\omega}^{(12)} = d_{\omega}^{(1)} d_{\omega}^{(2)*}. \tag{2.30}$$

The coherent processor output for two receivers is expressed as:

$$P_{Westwood}^{(12)}(r,z) = \frac{|\sum_{k=1}^{L} X_k^{(12)} D_k^{(12)*}|}{\left(\sum_{k=1}^{L} |D_k^{(12)}|\right)^{1/2} \left(\sum_{k=1}^{L} |X_k^{(12)}|\right)^{1/2}}. \tag{2.31}$$

The principle is the same for N hydrophones, the sum is performed for each of the $N(N-1)/2$ pairs:

$$P_{Westwood}(r,z) = \frac{|\sum_{p=1}^{N} \sum_{q=p+1}^{N} \sum_{k=1}^{L} X_k^{(pq)} D_k^{(pq)*}|}{\left(\sum_{p=1}^{N} \sum_{q=p+1}^{N} \sum_{k=1}^{L} |D_k^{(pq)}|\right)^{1/2} \left(\sum_{p=1}^{N} \sum_{q=p+1}^{N} \sum_{k=1}^{L} |X_k^{(pq)}|\right)^{1/2}}. \tag{2.32}$$

Note that since cross-correlation of measured spectra at the same frequency are involved, the unknown source phases cancel out by design and do not need to be estimated in this coherent scheme.

Also, the information coming from auto-spectra, or in other words the diagonal terms of the single frequencies CSDM has been discarded.

The method was applied to deep water experimental data, and the source was successfully tracked up to 42 km away from the receiving array. Factors as number of phones, array aperture and bandwidth used in the processing were investigated. As expected, using more phones, wider bandwidth and bigger aperture increased the quality of the localization. Adding the auto-correlation terms to the processing was shown to yield significant degradation of the peak to sidelobe/background levels, suggesting that those real terms might overpower the off-diagonal complex ones without contributing positively to the localization. Finally, the ambiguity surface obtained was found more discriminating than the incoherent processor.

S. P. Czenszak and J. L. Krolik Czenszak and Krolik followed the approach of Westwood, and matched the cross-spectra of the field to modeled cross spectra at different (r, z) [22]. This time, they used the auto-spectra information as well. This allowed them to formulate the algorithm in a quadratic form similar to those describing single-frequency MFP.

The cross-spectra information between pairs of elements at L frequencies is stacked in a $N \times N \times L$ column vector:

$$\widetilde{\boldsymbol{x}} = \Big[x_1^{(1)}x_1^{(1)*}, \ldots, x_1^{(1)}x_1^{(N)*}, \ldots, x_1^{(N)}x_1^{(1)*}, \ldots, x_1^{(N)}x_1^{(N)*}, \ldots, x_L^{(1)}x_L^{(1)*}, \ldots, x_L^{(1)}x_L^{(N)*}, \ldots, x_L^{(N)}x_L^{(1)*}, \ldots, x_L^{(N)}x_L^{(N)*}\Big]^T.$$

The cross-spectral density matrix involving the fourth order of the data is formed the usual way, where $\widetilde{\boldsymbol{x_k}}$ is data snapshot number k:

$$\widetilde{\boldsymbol{R}} = \frac{1}{K}\sum_{k=1}^{K} \widetilde{\boldsymbol{x_k}}\widetilde{\boldsymbol{x_k}}^H. \tag{2.33}$$

Similarly, a generalized weight vector $\widetilde{\boldsymbol{w}}(r, z)$ is implemented by stacking modeled cross-spectra coming from an hypothetical source at (r, z), and the conventional broadband coherent processor output is given by:

$$P_{Czenszak}(r, z) = \widetilde{\boldsymbol{w}}^H \widetilde{\boldsymbol{R}} \widetilde{\boldsymbol{w}}. \tag{2.34}$$

Note that as for Clay and Westwood's algorithms, the use of auto and cross-correlations of data from pairs of receivers at the same frequency prevents the user from having to estimate the unknown source phases.

One main advantage of formulating the coherent algorithm in the usual quadratic from is that it is straightforward to apply any type of adaptive matched-field processor. The authors recognized that a single-constrained adaptive processor as the MVDR in Sec. 2.3.1 would be very sensitive to mismatch, due to the increased number of degrees of freedom. They suggested the use of the Minimum Variance Environmental Perturbation Constraint algorithm (MV-EPC), previously developed by Krolik for single frequency scenarios [15].

The MV-EPC algorithm involves a set of linear constraints on modeled fields obtained from randomly perturbed environments, such that the output signal-to-noise ratio averaged over the ensemble of environmental realizations is maximized.

Simulated results demonstrated that the MV-EPC coherent broadband method yielded a percentage of correct localization of more than 90% out of 50 Monte-Carlo realizations versus 30% using an incoherent averaging of single frequency ambiguity surfaces. The side-lobe level was also lowered due to the extra degrees of freedom available from the cross-frequency information.

Z-H Michalopoulou and M. B. Porter This algorithm referred to as the MP algorithm is presented in detail because the next chapters will modify and adapt it to particular scenarios. As in typical single-frequency or incoherent broadband MFP scnenarios, Michalopoulou and Porter introduced a coherent algorithm based on matching received and modeled fields rather than cross-correlated pairs of fields [34]. However, the cross-frequency terms in the CSDM now include differences of source spectrum phases at pairs of frequencies. Ignoring those unknown terms in the implementation of the replica vector would implicity assume that the signal phase was constant accross frequencies. Such an hypothesis can result in a degradation of the source localization performance rendering any coherent processing detrimental to the process. The authors resorted to a normalization and cancellation scheme to get around the issue.

As proposed by Czenszak and Krolik, the received signal accross elements and frequencies is stacked in a $N \times L$ supervector.

$$\breve{\boldsymbol{x}} = \left[\; x_1^{(1)}, x_1^{(2)}, \ldots, x_1^{(N)}, \ldots, x_L^{(1)}, \ldots, x_L^{(N)} \; \right]^T . \tag{2.35}$$

From this supervector, a "super" CSDM can be constructed in the usual way, $\breve{\boldsymbol{R}} = E\{\breve{\boldsymbol{x}}\breve{\boldsymbol{x}}^H\}$. The MFP processor output can then be formulated as:

$$P_{MP}(r,z) = \breve{\boldsymbol{d}}^H \breve{\boldsymbol{R}} \breve{\boldsymbol{d}},$$

$$P_{MP}(r,z) = E\left[\left| \sum_{k=1}^{L} \boldsymbol{d}_k^H \boldsymbol{x}_k \right|^2 \right] . \tag{2.36}$$

Note that the position of the absolute value delimiters outside of the sum over frequencies makes this algorithm a coherent one and generates cross-frequency terms. In contrast, an incoherent algorithm sums absolute values of inner products:

$$P_{Incoh\_linear}\left(r,z\right) = E\left[\sum_{k=1}^{L}\left|\boldsymbol{d}_k^H\boldsymbol{x}_k\right|^2\right]. \tag{2.37}$$

As developed in Sec. 2.1.1, the noise-free complex signal received on the element i can be written as

$$x_\omega^{(i)} = S(\omega)G^{(i)}(0,z_i,R_s,Z_s,\omega), \tag{2.38}$$

where $S(\omega)$ is the complex fourier transformed source signal at the angular frequency ω, and $G^{(i)}(0,z_i,R_s,Z_s,\omega)$ the ocean waveguide's Green's function between the source location and the element i of the receiving array. Rewriting the output of the algorithm reveal that the unknown source phase remains to be evaluated, leaving the user with replicas mismatched with respect to the signal.

$$\begin{aligned} P_{MP}\left(r,z\right) &= \sum_{l=1}^{L}\sum_{k=1}^{L}\boldsymbol{d}_l^H\boldsymbol{x}_l\boldsymbol{x}_k^H\boldsymbol{d}_k \\ &= \sum_{l=1}^{L}\sum_{k=1}^{L}S(l)S(k)^*\boldsymbol{d}_l^H\boldsymbol{G}_l\boldsymbol{G}_k^H\boldsymbol{d}_k. \end{aligned} \tag{2.39}$$

The MP method addresses this issue [34, 35] by scaling the phase of each single-frequency subvector $\boldsymbol{x}_\omega$ by the phase on the first phone, and normalizing the subvector to unit length. This compensation procedure eliminates the unknown source terms in high signal-to-noise scenarios since, if we denote the new subvector by $\overline{\boldsymbol{x}}_\omega$:

$$\boldsymbol{x}_\omega = \begin{bmatrix} \left|S(\omega)G_\omega^{(1)}\right| e^{j\left(arg(S(\omega))+arg(G_\omega^{(1)})\right)} \\ \vdots \\ \left|S(\omega)G_\omega^{(N)}\right| e^{j\left(arg(S(\omega))+arg(G_\omega^{(N)})\right)} \end{bmatrix},$$

we have,

$$\overline{\boldsymbol{x}}_\omega = \frac{1}{\alpha}\begin{bmatrix} \left|G_\omega^{(1)}\right| e^{j0} \\ \vdots \\ \left|G_\omega^{(N)}\right| e^{j\left(arg(G_\omega^{(N)})-arg(G_\omega^{(1)})\right)} \end{bmatrix}, \tag{2.40}$$

where α is a coefficient of normalization.

When the amount of noise imbeded in the signal is not negligible anymore, the amplitude and phase normalization scheme described above does not cancel the unknown source terms in the noise component. The MP algorithm therefore carries an inherent mismatch when localizing low signal-to-noise ratio sources.

The authors applied the coherent broadband method to an experimental data set, and showed that the MVDR coherent processor tracked nearly perfectly the source in range and depth (in 90% of the cases) in comparison to 10% using an incoherent dB average of MVDR power outputs.

The normalization scheme was revisited in a later paper [35]. When the SNR is low at hydrophone number 1 the measurement of the phase is likely to be corrupted by the phase of the noise leading to uncorrect cancellation of the unknown source phases for the remaining hydrophones. A better choice would be to normalize by the phase of the hydrophone exhibiting the highest SNR, but the process is still subject to noise contamination. The authors proposed to use an estimate of the phase at the first phone by averaging phases coming from several snapshots instead.

T. Yang Yang recognized that deconvolving the received signal by the transfer function of the waveguide would yield the original signal waveform [36]. However, the implementation of the transfer function requires knowledge of the source position.

Incoherent average of single-frequency MFP outputs is implemented initially to estimate the source location. The transfer function at the given position is then computed and used to infer the source waveform. A coherent broadband processing approach is then made possible by adding the estimated source phases to the replica vectors at each frequency.

The technique applied on noise-free simulated signal showed that the reconstructed signal achieved a correlation of 0.998 with the original waveform, and the coherent broadband ambiguity surface displayed lower sidelobes than the incoherent one, in accord with the theoretical processing gain expected from the extra degrees of freedom generated by the cross-frequency information.

G. J. Orris, M. Nicholas and J. S. Perkins Orris *et al* investigated coherent multi-frequency MFP using experimental data [37]. They considered the unknown source phases as free parameters to be determined using an otimization method. MFP is therefore used in the context of an inversion problem, where a set of environmental or source related parameters are scanned to give the best estimate of the signal field.

The optimization problem is written as:

$$\min_{\{arg(S(k))\in[0,2\pi)\forall k=[1..L],r,z\}}[1-\frac{1}{L\left(L-1\right)}\sum_{nm}e^{-i(arg(S(m))-arg(S(n)))}\boldsymbol{d}_m^H\boldsymbol{R}_{m,n}\boldsymbol{d}_n], \quad (2.41)$$

where $\boldsymbol{R}_{m,n}$ is the cross spectral density matrix obtained from the cross between snapshots at frequencies ω_m and ω_n. Only the cross-frequency terms are considered in this coherent scheme

To avoid being too computationally cumbersome and still give a reasonable estimate of the source phase, the search has to be limited to a couple frequencies only. Note that the phase outputted by the processor might differ from the actual original source phase since the estimation is made after propagation of the signal through the waveguide and corruption by noise.

The method was tested using five tonals of the real data set. The range resolution was shown to be greatly improved in comparison with the incoherent method, and the depth estimate was found close to the actual source depth, allowing a more precise localization of the source. Additionaly, as much as five decibel enhancement in the peak-to-sidelobe ratio at low SNR was achieved.

Comparison of the amount of data exploited by each coherent method

The broadband techniques presented in the previous section combine data across frequencies in a slightly different manner. Not only the way the single frequency outputs are treated varies from one method to the other, but some of the techniques involve a direct comparison of the fields while other form cross-correlations of pairs of fields at different elements. As a result, some of the algorithms use a bigger portion of the data information available than the others.

To better visualize the amount of information exploited by each method, we

look at the dimension of the CSDM associated. The simple case of a two receiver array recording data at two single frequencies is considered. Only the frequency domain broadband techniques introduced in Sec. 2.4.1 and 2.4.2 are involved in the comparison.

Two main types of algorithms have been presented:

1. The methods matching complex fields at the elements to simulated fields at hypothetical source positions, which typically have to deal with the unknown source spectrum with application of a coherent processor (incoherent MFP, Z-H Michalopoulou and M. B. Porter's coherent MFP),

2. The ones matching correlations of pairs of receivers outputs to correlation of pairs of receivers simulated outputs, where the source phase is cancelled out by design (E. K. Westwood coherent MFP and S. P. Czenszak and J. L. Krolik coherent MFP).

Figure (2.14) illustrates the amount of the coherent cross-spectral density matrix exploited by the incoherent processor. The subscript designates the frequency index and the superscript the element number. The cross-frequency information is ignored, and only the outer-product of the received field at single-frequency is used.

In contrast, the coherent method developed by Z-H Michalopoulou and M. B. Porter uses the full extent of the cross-spectral density matrix formed by phase-correcting and normalizing the narrowband outputs to remove the unknown source phases, as apparent in Fig. (2.15). The increase in data space provides more resolution and a wider dynamic range between the main-lobe and background level at the output of the processor.

The next type of algorithms uses the fourth-order moment of the data by matching cross-correlations of pairs of receiver outputs. The data space is therefore increased by the number of elements squared.

Figure (2.16) shows the portion of the corresponding CSDM used by E. K. Westwood's method. Only cross-correlations between different receivers are kept.

S. P. Czenszak and J. L. Krolik's method, in contrast, uses the full fourth-order moment CSDM, as seen on Fig. (2.17).

$x_1^{(1)} * x_1^{(1)}$	$x_1^{(1)} * x_1^{(2)}$	$x_1^{(1)} * x_2^{(1)}$	$x_1^{(1)} * x_2^{(2)}$
$x_1^{(2)} * x_1^{(1)}$	$x_1^{(2)} * x_1^{(2)}$	$x_1^{(2)} * x_2^{(1)}$	$x_1^{(2)} * x_2^{(2)}$
$x_2^{(1)} * x_1^{(1)}$	$x_2^{(1)} * x_1^{(2)}$	$x_2^{(1)} * x_2^{(1)}$	$x_2^{(1)} * x_2^{(2)}$
$x_2^{(2)} * x_1^{(1)}$	$x_2^{(2)} * x_1^{(2)}$	$x_2^{(2)} * x_2^{(1)}$	$x_2^{(2)} * x_2^{(2)}$

Figure 2.14: Coherent cross-spectral density matrix for the two-receiver array, two frequencies processed scenario obtained by forming the outer product of the received field. The portion of the data matrix involved in the incoherent processing is shown in blue. Half of the available information is exploited by the incoherent algorithm.

Figure 2.15: Coherent cross-spectral density matrix for the two-receiver array, two frequencies processed scenario obtained by forming the outer product of the received field. The portion of the data matrix involved in the algorithm developed by Z-H. Michalopoulou and M. Porter is shown in blue. As opposed to the incoherent method the cross-frequency information is exploited by the algorithm. Note that the data has however been modified to discard the unknown source spectrum's information.

$x_1^{(1)}x_1^{(1)*}$ × $x_1^{(1)*}x_1^{(1)}$	$x_1^{(1)}x_1^{(1)*}$ × $x_1^{(1)*}x_1^{(2)}$	$x_1^{(1)}x_1^{(1)*}$ × $x_1^{(2)*}x_1^{(1)}$	$x_1^{(1)}x_1^{(1)*}$ × $x_1^{(2)*}x_1^{(2)}$	$x_1^{(1)}x_1^{(1)*}$ × $x_2^{(1)*}x_2^{(1)}$	$x_1^{(1)}x_1^{(1)*}$ × $x_2^{(1)*}x_2^{(2)}$	$x_1^{(1)}x_1^{(1)*}$ × $x_2^{(2)*}x_2^{(1)}$	$x_1^{(1)}x_1^{(1)*}$ × $x_2^{(2)*}x_2^{(2)}$
$x_1^{(1)}x_1^{(2)*}$ × $x_1^{(1)*}x_1^{(1)}$	$x_1^{(1)}x_1^{(2)*}$ × $x_1^{(1)*}x_1^{(2)}$	$x_1^{(1)}x_1^{(2)*}$ × $x_1^{(2)*}x_1^{(1)}$	$x_1^{(1)}x_1^{(2)*}$ × $x_1^{(2)*}x_1^{(2)}$	$x_1^{(1)}x_1^{(2)*}$ × $x_2^{(1)*}x_2^{(1)}$	$x_1^{(1)}x_1^{(2)*}$ × $x_2^{(1)*}x_2^{(2)}$	$x_1^{(1)}x_1^{(2)*}$ × $x_2^{(2)*}x_2^{(1)}$	$x_1^{(1)}x_1^{(2)*}$ × $x_2^{(2)*}x_2^{(2)}$
$x_1^{(2)}x_1^{(1)*}$ × $x_1^{(1)*}x_1^{(1)}$	$x_1^{(2)}x_1^{(1)*}$ × $x_1^{(1)*}x_1^{(2)}$	$x_1^{(2)}x_1^{(1)*}$ × $x_1^{(2)*}x_1^{(1)}$	$x_1^{(2)}x_1^{(1)*}$ × $x_1^{(2)*}x_1^{(2)}$	$x_1^{(2)}x_1^{(1)*}$ × $x_2^{(1)*}x_2^{(1)}$	$x_1^{(2)}x_1^{(1)*}$ × $x_2^{(1)*}x_2^{(2)}$	$x_1^{(2)}x_1^{(1)*}$ × $x_2^{(2)*}x_2^{(1)}$	$x_1^{(2)}x_1^{(1)*}$ × $x_2^{(2)*}x_2^{(2)}$
$x_1^{(2)}x_1^{(2)*}$ × $x_1^{(1)*}x_1^{(1)}$	$x_1^{(2)}x_1^{(2)*}$ × $x_1^{(1)*}x_1^{(2)}$	$x_1^{(2)}x_1^{(2)*}$ × $x_1^{(2)*}x_1^{(1)}$	$x_1^{(2)}x_1^{(2)*}$ × $x_1^{(2)*}x_1^{(2)}$	$x_1^{(2)}x_1^{(2)*}$ × $x_2^{(1)*}x_2^{(1)}$	$x_1^{(2)}x_1^{(2)*}$ × $x_2^{(1)*}x_2^{(2)}$	$x_1^{(2)}x_1^{(2)*}$ × $x_2^{(2)*}x_2^{(1)}$	$x_1^{(2)}x_1^{(2)*}$ × $x_2^{(2)*}x_2^{(2)}$
$x_2^{(1)}x_2^{(1)*}$ × $x_1^{(1)*}x_1^{(1)}$	$x_2^{(1)}x_2^{(1)*}$ × $x_1^{(1)*}x_1^{(2)}$	$x_2^{(1)}x_2^{(1)*}$ × $x_1^{(2)*}x_1^{(1)}$	$x_2^{(1)}x_2^{(1)*}$ × $x_1^{(2)*}x_1^{(2)}$	$x_2^{(1)}x_2^{(1)*}$ × $x_2^{(1)*}x_2^{(1)}$	$x_2^{(1)}x_2^{(1)*}$ × $x_2^{(1)*}x_2^{(2)}$	$x_2^{(1)}x_2^{(1)*}$ × $x_2^{(2)*}x_2^{(1)}$	$x_2^{(1)}x_2^{(1)*}$ × $x_2^{(2)*}x_2^{(2)}$
$x_2^{(1)}x_2^{(2)*}$ × $x_1^{(1)*}x_1^{(1)}$	$x_2^{(1)}x_2^{(2)*}$ × $x_1^{(1)*}x_1^{(2)}$	$x_2^{(1)}x_2^{(2)*}$ × $x_1^{(2)*}x_1^{(1)}$	$x_2^{(1)}x_2^{(2)*}$ × $x_1^{(2)*}x_1^{(2)}$	$x_2^{(1)}x_2^{(2)*}$ × $x_2^{(1)*}x_2^{(1)}$	$x_2^{(1)}x_2^{(2)*}$ × $x_2^{(1)*}x_2^{(2)}$	$x_2^{(1)}x_2^{(2)*}$ × $x_2^{(2)*}x_2^{(1)}$	$x_2^{(1)}x_2^{(2)*}$ × $x_2^{(2)*}x_2^{(2)}$
$x_2^{(2)}x_2^{(1)*}$ × $x_1^{(1)*}x_1^{(1)}$	$x_2^{(2)}x_2^{(1)*}$ × $x_1^{(1)*}x_1^{(2)}$	$x_2^{(2)}x_2^{(1)*}$ × $x_1^{(2)*}x_1^{(1)}$	$x_2^{(2)}x_2^{(1)*}$ × $x_1^{(2)*}x_1^{(2)}$	$x_2^{(2)}x_2^{(1)*}$ × $x_2^{(1)*}x_2^{(1)}$	$x_2^{(2)}x_2^{(1)*}$ × $x_2^{(1)*}x_2^{(2)}$	$x_2^{(2)}x_2^{(1)*}$ × $x_2^{(2)*}x_2^{(1)}$	$x_2^{(2)}x_2^{(1)*}$ × $x_2^{(2)*}x_2^{(2)}$
$x_2^{(2)}x_2^{(2)*}$ × $x_1^{(1)*}x_1^{(1)}$	$x_2^{(2)}x_2^{(2)*}$ × $x_1^{(1)*}x_1^{(2)}$	$x_2^{(2)}x_2^{(2)*}$ × $x_1^{(2)*}x_1^{(1)}$	$x_2^{(2)}x_2^{(2)*}$ × $x_1^{(2)*}x_1^{(2)}$	$x_2^{(2)}x_2^{(2)*}$ × $x_2^{(1)*}x_2^{(1)}$	$x_2^{(2)}x_2^{(2)*}$ × $x_2^{(1)*}x_2^{(2)}$	$x_2^{(2)}x_2^{(2)*}$ × $x_2^{(2)*}x_2^{(1)}$	$x_2^{(2)}x_2^{(2)*}$ × $x_2^{(2)*}x_2^{(2)}$

Figure 2.16: Coherent cross-spectral density matrix for the two-receiver array, two frequencies processed scenario obtained by forming the outer product of the correlated field between pairs of receivers. The portion of the data matrix involved in the algorithm developed by Z-E. K. Westwood is shown in blue. The autocorrelations are excluded from the processing.

$x_1^{(1)}x_1^{(1)*}$ × $x_1^{(1)*}x_1^{(1)}$	$x_1^{(1)}x_1^{(1)*}$ × $x_1^{(1)*}x_1^{(2)}$	$x_1^{(1)}x_1^{(1)*}$ × $x_1^{(2)*}x_1^{(1)}$	$x_1^{(1)}x_1^{(1)*}$ × $x_1^{(2)*}x_1^{(2)}$	$x_1^{(1)}x_1^{(1)*}$ × $x_2^{(1)*}x_2^{(1)}$	$x_1^{(1)}x_1^{(1)*}$ × $x_2^{(1)*}x_2^{(2)}$	$x_1^{(1)}x_1^{(1)*}$ × $x_2^{(2)*}x_2^{(1)}$	$x_1^{(1)}x_1^{(1)*}$ × $x_2^{(2)*}x_2^{(2)}$
$x_1^{(1)}x_1^{(2)*}$ × $x_1^{(1)*}x_1^{(1)}$	$x_1^{(1)}x_1^{(2)*}$ × $x_1^{(1)*}x_1^{(2)}$	$x_1^{(1)}x_1^{(2)*}$ × $x_1^{(2)*}x_1^{(1)}$	$x_1^{(1)}x_1^{(2)*}$ × $x_1^{(2)*}x_1^{(2)}$	$x_1^{(1)}x_1^{(2)*}$ × $x_2^{(1)*}x_2^{(1)}$	$x_1^{(1)}x_1^{(2)*}$ × $x_2^{(1)*}x_2^{(2)}$	$x_1^{(1)}x_1^{(2)*}$ × $x_2^{(2)*}x_2^{(1)}$	$x_1^{(1)}x_1^{(2)*}$ × $x_2^{(2)*}x_2^{(2)}$
$x_1^{(2)}x_1^{(1)*}$ × $x_1^{(1)*}x_1^{(1)}$	$x_1^{(2)}x_1^{(1)*}$ × $x_1^{(1)*}x_1^{(2)}$	$x_1^{(2)}x_1^{(1)*}$ × $x_1^{(2)*}x_1^{(1)}$	$x_1^{(2)}x_1^{(1)*}$ × $x_1^{(2)*}x_1^{(2)}$	$x_1^{(2)}x_1^{(1)*}$ × $x_2^{(1)*}x_2^{(1)}$	$x_1^{(2)}x_1^{(1)*}$ × $x_2^{(1)*}x_2^{(2)}$	$x_1^{(2))}x_1^{(1)*}$ × $x_2^{(2)*}x_2^{(1)}$	$x_1^{(2)}x_1^{(1)*}$ × $x_2^{(2)*}x_2^{(2)}$
$x_1^{(2)}x_1^{(2)*}$ × $x_1^{(1)*}x_1^{(1)}$	$x_1^{(2)}x_1^{(2)*}$ × $x_1^{(1)*}x_1^{(2)}$	$x_1^{(2)}x_1^{(2)*}$ × $x_1^{(2)*}x_1^{(1)}$	$x_1^{(2)}x_1^{(2)*}$ × $x_1^{(2)*}x_1^{(2)}$	$x_1^{(2)}x_1^{(2)*}$ × $x_2^{(1)*}x_2^{(1)}$	$x_1^{(2)}x_1^{(2)*}$ × $x_2^{(1)*}x_2^{(2)}$	$x_1^{(2)}x_1^{(2)*}$ × $x_2^{(2)*}x_2^{(1)}$	$x_1^{(2)}x_1^{(2)*}$ × $x_2^{(2)*}x_2^{(2)}$
$x_2^{(1)}x_2^{(1)*}$ × $x_1^{(1)*}x_1^{(1)}$	$x_2^{(1)}x_2^{(1)*}$ × $x_1^{(1)*}x_1^{(2)}$	$x_2^{(1)}x_2^{(1)*}$ × $x_1^{(2)*}x_1^{(1)}$	$x_2^{(1)}x_2^{(1)*}$ × $x_1^{(2)*}x_1^{(2)}$	$x_2^{(1)}x_2^{(1)*}$ × $x_2^{(1)*}x_2^{(1)}$	$x_2^{(1)}x_2^{(1)*}$ × $x_2^{(1)*}x_2^{(2)}$	$x_2^{(1)}x_2^{(1)*}$ × $x_2^{(2)*}x_2^{(1)}$	$x_2^{(1)}x_2^{(1)*}$ × $x_2^{(2)*}x_2^{(2)}$
$x_2^{(1)}x_2^{(2)*}$ × $x_1^{(1)*}x_1^{(1)}$	$x_2^{(1)}x_2^{(2)*}$ × $x_1^{(1)*}x_1^{(2)}$	$x_2^{(1)}x_2^{(2)*}$ × $x_1^{(2)*}x_1^{(1)}$	$x_2^{(1)}x_2^{(2)*}$ × $x_1^{(2)*}x_1^{(2)}$	$x_2^{(1)}x_2^{(2)*}$ × $x_2^{(1)*}x_2^{(1)}$	$x_2^{(1)}x_2^{(2)*}$ × $x_2^{(1)*}x_2^{(2)}$	$x_2^{(1)}x_2^{(2)*}$ × $x_2^{(2)*}x_2^{(1)}$	$x_2^{(1)}x_2^{(2)*}$ × $x_2^{(2)*}x_2^{(2)}$
$x_2^{(2)}x_2^{(1)*}$ × $x_1^{(1)*}x_1^{(1)}$	$x_2^{(2)}x_2^{(1)*}$ × $x_1^{(1)*}x_1^{(2)}$	$x_2^{(2)}x_2^{(1)*}$ × $x_1^{(2)*}x_1^{(1)}$	$x_2^{(2)}x_2^{(1)*}$ × $x_1^{(2)*}x_1^{(2)}$	$x_2^{(2)}x_2^{(1)*}$ × $x_2^{(1)*}x_2^{(1)}$	$x_2^{(2)}x_2^{(1)*}$ × $x_2^{(1)*}x_2^{(2)}$	$x_2^{(2)}x_2^{(1)*}$ × $x_2^{(2)*}x_2^{(1)}$	$x_2^{(2)}x_2^{(1)*}$ × $x_2^{(2)*}x_2^{(2)}$
$x_2^{(2)}x_2^{(2)*}$ × $x_1^{(1)*}x_1^{(1)}$	$x_2^{(2)}x_2^{(2)*}$ × $x_1^{(1)*}x_1^{(2)}$	$x_2^{(2)}x_2^{(2)*}$ × $x_1^{(2)*}x_1^{(1)}$	$x_2^{(2)}x_2^{(2)*}$ × $x_1^{(2)*}x_1^{(2)}$	$x_2^{(2)}x_2^{(2)*}$ × $x_2^{(1)*}x_2^{(1)}$	$x_2^{(2)}x_2^{(2)*}$ × $x_2^{(1)*}x_2^{(2)}$	$x_2^{(2)}x_2^{(2)*}$ × $x_2^{(2)*}x_2^{(1)}$	$x_2^{(2)}x_2^{(2)*}$ × $x_2^{(2)*}x_2^{(2)}$

Figure 2.17: Coherent cross-spectral density matrix for the two-receiver array, two frequencies processed scenario obtained by forming the outer product of the correlated field between pairs of receivers. The portion of the data matrix involved in the algorithm developed by S. P. Czenszak and J. L. Krolik is shown in blue.

While using a bigger portion of the information available in the data offers additional opportunity over more traditional methods like the incoherent algorithm, the increased data space also comes with a larger snapshot requirement. Indeed, at least twice the dimension of the CSDM number of snapshots have to be accumulated to form a well-defined invertible CSDM, suitable for adaptive MFP. During that time, the acoustic sources and interferers have to remain in a single range-depth resolution cell to avoid smearing of the main-lobe over continuous cells. This hypothesis, already strained for traditional methods can become problematic as the data space dimension becomes larger. Sensitivity to environmental mismatch is also aggravated.

Hence, using the fourth-order moment of the data is theoretically advantageous but not very practical. Methods correlating the modeled and received acoustic fields (*ie* using second-order moment of the data) are therefore favored in the rest of this dissertation.

Conventional coherent and incoherent broadband results

Amongst the diverse coherent methods presented in this chapter, we chose to study the one developed by Michalopoulou and Porter (MP). Its simple formulation in the frequency domain and use of the field information as opposed to cross-correlations between receivers makes it readily comparable to single-frequency and incoherent multi-frequency techniques already described. It is also straightforward to extend the MP coherent method to any kind of adaptive processing.

In this section, we compare the performance of conventional incoherent and coherent MP broadband MFP to single-frequency MFP, using simulated and experimental data. To be consistent with the single-frequency study of Section 2.2, the same portion of the SWellEx-96 experiment is processed, this time using the full 13 high level set of tonals.

Both simulated and experimental results are explored. Complex source spectrum terms are introduced in the simulated signal for each frequency, and assumed unknown for the rest of the processing. The same environment and parameters detailed in Sec. 2.2.2 are used to create the broadband conventional coherent

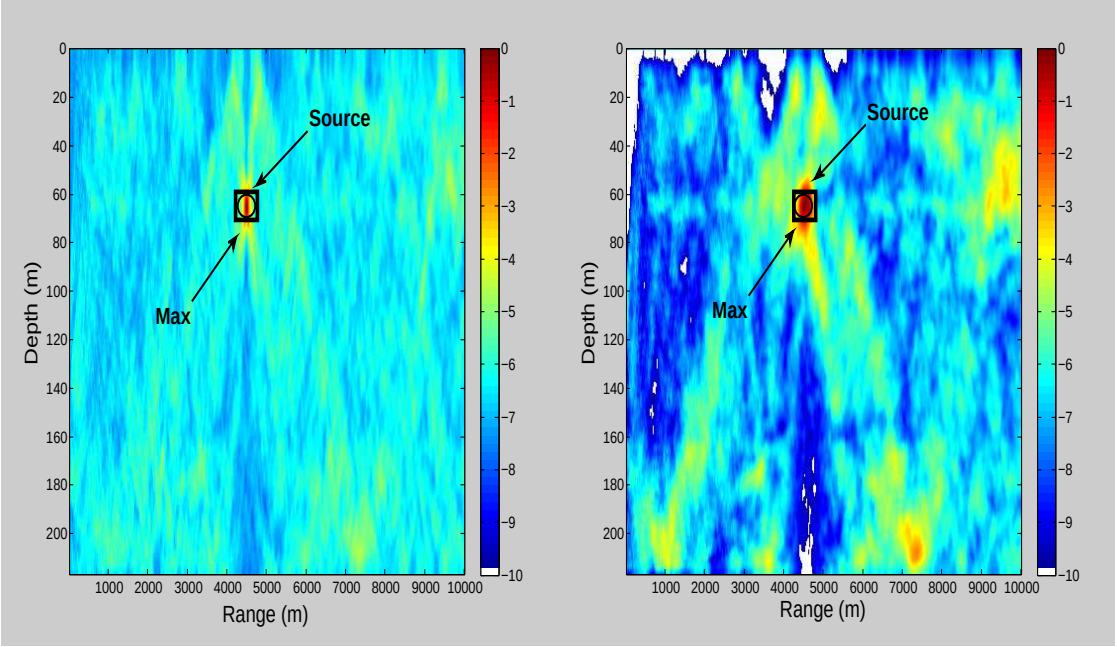

Figure 2.18: Simulated incoherent conventional MFP output obtained by dB-averaging 13 single-frequency outputs. The circle represent the position of the simulated source, and the square the position of the conventional algorithm's maximum.

Figure 2.19: Real data incoherent conventional MFP output obtained by dB-averaging 13 single-frequency outputs. The circle represent the position of the source, and the square the position of the conventional algorithm's maximum.

and incoherent ambiguity surfaces. Figures (2.18) and (2.19) display the simulated and experimental localization results obtained while incoherently averaging in dB the 13 single-frequency ambiguity surfaces.

Comparing those results to the simulated and experimental single-frequency ambiguity surfaces obtained by processing data at 49Hz in Figs. (2.6) and (2.7) show that averaging outputs in frequency does not affect the background and median level too much, but does lower the sidelobe level significantly, by 3 to 5 dB in this case. This is consistent with the assumption that averaging the narrowband ambiguities in dB should provide an additional gain over narrowband processing of $5log\,(L) = 5log\,(13) = 5.6dB$ in this case [21]

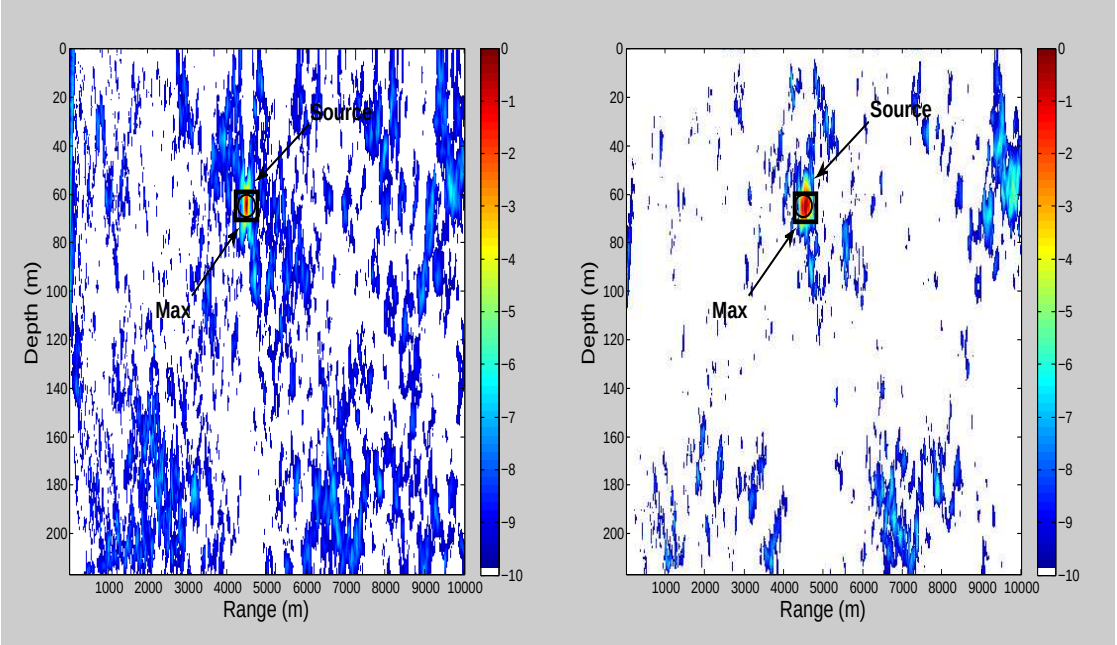

Figure 2.20: Simulated coherent conventional MFP output obtained by using the MP algorithm. The circle represent the position of the simulated source, and the square the position of the conventional algorithm's maximum.

Figure 2.21: Real data coherent conventional MFP output obtained by using the MP algorithm. The circle represent the position of the source, and the square the position of the conventional algorithm's maximum.

The same portion of the real and synthetic data is now processed coherently accross frequencies, using the MP conventional matched-field algorithm. Figures (2.20) and (2.21) show the simulated and experimental coherent ambiguity surfaces obtained.

The additional gain obtained by processing the frequencies coherently rather than incoherently is quite noticeable, since the the basal noise level, sidelobes and median levels are reduced by 5 to 8 dB.

In the MP algorithm, additional frequencies are stacked in a big "supervector" and in effect increase the dimension of the CSDM as if more array elements were present. When the array is steered at the true source position, the signal

is summed coherently along the receivers but also accross frequencies, while the incoherent part of the noise adds incoherently. A formal study of the extra processing gain associated is provided in Chapter 4. The "coherent gain" was shown to be a function of the input SNR, and reach a maximum of $N \times L$ for high SNR scenarios.

We found an additional processing gain of about 10 dB using the MP coherent algorithm over narrowband processing and 5 dB using the MP coherent algorithm versus an incoherent average of the single-frequency outputs. This is consistent with the theoretical $10log\,(L) = 10log\,(13) = 11.1dB$ and $5log\,(L) = 5log\,(13) = 5.6dB$ at high input SNR.

This dissertation work aims at enhancing broadband coherent MFP's performance (1) in presence of environmental mismatch, (2) for weak sources and (3) in high frequency scenarios. The white noise constraint algorithm is combined with coherent broadband techniques in a published study presented in Chapter 3, in an effort to increase robustness to model mismatch and mitigate the snapshot deficiency issue. Chapter 4 investigates localization at low signal-to-noise ratio and introduces a "fully-coherent" broadband algorithm to detect weak sources. Finally, Chapter 5 applies the coherent broadband methods to localization of high-frequency sources, and proposes a singular value decomposition technique over perturbed propagating environments to mitigate the effect of sound speed fluctuations in the medium.

Bibliography

[1] R. O. Nielsen. *Sonar signal processing*. Artech House, 1991.

[2] A. B. Baggeroer, W. A. Kuperman, and P. N. Mikhalevsky. An overview of matched field methods in ocean acoustics. *IEEE Journal of Oceanic engineering*, 18(4):401–424, october 1993.

[3] F. B. Jensen, W. A. Kuperman, M. B. Porter, and H. Schmidt. *Computational Ocean Acoustics*. Springer-Verlag New York, Inc., 2000.

[4] A. B. Baggeroer and H. Cox. Passive sonar limits upon nulling mulyiple moving ships with large aperture arrays. *Proceedings of the IEEE, 33rd Asilomar Conference on Signals, Systems Computing*, pages 103–108, 1999.

[5] H. C. Song, W. A. Kuperman, W. S. Hodgkiss, P. Gerstoft, and J. S. Kim. Null broadening with snapshot-deficient covariance matrices in passive sonar. *IEEE Journal of Oceanic engineering*, 28:250–261, 2003.

[6] Homer P. Bucker. Use of calculated sound fields and matched-field detection to locate sound sources in shallow water. *J. Acoust. Soc. Am.*, 59(2):368–373, February 1976.

[7] R. G. Fizell and S. C. Wales. Source localization in range and depth in an artic environment. *J. Acoust. Soc. Am., Suppl.*, (78):S57, 1985.

[8] N. O. Booth, A. R. Abawi, P. W. Schey, and W. S. Hodgkiss. Detectability of low-level broad-band signals using adaptive matched-field processing with vertical aperture arrays. *IEEE Journal of Oceanic engineering*, 25(3):296–313, July 2000.

[9] www.mpl.ucsd.edu/swellex96/s5.htm, 1996.

[10] H. L. Van Trees. *Optimum Array Processing, part IV of Detection, Estimation, and Modulation Theory*. Wiley-interscience, 2002.

[11] J. N. Maksym. A robust formulation of an optimum cros-spectral beamformer for line arrays. *J. Acoust. Soc. Am.*, 65(4):971–975, April 1979.

[12] A. Tolstoy. *Matched Field Processing for Underwater Acoustics*. World Scientific, Singapore, 1992.

[13] J. V. Candy and J. Sullivan. Model-based identification: An adaptive approach to ocean-acoustic processing. *IEEE Journal of Oceanic engineering*, 21:273–289, 1996.

[14] H. Cox, R. M. Zeskind, and M. M. Owen. Robust adaptive beamforming. *IEEE Transactions on Acoustics, Speech and Signal Processing*, 35(10):1365–1376, October 1987.

[15] J. L. Krolik. Matched-field minimum variance beamforming in a random ocean channel. *J. Acoust. Soc. Am.*, 92:1408–1419, 1992.

[16] H. S. Schmidt, A. B. Baggeroer, W. A. Kuperman, and E. K. Scheer. Environmentally tolerant beamforming for high-resolution matched-field processing: Deterministic mismatch. *J. Acoust. Soc. Am.*, 73:813–825, 1979.

[17] H. A. Chandler, C. Feuillade, and G. B. Smith. Sector-focused processing for stabilized resolution of multiple acoustic sources. *J. Acoust. Soc. Am.*, 97:2159–2172, 1995.

[18] A. B. Baggeroer, W. A. Kuperman, and H. Schmidt. Matched-field processing: Source localization in correlated noise as an optimum parameter estimation problem. *J. Acoust. Soc. Am.*, 83:571–587, 1988.

[19] N. Booth and P. Schey. Broadband matched-field processing of low level signals in shallow water. *J. Acoust. Soc. Am.*, 97:3291 (A), 1995.

[20] W. S. Hodgkiss, K. H. Kim, J. J. Murray, and J. L. Krolik. Robust mfp processor performance with swellex data. Esquimalt Defense Research Detachment, Victoria, BC, 12-14 June 1996. presentation at the 8th International Workshop on MFP and Model-Based Signal Processing.

[21] G. B. Smith, C. Feuillade, and D. R. DelBalzo. Matched-field processing enhancement in a shallow-water environment by incoherent broadband averaging. *J. Acoust. Soc. Am.*, 91:1447–1455, 1992.

[22] S. P. Czenszak and J. L. Krolik. Robust wideband matched-field processing with a short vertical array. *J. Acoust. Soc. Am.*, 101(2):749–759, February 1997.

[23] C. S. Clay. Optimum time domain signal transmission and source localization in a waveguide. *J. Acoust. Soc. Am.*, 81:660–664, 1987.

[24] C. S. Clay and S. Li. Optimum time domain signal transmission and source localization in a waveguide: Matched filter and deconvolution experiments. *J. Acoust. Soc. Am.*, 83:1377–1383, 1988.

[25] S. Li and C. S. Clay. Optimum time domain signal transmission and source localization in a waveguide: Experiments in an ideal wedge waveguide. *J. Acoust. Soc. Am.*, 82:1409–1417, 1987.

[26] L. N. Frazer and P. I. Pecholcs. Single-hydrophone localization. *J. Acoust. Soc. Am.*, 88:995–1002, 1990.

[27] R. K. Brienzo and W. S. Hodgkiss. Broadband matched-field processing. *J. Acoust. Soc. Am.*, 94:2821–2831, 1993.

[28] W. S. Hodgkiss and R. K. Brienzo. Broadband source detection and range/depth localization via full-wavefield (matched-field) processing. *Proc. ICASSP-90*, (2743-2747), April 1990.

[29] A. C. Kibblewhite and L. D. Hampton. A review od deep ocean sound attenuation at very low frequencies. *J. Acoust. Soc. Am.*, 67:147–157, 1980.

[30] R. J. Urick. *Principles of Underwater Sound*. p 106. McGraw-Hill, New-York, 1983.

[31] Y. P. Lee. Time-domain single hydrophone localization in a real shallow water environment. *IEEE Journal of Oceanic engineering*, pages 1074–1077, 1998.

[32] P. Hursky, M. B. Porter, and M. Siderius. High frequency (8-16 hz) model-base source localization. *J. Acoust. Soc. Am.*, 115:3021–3032, 2004.

[33] E. K. Westwood. Broadband matched-field source localization. *J. Acoust. Soc. Am.*, 91(5):2777–2789, May 1992.

[34] Z.-H. Michalopoulou and M. B. Porter. Matched-field processing for broadband source localization. *IEEE Journal of Oceanic engineering*, 21:384–392, 1996.

[35] Z.-H. Michalopoulou. Robust multi-tonal matched-field inversion: A coherent approach. *J. Acoust. Soc. Am.*, 104:163–170, 1998.

[36] T. Yang. Broadband source localization and signature estimation. *J. Acoust. Soc. Am.*, 93:1797–1806, 1993.

[37] G. J. Orris, M. Nicholas, and J. S. Perkins. The matched-phase coherent multi-frequency matched-field processor. *J. Acoust. Soc. Am.*, 107(5):2563–2575, 2000.

Chapter 3

Coherent broadband white noise constraint processing

3.1 Abstract

Adaptive matched-field processing (MFP) is not only very sensitive to mismatch, but also requires the received sound levels to exceed a threshold signal-to-noise ratio. Furthermore, acoustic sources and interferers have to move slowly enough across resolution cells so that a full rank cross-spectral density matrix can be constructed. Coherent-broadband MFP takes advantage of the temporal complexity of the signal, and therefore offers an additional gain over narrowband processing by augmenting the dimension of the data space. However, the sensitivity to mismatch is also increased in the process, since a single constraint is usually not enough to achieve robustness and the snapshot requirement becomes even more problematic. The white noise constraint method, typically used for narrowband processing, is applied to a previously derived broadband processor to enhance its robustness to environmental mismatch and snapshot deficiency. The broadband white noise constraint theory is presented and validated through simulation and experimental data. The dynamic range bias obtained from the snapshot-deficient processing is shown to be consistent with that previously presented in the literature for a single frequency.

3.2 Introduction

Adaptive matched-field processing (MFP) is extremely sensitive to environmental mismatch [1, 2]. For example, the minimum variance distortionless response (MVDR) method of using a borehole constrained optimization requires accurate environmental model parameters and array elements localization. The procedure also involves a matrix inversion of a well conditioned sample cross spectral density matrix (CSDM). Single constraints, leading to high resolution processors, become problematic for a combination of large arrays with some mismatch[3]. Robust processors attempt to overcome the mismatch problem while keeping the benefits of the adaptive algorithms[4, 5, 6, 7]. The white noise constraint method (WNCM)[7] has been localizing sources in many challenging environments without the requirement of seeking more accurate environmental information. Further, it has been

effective in dealing with so-called "snapshot-deficient scenarios" in which targets and interferors move across resolution cells before enough data vectors, or snapshots, can be recorded at the array and combined to construct a full rank CSDM [8, 9].

Adaptivity also requires a threshold signal-to-noise ratio (SNR) [10]. Therefore, coherent broadband MFP, which involves an extra-processing gain from using multiple frequency data analogous to the coherent gain associated with more array elements, potentially offers additional opportunities over single frequency processing. However, we can expect adaptive coherent broadband MFP to have even greater mismatch sensitivity since there is a larger data space (frequency $\times$ number of array elements) subject to the same single constraint. In addition, the snapshot requirement[8] for constructing the larger CSDM, which is typically already strained for practical single frequency scenarios, becomes problematic. In this paper, we apply the white noise constraint method to a coherent broadband processor to develop a robust[7] coherent broadband MFP processor suitable for snapshot deficient scenarios.

Broadband matched-field methods can be exploited in either the frequency or time domain. In the time domain, for example, Clay[11] proposed to match measured and modeled impulse responses of transmission between the source and a receiver. This technique, which requires knowledge of the source function, was used by Li *et al* on laboratory data [12, 13] . Brienzo and Hodgkiss[14] also successfully applied it on experimental data coming from an explosive source. The unknown source wave form was estimated from the direct path arrival, and the additional processing gain it procures demonstrated. Frazer and Pecholcs[15] generalized the method and introduced new algorithms requiring no knowledge of the source function, instead estimating it as well as the source location. More recently, Hursky *et al*[16] tracked a high frequency source in range and depth by matching correlations of impulse response function between receivers, canceling out by design the unknown source waveform.

In the frequency domain, a common approach proposed by Baggeroer *et al* is to incoherently average single-frequency ambiguity surfaces to suppress ambigu-

ous sidelobes[10]. Coherent broadband processors, in contrast, take full advantage of the complexity of the signal by keeping the complex cross-frequency inner products. These processors have to deal with the typically unknown complex spectral properties of the source and can be divided into two categories:

1. Matching a first moment quantity such as pressure that consequently involves sample data covariance matrices,

2. Matching a second moment quantity such as data correlations between receiver element pairs and therefore involves estimating fourth moment quantities from data (with an increased data requirement from [frequency $\times$ number of array elements] to [frequency $\times$ (number of array elements)^2] for accurate estimation).

Actually, the latter category was first treated in the literature by Westwood, who developed an algorithm which sums correlations of modeled and experimental cross-spectra coherently over frequency [17]. No knowledge of the source spectrum is assumed, but it can be easily incorporated in the algorithm when known. The method was applied successfully to a shallow water experimental data set characterized by strong multipaths [18]. This method was further generalized by Czenszak and Krolik [19], who introduced an algorithmic procedure involving the fourth-order statistics of the data so that the cross-spectral density matrix of the received data is matched to a set of weight matrices using the magnitude squared Frobenius matrix inner product. Their purpose was to combine the higher moment analysis with its large data and computational requirements with the earlier developed environmental perturbation constraint method[5]. The latter's additional constraints resulted in a more stable, though extremely lengthy processing procedure.

The first category builds on standard algorithms already well-known from frequency domain processing. Michalopoulou and Porter[20, 21] proposed a processor in which the data is stacked over frequencies in a "supervector" and matched to a modeled one. While the tranfer functions are treated coherently, one should note that this processor is really only semi-coherent, since the unknown phases

across frequency are removed in the construction of the supervector. The processing allows for including the source amplitude, if known. Orris *et al* further considered those unknown phase relationships as free parameters that may be determined using a global functional minimization algorithm, again with increased computational complexity [22].

In parallel, an extensive amount of work has been done to address the conflicting issues of resolution and robustness to environmental mismatch. High resolution was achieved by developing optimal processors resulting from the solution of a constrained optimization problem. These adaptive algorithms, such as the the MVDR processor [23], use the data to construct optimum weights. While very efficient at suppressing noise and interfering signals, the MVDR is more vulnerable to any kind of mismatch between the modeled and real pressure fields than a conventional processor [7]. Furthermore, it requires a sufficient number of snapshots to construct an invertible CSDM. This is often problematic for a moving target because of the opposing requirements of high resolution producing small resolution cells versus the necessity of building up a CSDM from sufficient snapshots in a single cell.

Again there are two categories of dealing with environmental robustness:

1. Enlarge the search space or provide some sort of environmental blurring[4, 5, 6, 24],

2. Constrain the algorithmic cause of the instability[3, 7].

The WNCM [7], which constrains the array gain against uncorrelated noise, performs particularly well in dealing with both robustness and snapshot-deficient data. For the latter aspect, the dynamic range bias of snapshot-deficient processing has been addressed in the literature[8, 9] and must also be considered in the broadband case.

This paper combines the coherent broadband method introduced by Porter and Michalopoulou (herein referred to as MP) with white noise constrained MVDR processing. In Sec. 3.3, we first provide an overview of incoherent and coherent MP processors . We then apply the MVDR/WNC method in section 3.4.

We also illustrate the resulting performance using data from the Hudson Canyon experiment[25]. In section 3.5, we show that the dynamic range bias from the snapshot deficient processing is consistent with previous single frequency literature[8, 9] and that the processor has a SNR threshold. We evaluate the robustness of the processor to slight environmental mismatch as the source moves in range in section 3.6. Finally, section 3.7 provides a summary and discussion.

3.3 Formulation of the coherent MP model

Amongst the diverse coherent broadband algorithms introduced in the literature, the coherent MP model has been chosen in this study because it is readily applicable to adaptive MFP, and the results obtained using the MVDR processor on real data are promising[20] .

Let $x_\omega^{(i)}$ denote the complex field received on the hydrophone i, N the number of hydrophones in the array, and L the number of individual frequencies considered. The multiple frequency components are incorporated by stacking narrowband signal vectors into one "supervector" of length $N \times L$, L being the number of tones processed and the superscrpt T the transpose operation,

$$\breve{\boldsymbol{x}} = \left[\; x_1^{(1)}, x_1^{(2)}, \ldots, x_1^{(N)}, \ldots, x_L^{(1)}, \ldots, x_L^{(N)} \; \right]^T. \tag{3.1}$$

From this supervector, a "super" CSDM can be constructed by forming the outer product of the vector by its complex conjugate transpose, $\breve{\boldsymbol{R}} = E\{\breve{\boldsymbol{x}}\breve{\boldsymbol{x}}^H\}$, where $E\{\}$ is the expectyation value. The MFP processor output can then be formulated as

$$P_{MP}(r,z) = \breve{\boldsymbol{d}}^H(r,z)\breve{\boldsymbol{R}}\breve{\boldsymbol{d}}(r,z),$$

$$P_{MP}(r,z) = E\left[\left| \sum_{k=1}^{L} \boldsymbol{d_k}^H(r,z)\boldsymbol{x_k} \right|^2 \right], \tag{3.2}$$

where $d_k(r,z)$ is the replica vector at angular frequency ω_k from a source at depth z and distance r from the array and the superscript H is the complex conjugate transpose operation.

Note that the position of the absolute value delimiters outside of the sum over frequencies allows the transfer functions to be treated coherently and generates cross-frequency terms. In contrast, an incoherent algorithm sums absolute values of inner products

$$P_{IC\_linear}\left(r,z\right) = E\left[\sum_{k=1}^{L}\left|\boldsymbol{d}_k^H(r,z)\boldsymbol{x}_k\right|^2\right]. \tag{3.3}$$

The complex signal received on the element i can be written as

$$x_\omega^{(i)} = S(\omega)G^{(i)}(0,z_i,R_s,Z_s,\omega), \tag{3.4}$$

where $S(\omega)$ is the complex source signal at the angular frequency ω, and the expression $G^{(i)}(0,z_i,R_s,Z_s,\omega)$ the transfer function between the source and the receiver i, assuming the ideal case of no contamination by noise. Rewriting the output of the algorithm reveals that the unknown source phase terms remain to be evaluated, leaving the user with replicas mismatched with respect to the signal,

$$\begin{aligned} P_{MP}\left(r,z\right) &= \sum_{l=1}^{L}\sum_{k=1}^{L}\boldsymbol{d}_l^H(r,z)\boldsymbol{x}_l\boldsymbol{x}_k^H\boldsymbol{d}_k(r,z) \\ &= \sum_{l=1}^{L}\sum_{k=1}^{L}S(l)S(k)^*\boldsymbol{d}_l^H(r,z)\boldsymbol{G}_l\boldsymbol{G}_k^H\boldsymbol{d}_k(r,z). \end{aligned} \tag{3.5}$$

where the asterisk represents the complex conjugate operation.

The MP method addresses this issue by scaling the phase of each single-frequency subvector $\boldsymbol{x}_\omega$ by the phase on the first phone, and normalizing the subvector to unit length [20, 21]. This compensation procedure eliminates the unknown source terms in high signal-to-noise scenarios since, if we denote the new subvector by $\overline{\boldsymbol{x}}_\omega$,

$$\boldsymbol{x}_\omega = \begin{bmatrix} \left|S(\omega)G_\omega^{(1)}\right| e^{j\left(arg(S(\omega))+arg(G_\omega^{(1)})\right)} \\ \vdots \\ \left|S(\omega)G_\omega^{(N)}\right| e^{j\left(arg(S(\omega))+arg(G_\omega^{(N)})\right)} \end{bmatrix},$$

we have,

$$\overline{\boldsymbol{x}}_\omega = \frac{1}{\alpha}\begin{bmatrix} \left|G_\omega^{(1)}\right| e^{j0} \\ \vdots \\ \left|G_\omega^{(N)}\right| e^{j\left(arg(G_\omega^{(N)})-arg(G_\omega^{(1)})\right)} \end{bmatrix}, \tag{3.6}$$

where $\alpha = \sqrt{\left|G_\omega^{(1)}\right|^2 + \ldots + \left|G_\omega^{(N)}\right|^2}$ is a coefficient of normalization.

When the amount of noise imbeded in the signal is not negligible anymore, the above-described amplitude and phase normalization scheme does not cancel the unknown source terms in the noise component. The MP algorithm therefore carries an inherent mismatch when localizing low signal-to-noise ratio sources. See section 3.4 for further discussion of the MP algorithm's performance versus signal-to-noise ratio.

3.4 Minimum variance and white noise constraint processing

In this section, the minimum variance and white noise constraint methods are presented in the context of broadband MFP. Their localization performance, both in the incoherent and coherent case, is evaluated on experimental data. The Hudson Canyon experiment[25] , used by Michalopoulou and Porter to test their algorithms as well[20], was chosen for comparison purposes. It took place in shallow water (73 m) out of the New Jersey coast. An acoustic source was towed at 36 m deep over an essentially flat bottom, and the acoustic field was sampled by a 24 element vertical line array.

Data from two source tracks (ten different ranges per track) are provided. In the first one, the source sent multi-tones at 50, 175, 375 and 425 Hz and moved up to 4.5 km away from the receivers. The source traveled back toward the receiver array in the second track, emitting tones at 75, 275, 525 and 600 Hz. Ten observations are available for each source range, and the average SNR at each element was approximately 10 dB. The Hudson Canyon environment is illustrated in Fig. (3.1). A normal mode propagation model [26] is used to create the replica vectors, and 4, 15, 32, and 36 modes were kept, respectively, at the frequencies of the first leg, and 6, 24, 30, and 46 modes at the ones of the second leg.

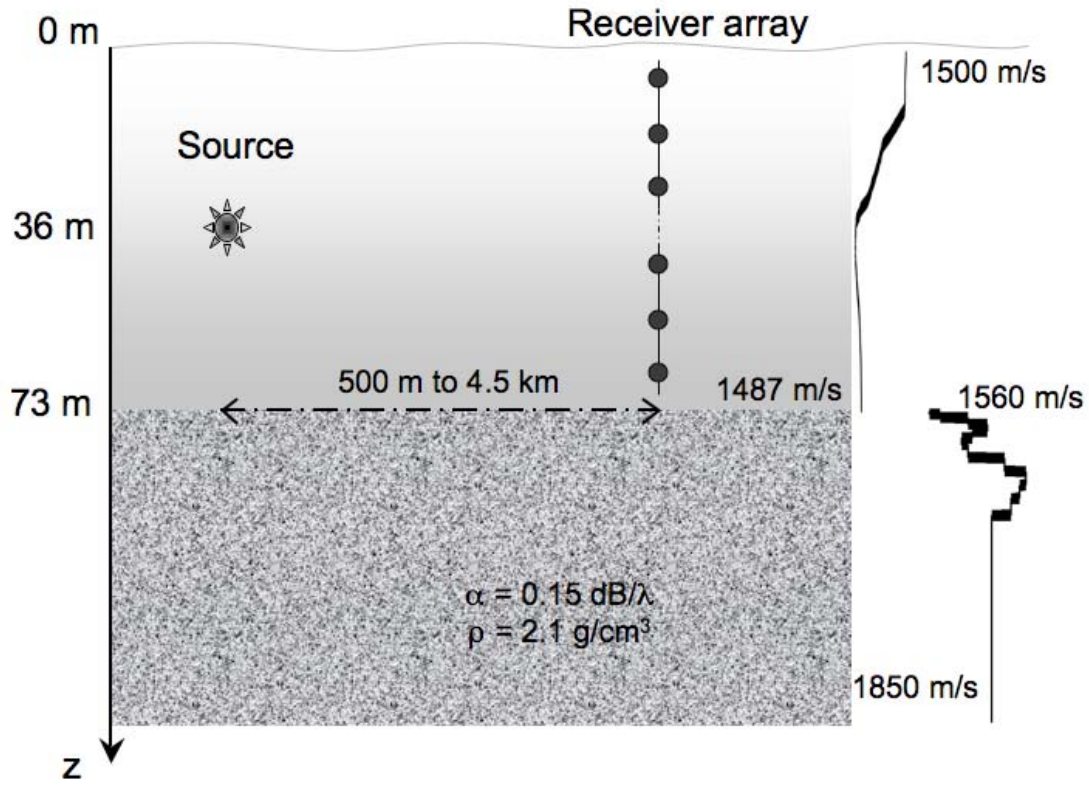

Figure 3.1: The Hudson Canyon environment features a 24 element vertical array and an acoustic source towed at 36 m deep from 500 m to 4.5 km away from the receivers and sent a set of four tones at 50, 175, 375, and 425 Hz. It traveled back toward the receiver array in a second track, emitting tones at 75, 275, 525, and 600 Hz.

3.4.1 Minimum variance method

The general formulation of the MVDR matched-field processor in the frequency domain starts with

$$P\,(r,z) = \boldsymbol{w}^H(r,z)\boldsymbol{R}\boldsymbol{w}(r,z). \tag{3.7}$$

where $\boldsymbol{R} = E\{\boldsymbol{x}\boldsymbol{x}^H\}$ is the CSDM at the frequency of interest, and the weight vector $\boldsymbol{w}$ is determined by solving

$$\min_{\boldsymbol{w}} \boldsymbol{w}^H\boldsymbol{R}\boldsymbol{w} \quad \textit{subject to } \boldsymbol{w}^H\boldsymbol{d} = 1, \tag{3.8}$$

$\boldsymbol{d}$ being the look direction steering vector at (r,z).

The well known solution of this optimization problem is

$$\boldsymbol{w}_{\boldsymbol{mvdr}} = \frac{\boldsymbol{R}^{-1}\boldsymbol{d}}{\boldsymbol{d}^H\boldsymbol{R}^{-1}\boldsymbol{d}}, \tag{3.9}$$

which yields:

$$\boldsymbol{P}_{\boldsymbol{mvdr}}\,(r,z) = \frac{1}{\boldsymbol{d}^H\boldsymbol{R}^{-1}\boldsymbol{d}}. \tag{3.10}$$

This algorithm enhances the resolution considerably in comparison to a conventional processor, however, this exceptional resolution capability comes with an increased sensitivity to slight mismatch between the modeled and actual environment.

Michalopoulou and Porter tested the MVDR algorithm on the Hudson canyon experimental data set [20]. Since only ten snapshots were available per source position, the cross-spectral density matrix was diagonally loaded "by adding a small multiple of the identity matrix to it" [20]. Their study shows that incoherently averaging MVDR ambiguity surfaces yields marginal results for that data set. As expected, the narrowband MVDR is quite sensitive to mismatch, and averaging single-frequency outputs reinforces the maximum constructively in only 10 % of the cases (30 % when each output was normalized to a maximum of one prior averaging).

In contrast, the broadband coherent MP version of the MVDR shows a great improvement, now successfully localizing the source in 90 % of the cases, though with a peak-to-sidelobe ratio of only 2 dB or less.

Those encouraging results show that frequency coherence does enhance marginaly the estimation performance, and motivate us to apply an additional constraint on the white noise gain (WNCM processor) in an attempt to increase the robustness to mismatch.

3.4.2 White noise constraint method

Cox *et al* [7] showed that in the presence of uncorrelated noise, the sensitivity of the algorithm to signal mismatch is equal to the reciprocal of the white noise gain. This observation led them to introduce an inequality constraint on the gain against spatially white noise. This modified MVDR, the WNCM algorithm, consequently loses some of its high-resolution characteristics along with its requirement for very precise knowledge of the environment.

In the frequency domain, the weight vector is the solution of the optimization problem:

$$\min_{\boldsymbol{w}} \boldsymbol{w}^H \boldsymbol{R} \boldsymbol{w} \;\; subject\,to \;\; \boldsymbol{w}^H \boldsymbol{d} = 1 \;\; and \;\; \boldsymbol{w}^H \boldsymbol{w} \leq \delta^{-2}, \tag{3.11}$$

where δ^2 ia a number less than the maximum possible white noise gain given by $max[1/w^H w)] = 1$. It yields:

$$\boldsymbol{w}_{\boldsymbol{wncm}}(r,z) = \frac{(\boldsymbol{R} + \epsilon \boldsymbol{I})^{-1} \boldsymbol{d}}{\boldsymbol{d}^H (\boldsymbol{R} + \epsilon \boldsymbol{I})^{-1} \boldsymbol{d}}. \tag{3.12}$$

The value of ϵ is such that the third inequality of Eq. 3.11 is satisfied.

When the environment is well studied, single frequency WNCM usually succeeds in localizing the source. An incoherent average across frequencies is then expected to further reduce the sidelobes level, provided that the type of mismatch present doesn't provoke a frequency-dependent shift of the maximum.

In an attempt to decrease the level of the sidelobes, a coherent-broadband white noise constraint processor is implemented. Since the MP algorithm is formulated in the usual quadratic form, $P_{MP}(r,z) = \overline{\boldsymbol{w}}^H(r,z)\overline{\boldsymbol{R}}\overline{\boldsymbol{w}}(r,z)$, and as in the narrowband case the white noise cross-spectral density matrix is the identity matrix, the extension to the white noise constraint algorithm is straightforward:

$$\boldsymbol{w}_{wncm}^{MP} = \frac{\left(\overline{\boldsymbol{R}} + \epsilon \boldsymbol{I}\right)^{-1} \overline{\boldsymbol{d}}}{\overline{\boldsymbol{d}}^H \left(\overline{\boldsymbol{R}} + \epsilon \boldsymbol{I}\right)^{-1} \overline{\boldsymbol{d}}}. \tag{3.13}$$

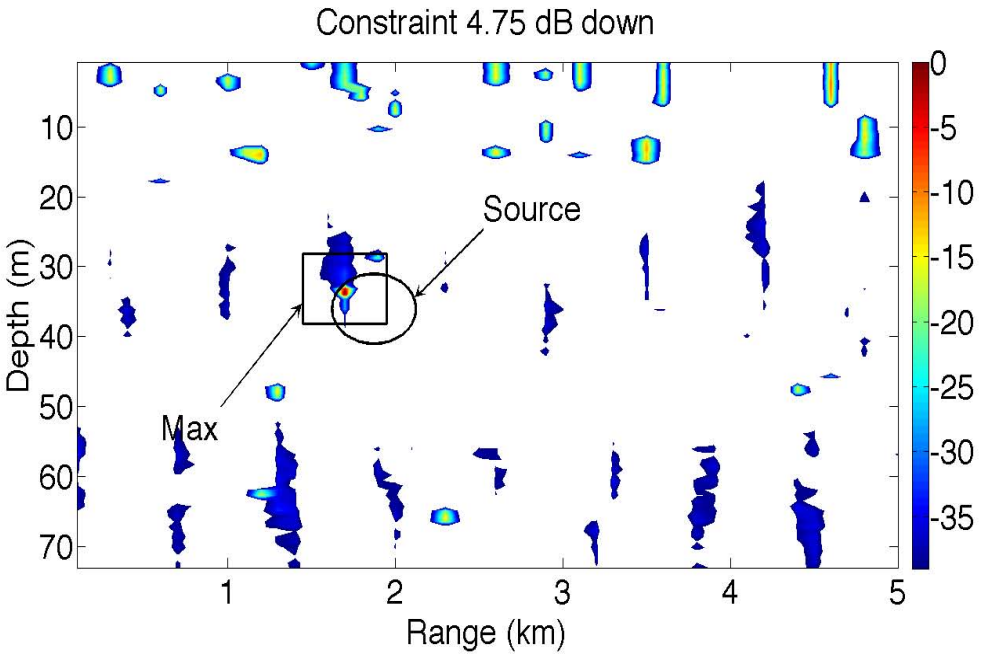

Figure 3.2: White noise constraint MFP obtained by an incoherent dB average of four frequencies ambiguity surfaces (50, 175, 375 and 425 Hz). The source is localized and the first sidelobes appear 10 dB down from the main peak. The white color corresponds to a level beyond the dynamic range.

This time the amount of loading is determined by the supervector.

The same portion of the Hudson canyon data set used by Michalopoulou and Porter to test the MVDR version of their coherent algorithm is processed for comparison purposes. The value of the constraint on white noise being somewhat arbitrary, a set of constraints ranging from 0.5 to 6 dB down the maximum by steps of 0.25 dB will be applied. As discussed in section 3.5, the constraint allowing the maximum dynamic range bias to be visible will be kept. Note that the value of the constraint does not vary across frequency. The source is considered correctly localized when the the maximum is within 5 m depth and 200 m range from the true position.

Figure (3.2) shows the output of the incoherent average of WNCM ambiguity surfaces obtained with the constraint showing a maximum bias. The source location, at $Z_s = 36\ m$ and $R_s = 1.87\ km$ is marked by an ellipse, while the

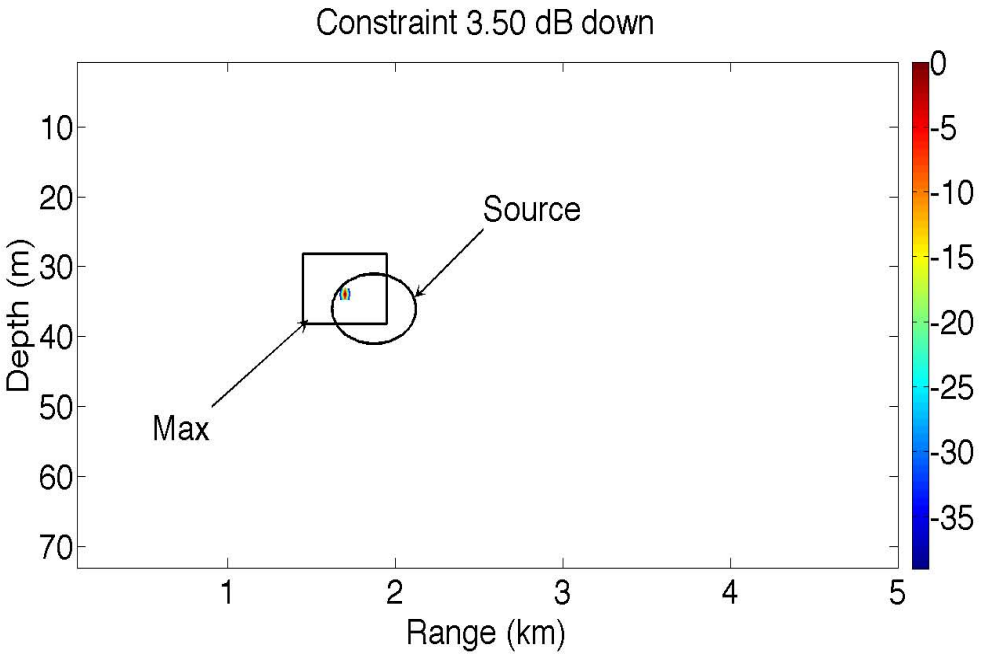

Figure 3.3: Output from the MP coherent broadband white noise constraint MFP using four frequencies (50, 175, 375 and 425 Hz) . The main peak is at the true source position, and stands 146 dB above the noise. The white color corresponds to a level beyond the dynamic range. The dynamic range is set to 40 dB for comparison purposes with Fig. (3.6).

maximum of the ambiguity surface lies in the square. In contrast with the incoherent average of MVDR single-frequency outputs, the source is now localized successfully, with a peak-to-sidelobe level of approximately 10 dB.

Figures (3.3) and (3.4) display the MP coherent-broadband, white noise constraint, ambiguity surface (with the constraint showing a maximum bias) with 40 and 150 dB dynamic range, respectively. As apparent in Figs. (3.3) and (3.4), the algorithm is not only robust to mismatch between the experimental and modeled fields since the source is successfully localized, but also discriminating, as suggested by the absence of any sidelobes up to 40 dB under the peak value. In fact a large dynamic range of 146 dB was necessary to see the first sidelobes. Since the actual SNR at each element was around 10 dB and there were only 24 elements and 4 frequencies processed, it suggests the presence of a bias in dynamic range,

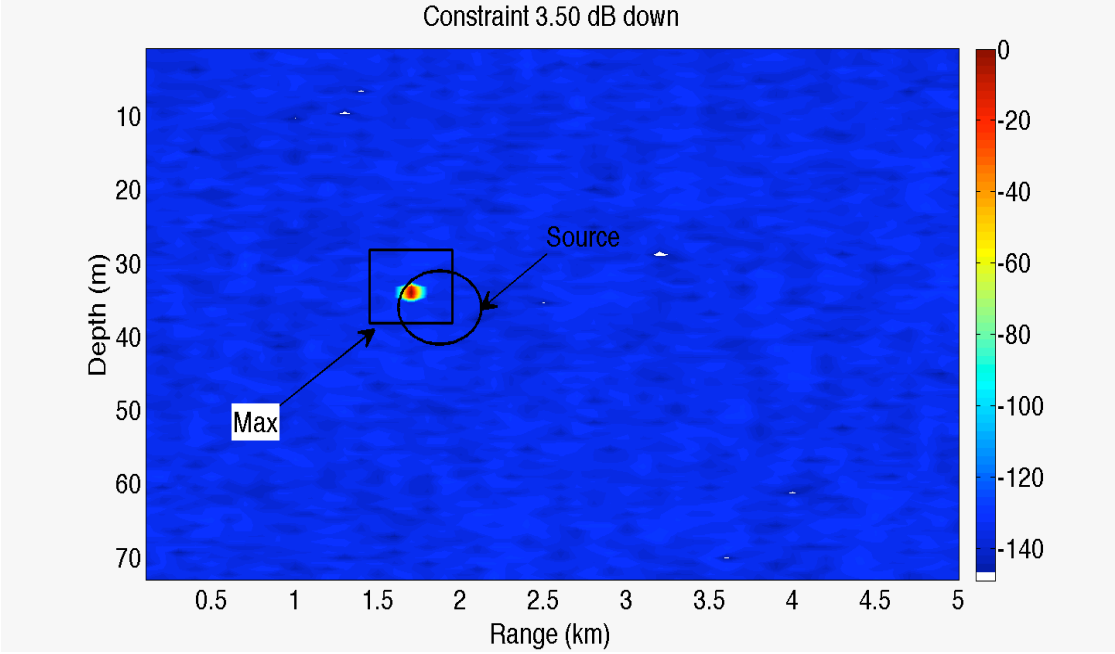

Figure 3.4: Output from the MP coherent broadband white noise constraint MFP using four frequencies (50, 175, 375 and 425 Hz) . The main peak is at the true source position, and stands 146 dB above the noise. The white color corresponds to a level beyond the dynamic range. The dynamic range is set to 150 dB to see the sidelobe level.

discussed for a single frequency by Baggeroer and Cox[8] as well as Song *et al* [9] and generalized for multiple frequencies in the Sec. 3.5.

3.5 Dynamic range bias in white noise processing

In a snapshot-deficient scenario, as in the Hudson canyon data set, the CSDM eigenvalue spectrum is composed mainly of three groups. The highest eigenvalues correspond to the source and strong interferers, followed by a lower plateau of eigenvalues associated with noise, and finally non-physical eigenvalues, usually much lower in magnitude, due to the fact that the matrix is ill-conditioned. In this case, diagonally loading the CSDM decreases the gap between the noise eigenvalues and the lowest plateau, and eventually renders the matrix invertible. But by changing the magnitude of these small eigenvalues, we also change the amount of bias at the output of the loaded MVDR, such that the apparent power of the signal and noise will be lower than in reality[8].

Song *et al* formulated the amount of bias to be expected versus loading γ [9]. Note that the loading referred to here as γ is a static loading independent of the look direction, as would be used to invert the CSDM for the MVDR algorithm, as opposed to the dynamic loading ϵ involved in the WNCM processor. They found that when γ was much smaller than the eigenvalues of the CSDM associated with noise smallest noise, λ_n, the signal and noise power outputs shifted by $2\gamma/\lambda_n$ in decibels. However, when γ is equal or bigger to that smallest eigenvalue, the power output changes as only γ/λ_n in decibels. In both cases, the shift in magnitude of the power output is responsible for the bias in dynamic range observed on the MP coherent-broadband, white noise constraint, ambiguity surfaces, as explained in the following.

Figure (3.5) gives a schematic representation of the variation of the eigenvalue spectrum in our example as the CSDM becomes snapshot deficient. In the Hudson Canyon experiment, the SNR recorded at each element was approximately 10 dB. When introducing an additional 20 dB of array gain ($10log(L \times N)$), the gap between the signal and noise eigenvalues is expected to be around 30 dB. There-

diagram.pdf

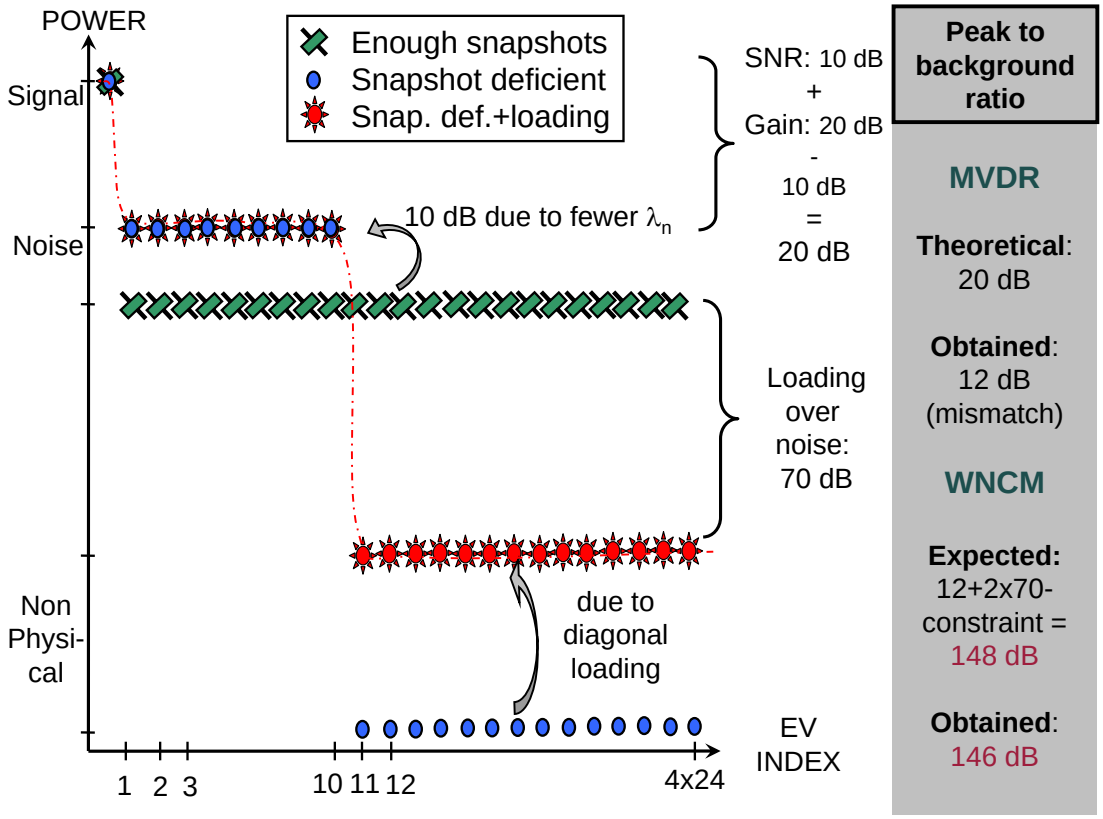

Figure 3.5: Variation of the coherent CSDM signal and noise eigenvalues in the ideal case of (1) sufficient snapshots, (2) 10 snapshots only and (3) 10 snapshots and a loading of γ/λ_n = -70 dB. The corresponding expected and obtained peak-to-background ratios is given for the broadband coherent MVDR and WNCM algorithms.

fore, with no diagonal loading, and in the ideal case of no environmental mismatch or snapshot deficiency, the peak-to-background ratio at the output of the MVDR should be 30 dB.

Since there is not enough snapshots available in our case, a small amount of loading is chosen in order to invert the cross-spectral density matrix. More precisely, $\gamma/\lambda_n = 10^{-7}$ (or -70 dB) was found sufficient to stabilize the matrix with respect to inversion. This corresponds to the first case of the bias theory for which γ is much smaller than the eigenvalues of the CSDM associated with

noise; therefore we can expect the signal and noise power outputs to be shifted by $2 * [\gamma/\lambda_n]_{in\ dB} = 2 * (-90 + 20) = -140$ dB. However, since the ambiguity surfaces are normalized to have a maximum of 0 dB prior to plotting, and both the signal and noise are biased in the same way, this 140 dB bias is not visible in the MVDR plots, as seen in the pictures obtained by Michalopoulou and Porter[20]. One can also notice that a peak-to-background ratio of about 12 dB was obtained instead of the theoretical 30 dB. Indeed, the total noise level, expressed as the sum of the noise eigenvalues, remains the same between the ideal and snapshot-deficient scenarios, while the number of noise eigenvalues decreases from $L \times N$ to 10. We therefore expect the snapshot-defficient noise eigenvalues to be $10log[(L \times N)/10] = 9.8$ dB more powerful than the ideal noise eigenvalues. The inevitable environmental mismatch is responsible for the remaining discrepancy between the theoretical and experimental coherent MVDR peak-to-background ratios.

As Song also pointed out, the white noise constraint method, in contrast to the MVDR, takes advantage of this power bias [9]. Indeed the WNCM sets the white noise gain to that of the MVDR until the norm of the MVDR until the norm of the MVDR weight vector no longer satisfy the inequality constraint. When this happens, the CSDM is loaded causing the white noise gain to decrease and eventually reach a minimum value determined by the constraint δ itself.

Therefore, in our white noise constraint plots, the noise should be 140 dB lower than its actual physical value everywhere except around the location of the source for which the MVDR weight vector's norm becomes very large. The white noise gain at the peak is then set by the value of the constraint (-3.5 dB for the coherent case in Figs. (3.3) and (3.4). In other words, the peak to background ratio is expected to be given by [bias + peak-to-background ratio without loading - white noise constraint] $= -140 - 12 + 3.5 \approx -148$ dB, which is consistent with the 146 dB dynamic range found experimentally.

To test the hypothesis that the bias present in our results is indeed dependent on the amount of loading, we increased the loading by steps of 2 dB in Fig. (3.6) and looked at the evolution of the peak-to-background ratio in decibels. The dot lines correspond to the case previously depicted of $\gamma/\lambda_n = -70$ dB. For

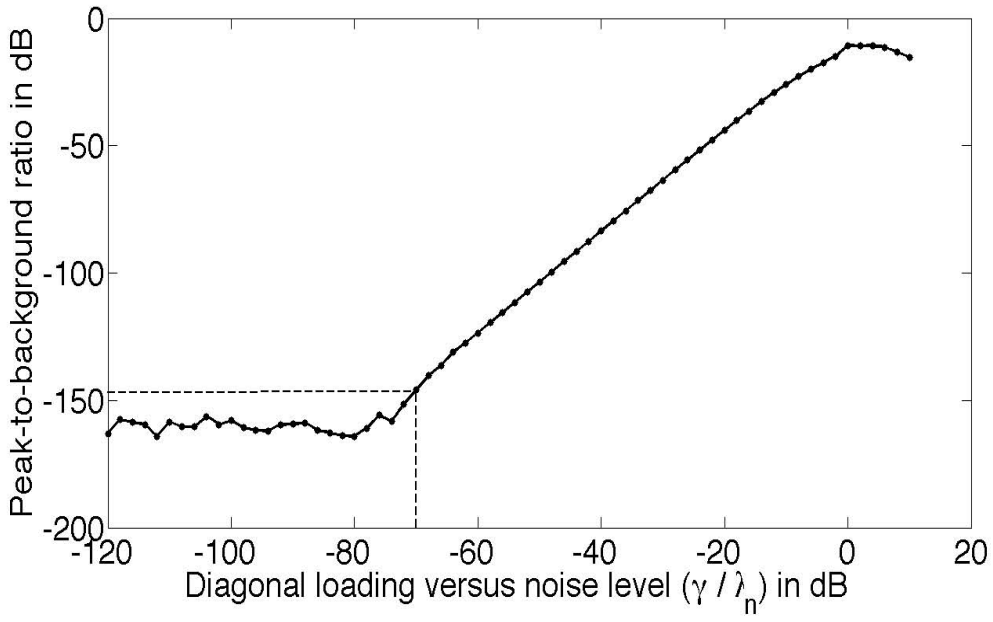

Figure 3.6: Effect of the amount of diagonal loading on the bias for broadband coherent white noise processing in a snapshot deficient scenario. As the theory suggests, the peak-to-background ratio is varying with respect to the loading with a slope of 2. The dashed lines correspond to the example previously treated.

$\gamma/\lambda_n \in [-75, -10]$ dB, the peak-to-background ratio is reduced by the diagonal loading with a slope of 2, as is found theoretically. As the loading continues to increase, the slope of the peak-to-background ratio approaches one, and eventually reaches the -12 dB ratio of the MVDR processing. When the loading gets very small in comparison to the noise eigenvalues, $\gamma/\lambda_n = -75$ dB, the matrix is increasingly ill-conditionned and the effect of loading becomes negligible. Hence the peak-to-background ratio reaches the machine precision limit of -160 dB.

As seen on Fig. (3.4), the MP broadband coherent white noise constraint processor localizes the source successfully while reducing the sidelobe level to -146 dB. However such a dynamic range does not imply that it can localize sources at extremely low signal-to-noise ratio. There is in fact a threshold SNR, discussed by Baggeroer *et al* in the single frequency context, under which the algorithm fails to localize the source [10]. We illustrate the issue by implementing a mismatch-free

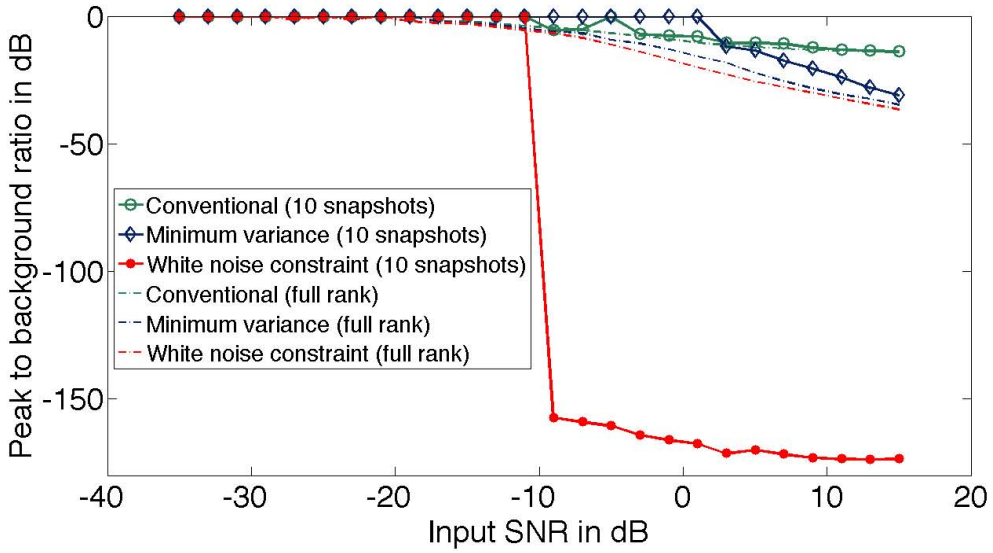

Figure 3.7: Effect of the signal-to-noise ratio on the detectability of the source using the coherent broadband MP algorithm in a snapshot deficient scenario. A peak-to-background level of 0 dB corresponds to a failure of the algorithm to localize the source. For the WNCM algorithms, a set of constraints ranging from 0.5 to 6 dB down the maximum by steps of 0.25 dB is applied, and the largest peak-to-background ratio obtained for each input SNR is represented. Despite the large dynamic range provided by the white-noise constraint, it cannot localize sources at really low SNR.

simulation of the Hudson Canyon environment in a snapshot-deficient scenario for which the SNR at each receiver was reduced by steps of 2 dB. This was done by constructing ten individual realizations of signal plus white noise, and implementing the CSDM associated.

Figure (3.7) represents the peak-to-background ratio obtained with the conventional, minimum variance, and white-noise constraint MP coherent broadband processor as the input SNR varies. A peak-to-background ratio of 0 dB corresponds to cases for which the algorithm failed to localize the source. One can note that despite having a 20 dB theoretical array plus processing gain, the coherent white noise constraint algorithm in a snapshot-deficient scenario does not localize a source with less than -10 dB SNR. This is due to the smaller number of eigenvalues

associated with noise, discussed previously, effectively lowers the gain to 10 dB. In contrast, the curves obtained with a full rank CSDM matrix show no bias and localize sources as weak as -20 dB SNR. While the coherent white-noise constraint method displays very low sidelobes and a better performance than the other algorithms at low SNR, it nevertheless fails at SNR lower than -10 dB despite its very large dynamic range.

The excess of dynamic range associated with the broadband WNC processor is therefore convenient for localization purposes but caution is required when making any physical interpretation.

3.6 Source tracking in range and depth

In the specific example discussed in Sec. 3.4, both MVDR and WNCM versions of the broadband coherent algorithm developed by Michalopoulou and Porter localized the source, but the white noise constraint displayed much lower sidelobes. How robust is this algorithm when the environmental mismatch is increased and the position of the source changed? To address this question, we processed each of the twenty frames present in the outgoing and incoming legs, and introduce a slight sound speed mismatch. The localization performance in range and depth of the coherent and incoherent MVDR and WNCM matched-field processors was then compared.

Figure (3.8) (a) displays the range slices obtained with the incoherent minimum variance processor for each source position, and Fig. (3.8) (b) shows the depth track intersecting those estimated ranges. The known source ranges and depths are indicated by the black circles. Figures (3.9) (a) and (3.9) (b) are the corresponding figures obtained using the coherent MP MVDR algorithm. In this case, the mismatch is sufficient to lose track of the source at most positions for both incoherent and coherent processors. The sidelobe level is, however, lower in the coherent case.

Figures (3.10) (a), (3.10) (b) and Figs. (3.11) (a), (3.11) (b) show the same type of plots using the incoherent and coherent MP white noise constraint

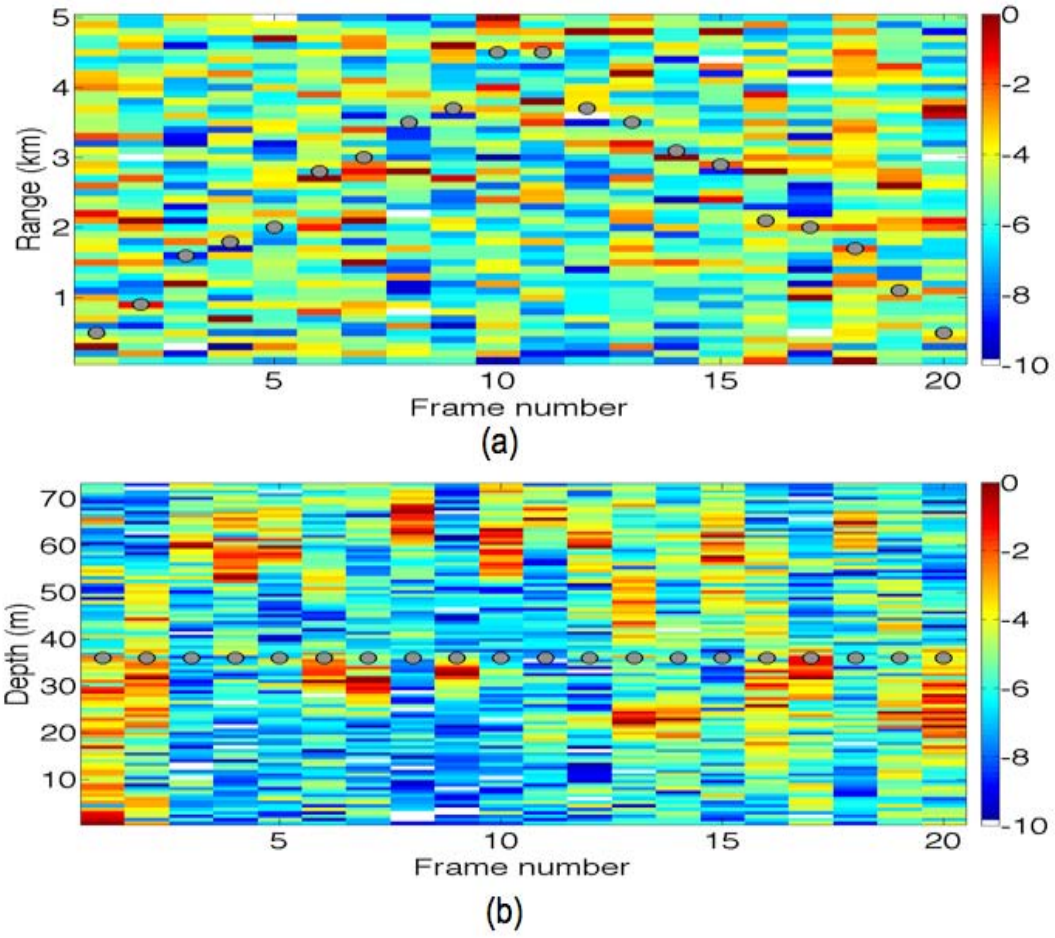

Figure 3.8: Source track obtained using the incoherent minimum variance algorithm in the presence of mismatch. The black circles indicate the true source positions. (a) Range track at source depth of 36 m, and (b) depth track along the estimated range track.

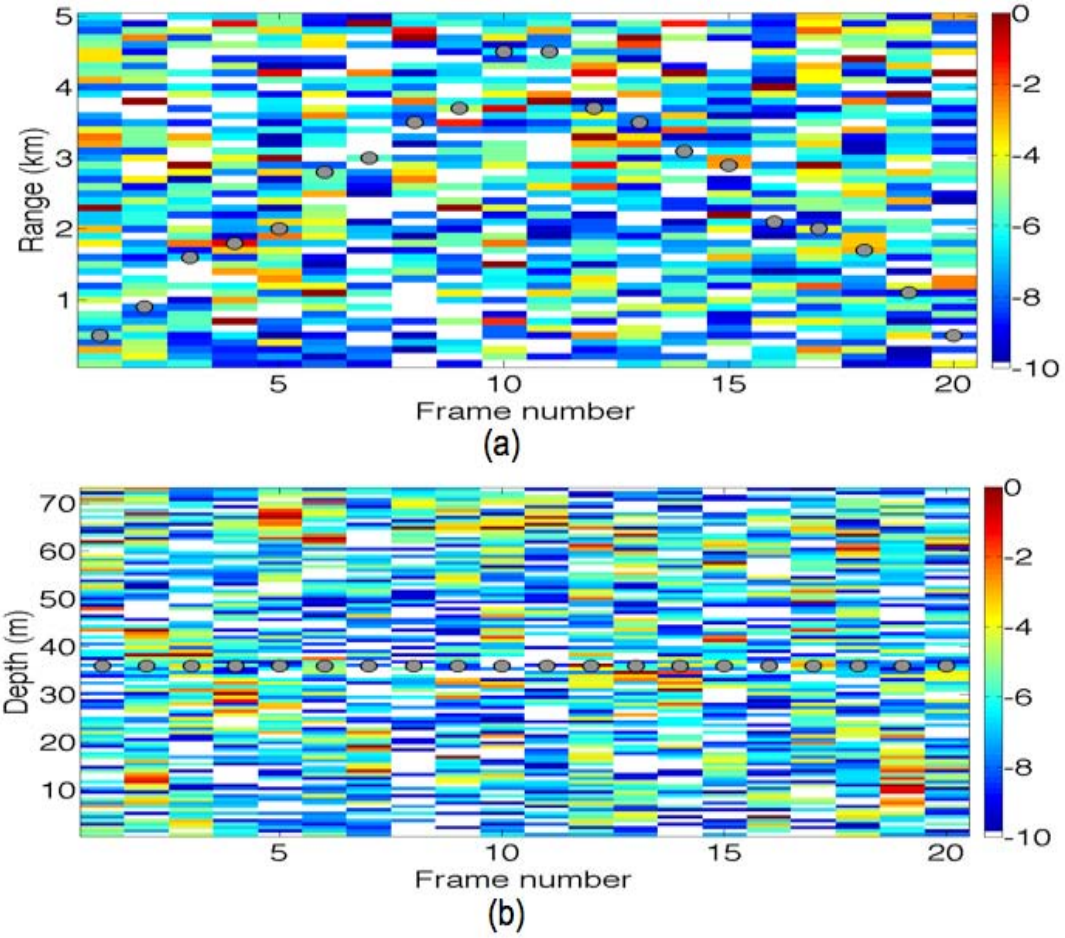

Figure 3.9: Source track obtained using the coherent MP minimum variance algorithm in the presence of mismatch. The black circles indicate the true source positions. (a) Range track at source depth of 36 m, and (b) depth track along the estimated range track.

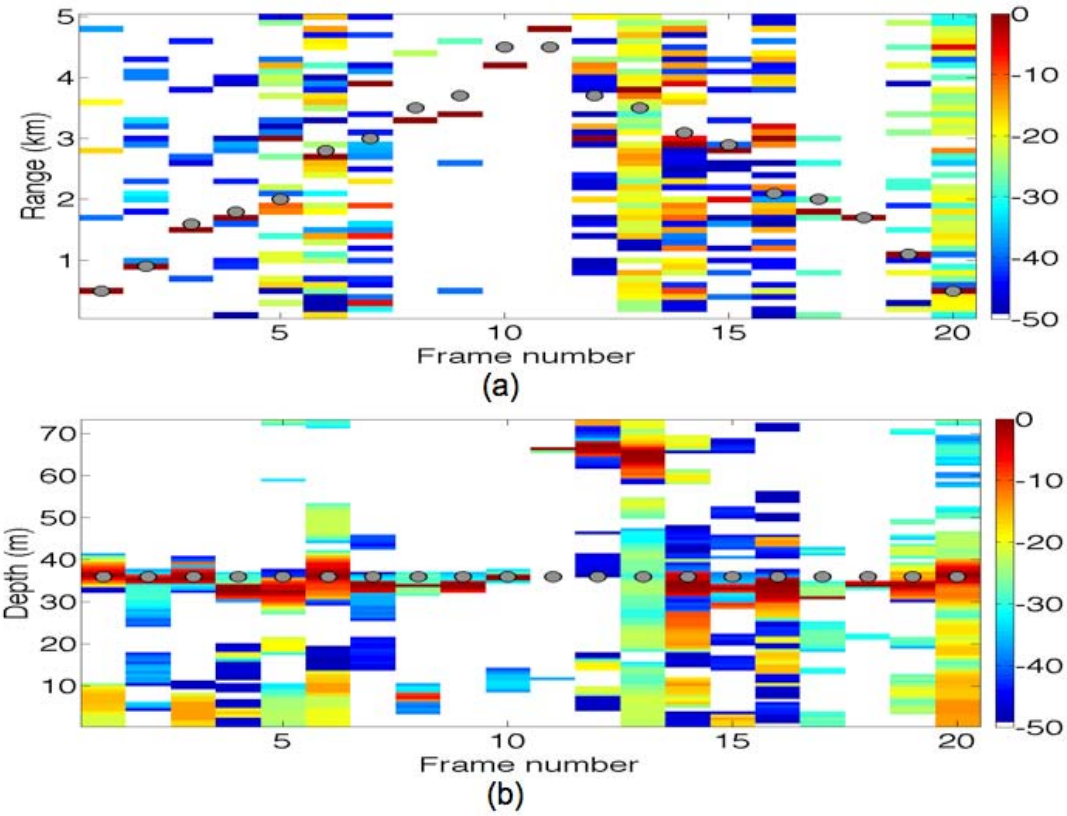

Figure 3.10: Source track obtained using the incoherent white noise constraint algorithm in the presence of mismatch. The black circles indicate the true source positions. (a) Range track at source depth of 36 m, and (b) depth track along the estimated range track.

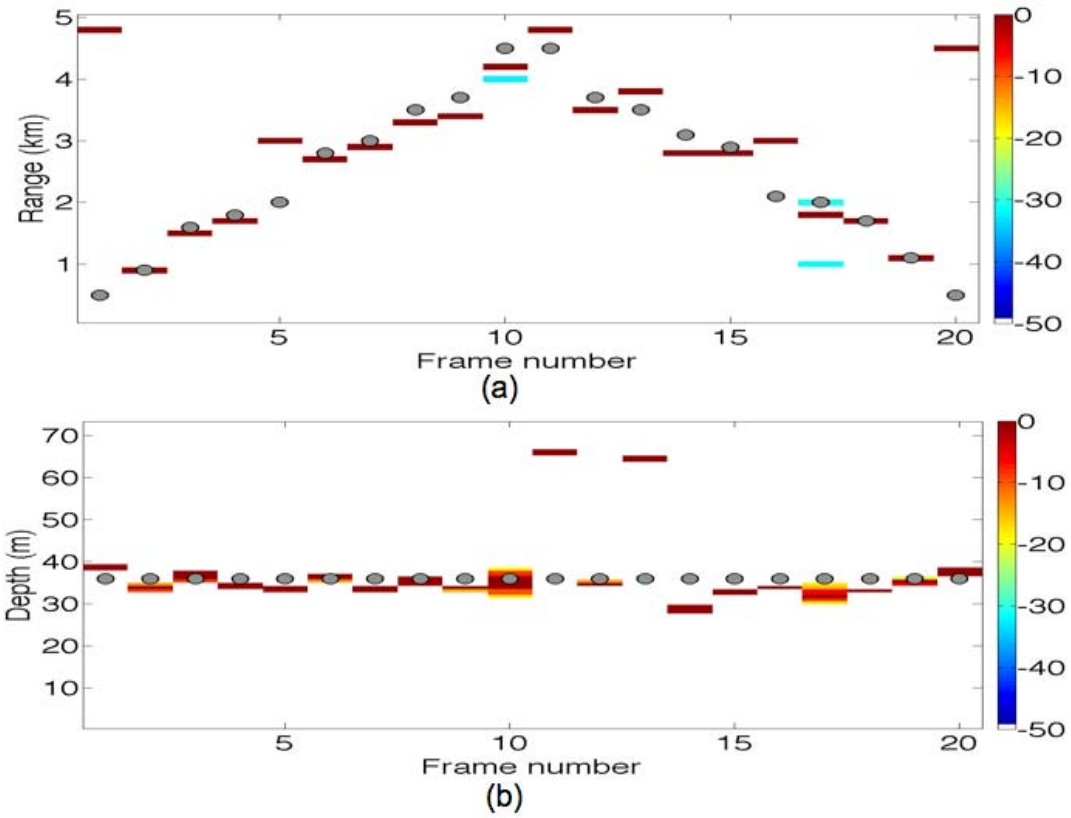

Figure 3.11: Source track obtained using the coherent MP white noise constraint algorithm in the presence of mismatch. The black circles indicate the true source positions. (a) Range track at source depth of 36 m, and (b) depth track along the estimated range track.

algorithms. This time the source is tracked in range and depth in both cases, with a significantly lower sidelobe level obtained when using the coherent MP processor. The white noise constraint algorithm is therefore more robust to environmental mismatch than the MVDR and produces low sidelobes when combined with a coherent broadband algorithm like the one developed by Michalopoulou and Porter.

3.7 Summary and conclusion

The problem of broadband acoustic source localization in shallow water has been addressed. As previously shown, exploiting the information across frequency is essential to perform a successful localization in this type of environment. Two approaches were compared, the first consists in incoherently averaging the information across frequencies, and the second, developed by Michalopoulou and Porter, treats the multiple frequencies information coherently. Applying the very common MVDR estimator to both methods revealed that the MFP discrimination is indeed improved by the use of a coherent algorithm, but, on the other hand, that sensitivity to mismatch is still problematic.

To address this issue, the robust white noise constraint estimator has been applied to the coherent and incoherent approaches. Both methods were able to track a source accurately and continuously using experimental data, in the presence of enough mismatch to lead to erroneous MVDR detections. The coherent white noise constraint processor has also been shown through simulation to perform better than the conventional and MVDR estimators at low SNR. Applying the WNCM algorithm to the MP broadband coherent method allowed us to get a robust, discriminating, high resolution processor well suited for practical applications.

3.8 Acknowledgments

This work was funded by ONR under Contract No. N00014-06-1-0198. The authors would also like to thank Michael Porter for providing the data of

the Hudson Canyon experiment, and Heechun Song for his helpful comments and discussions.

The text of this chapter is a full reprint of the material as it appears in Claire Debever and William A. Kuperman, "Robust matched-field processing using a coherent broadband white noise constraint processor", J. Acoust. Soc. Am., vol. 122, Number 4, pp. 1979-1986. The dissertation author was the primary researcher and author, and the co-author listed in this publication directed and supervised the research which forms the basis for this chapter.

Bibliography

[1] A. B. Baggeroer, W. A. Kuperman, and P. N. Mikhalevsky. An overview of matched field methods in ocean acoustics. *IEEE Journal of Oceanic engineering*, 18(4):401–424, october 1993.

[2] A. Tolstoy. *Matched Field Processing for Underwater Acoustics*. World Scientific, Singapore, 1992.

[3] J. N. Maksym. A robust formulation of an optimum cros-spectral beamformer for line arrays. *J. Acoust. Soc. Am.*, 65(4):971–975, April 1979.

[4] H. S. Schmidt, A. B. Baggeroer, W. A. Kuperman, and E. K. Scheer. Environmentally tolerant beamforming for high-resolution matched-field processing: Deterministic mismatch. *J. Acoust. Soc. Am.*, 73:813–825, 1979.

[5] J. L. Krolik. Matched-field minimum variance beamforming in a random ocean channel. *J. Acoust. Soc. Am.*, 92:1408–1419, 1992.

[6] J. V. Candy and J. Sullivan. Model-based identification: An adaptive approach to ocean-acoustic processing. *IEEE Journal of Oceanic engineering*, 21:273–289, 1996.

[7] H. Cox, R. M. Zeskind, and M. M. Owen. Robust adaptive beamforming. *IEEE Transactions on Acoustics, Speech and Signal Processing*, 35(10):1365–1376, October 1987.

[8] A. B. Baggeroer and H. Cox. Passive sonar limits upon nulling mulyiple moving ships with large aperture arrays. *Proceedings of the IEEE, 33rd Asilomar Conference on Signals, Systems Computing*, pages 103–108, 1999.

[9] H. C. Song, W. A. Kuperman, W. S. Hodgkiss, P. Gerstoft, and J. S. Kim. Null broadening with snapshot-deficient covariance matrices in passive sonar. *IEEE Journal of Oceanic engineering*, 28:250–261, 2003.

[10] A. B. Baggeroer, W. A. Kuperman, and H. Schmidt. Matched-field processing: Source localization in correlated noise as an optimum parameter estimation problem. *J. Acoust. Soc. Am.*, 83:571–587, 1988.

[11] C. S. Clay. Optimum time domain signal transmission and source localization in a waveguide. *J. Acoust. Soc. Am.*, 81:660–664, 1987.

[12] S. Li and C. S. Clay. Optimum time domain signal transmission and source localization in a waveguide: Experiments in an ideal wedge waveguide. *J. Acoust. Soc. Am.*, 82:1409–1417, 1987.

[13] C. S. Clay and S. Li. Time domain signal transmission and source location in a waveguide: Matched filter and deconvolution experiments. *J. Acoust. Soc. Am.*, 83:1377–1383, 1988.

[14] R. K. Brienzo and W. S. Hodgkiss. Broadband matched-field processing. *J. Acoust. Soc. Am.*, 94:2821–2831, 1993.

[15] L. N. Frazer and P. I. Pecholcs. Single-hydrophone localization. *J. Acoust. Soc. Am.*, 88:995–1002, 1990.

[16] P. Hursky, M. B. Porter, and M. Siderius. High frequency (8-16 hz) model-base source localization. *J. Acoust. Soc. Am.*, 115:3021–3032, 2004.

[17] E. K. Westwood. Broadband matched-field source localization. *J. Acoust. Soc. Am.*, 91(5):2777–2789, May 1992.

[18] D. P. Knobles and S. K. Mitchell. Broadband localization by matched fields in range and bearing in shallow water. *J. Acoust. Soc. Am.*, 96:1813–1820, 1994.

[19] S. P. Czenszak and J. L. Krolik. Robust wideband matched-field processing with a short vertical array. *J. Acoust. Soc. Am.*, 101(2):749–759, February 1997.

[20] Z.-H. Michalopoulou and M. B. Porter. Matched-field processing for broadband source localization. *IEEE Journal of Oceanic engineering*, 21:384–392, 1996.

[21] Z.-H. Michalopoulou. Robust multi-tonal matched-field inversion: A coherent approach. *J. Acoust. Soc. Am.*, 104:163–170, 1998.

[22] G. J. Orris, M. Nicholas, and J. S. Perkins. The matched-phase coherent multi-frequency matched-field processor. *J. Acoust. Soc. Am.*, 107(5):2563–2575, 2000.

[23] H. L. Van Trees. *Optimum Array Processing, part IV of Detection, Estimation, and Modulation Theory*. Wiley-interscience, 2002.

[24] H. A. Chandler, C. Feuillade, and G. B. Smith. Sector-focused processing for stabilized resolution of multiple acoustic sources. *J. Acoust. Soc. Am.*, 97:2159–2172, 1995.

[25] W. M. Carey, J. Doutt, R. B. Evans, and L. M. Dillman. Shallow-water sound transmission measurements on the new jersey continental shelf. *IEEE Journal of Oceanic engineering*, 20:321–335, 1995.

[26] M. B. Porter. The kraken normal mode program (sm245). *SACLANT Undersea Research Center, La Spezia, Italy*, 1991.

Chapter 4

Fully coherent matched-field processing using a source phase estimation technique

4.1 Abstract

Source localization using matched-field processing (MFP) is typically problematic when the received sound levels are lower than a threshold signal-to-noise ratio (SNR). Broadband MFP offers an additional processing gain over narrowband methods by augmenting the data space, equivalent to increasing the number of hydrophones in the array. More specifically, coherent broadband methods which take further advantage of the temporal complexity of the signal than incoherent ones provide an added benefit in terms of localization performance. The detectability of the signal versus input SNR is evaluated for four types of conventional MFP algorithms using the detection index metric. The first is the narrowband MFP, the second incoherently averages the information across frequencies, the third treats the multiple frequencies information semi-coherently and removes the unknown source phases from the processing, and the fourth incorporates those phases making it a fully-coherent method. A technique to extract the source signal spectrum's phases from the data is presented and the added processing gain offered by the coherent methods is validated through theory, simulation and experimental data. The data derived variation of the detection index versus input SNR is shown to be consistent with the simulated results.

4.2 Introduction

Matched-field processing (MFP) techniques intend to provide range/depth localization of acoustic sources and/or information on the propagating media itself. Matched-field processing typically gets problematic when the signal-to-noise ratio (SNR) is low. Hence broadband processing, which takes advantage of the temporal complexity of the signal and therefore offers an additional gain over narrowband processing by augmenting the dimension of the data space, enhances the localization performance of the algorithm. This chapter quantifies the added benefit obtained by processing multiple frequencies coherently as opposed to incoherently using the detection index metric. The effect of canceling versus introducing the frequency-dependent unknown source phases in the coherent processing scheme

will be explored.

There typically are two ways to combine information across frequency.

1. One can do an incoherent broadband type of processing [1, 2, 3], where single frequency power outputs are averaged linearly or in dB in an effort to lower the sidelobes and increase the robustness of MFP to environmental uncertainties. The sum increases the detectability of the signal and robustness to mismatch when the environmental uncertainties cause a frequency-independent shift of the main lobe as opposed to the sidelobes.

2. Or one can exploit the cross-frequency complex information enlarging the data space and providing an extra-processing gain, with the drawback that these processors have to deal with the typically unknown complex spectral properties of the signal sent.

Broadband coherent methods use more information than incoherent ones by incorporating coherence across frequencies. The complexity of the impulse response between the source and receivers is therefore enhanced, decreasing the source localization's ambiguity. One important drawback of these algorithms is the need to predict the source phase accurately as a function of frequency, despite the signal sent by the source usually being unknown. Hence most coherent algorithms available to date cancel out the source phase by matching cross-correlation outputs of pairs of hydrophones [4, 5, 6, 7, 8], or by using the phase at one element to remove the unknown source phase on the remaining ones [9, 10]. Those methods are therefore better described as semi-coherent techniques, since they discard the source phase in the localization process.

Broadband coherent matched-field methods were first developed in the time-domain. The earliest work has been credited to Clay [6], who proposed to match measured and modeled impulse responses of transmission between the source and a receiver to estimate the source location. His method however requires knowledge of the source function. Clay and Li [5, 7] successfully used the technique to locate a source in an almost ideal laboratory rigid waveguide. Brienzo and Hodgkiss [11, 12] also localized a short range explosive source. The unknown source spectrum was

evaluated from the direct path arrival. Frazer and Pecholcs considered different types of norms and introduced five new single hydrophone algorithms, some of them requiring no *a priori* knowledge of the source function, but estimating it instead along with the source location [13]. Later on, Hursky *et al.* demonstrated the feasibility of high frequency time-domain localization [14]. When the source spectrum is not available, cross-correlating the signals received on two hydrophones cancelled out the unknown source phase.

Since adaptive MFP methods operate in the frequency domain, coherent broadband processors involving discrete frequencies are of particular interest. Westwood [4] was the first to develop an algorithm matching cross correlated measured impulse responses between pairs of receivers against modeled ones, the resulting complex function being summed coherently over frequencies. It differs from the time domain method introduced by Clay [6] in the sense that the output is not the maximum of the time-domain cross-correlations anymore, but the coherent summation of the narrowband cross-correlations. The unknown source phases cancel out by design. The information coming from auto-spectra, or in other words the diagonal terms of the single frequency cross-spectral density matrices (CSDM) has been discarded, since it can overpower the off-diagonal complex entries without contributing positively to the localization. The method was applied successfully to a shallow water experimental data set characterized by strong multipath. Czenszak and Krolik [8], on the other hand kept the auto-spectra information and formulated the algorithm in a quadratic form similar to single frequency MFP. A previously developed adaptive method, the environmental perturbation constraint [15], was applied to mitigate the higher sensitivity to mismatch resulting from the increased number of degrees of freedom.

Michalopoulou and Porter [9, 10] introduced a coherent algorithm based on matching received and modeled fields rather than cross-correlated pairs of received and modeled fields. One should note that since the unknown source phases across frequency do not cancel out anymore, the authors resorted to a normalization and cancellation scheme to remove the source's spectrum amplitude and phase, equalizing the source level at different frequencies. The resulting processor is therefore

coherent in the sense that the cross-frequency information is exploited. However since the information contained in the signal's spectrum is discarded in the process, we will refer to the method as semi-coherent in the rest of the dissertation. The processor tested on a real data set was shown to significantly improve the minimum variance distortionless response (MVDR) tracking accuracy in comparison to incoherent broadband techniques. Debever and Kuperman [16] combined it with the adaptive white noise constraint algorithm to enhance its robustness to environmental mismatch and snapshot deficiency. Orris *et al* considered the unknown source phases as free parameters to be determined using an optimization method [17]. The increased computational complexity however limits the use of the technique to a handful of frequencies.

An extensive amount of work has therefore been done to develop methods using frequencies in a coherent way. Amongst all of them, Michalopoulou and Porter's algorithm, herein referred to as the semi-coherent algorithm is chosen because its formulation builds on standard single frequency algorithms.

This chapter explores the effect of adding the source's phases information to the semi-coherent algorithm, making it fully-coherent. In Sec. 4.3, we first provide an overview of incoherent, semi-coherent and fully-coherent broadband MFP. We then introduce a phase estimation technique in Sec. 4.4 to evaluate the unknown source phases from the data itself. Sec. 4.5 presents the detection index theory [18, 19, 20, 21], used as a metric to study the reliability of the source localization versus input SNR using simulated data in Sec. 4.6 and data from the SWellEx-96 experiment in Sec. 4.7. Finally, Sec. 4.8 provides a summary and discussion.

4.3 Broadband matched-field models

Typically, a broadband source signal can be decomposed in the frequency domain into N_b frequency bins defined as $N_b = \frac{BW}{f_s/N_{fft}}$, where BW is the signal's bandwidth, f_s the sampling frequency and N_{fft} the number of points chosen to implement the Fourier transform of the signal. The information carried by each bin might not necessarily be independent from the one carried in adjacent bins,

and the actual number of degrees of freedom depends on the actual sampling and length of the emitted signal. In any case, the more information that is used to match the data on the array against synthetic fields coming from hypothetical source locations, the more accurate and discriminating the localization will be. Broadband MFP, a natural extension of single-frequency processing is therefore helpful in the presence of weak sources. This section describes the different ways available to combine information across frequency. A theoretical study of the expected coherent versus incoherent gain at the output of the processor is also provided.

4.3.1 Incoherent processing

Let $x_\omega^{(i)}$ denote the complex field received on the hydrophone i at angular frequency ω from a source at (R_s, Z_s) .

$$x_\omega^{(i)} = S(\omega)G^{(i)}(0, z_i, R_s, Z_s, \omega) + Q^{(i)}(\omega), \tag{4.1}$$

where $S(\omega)$ is the frequency dependent complex source spectrum, the expression $G^{(i)}(0, z_i, R_s, Z_s, \omega)$ the ocean waveguide's Green's function between the source location and the element i of the receiving array, and $Q^i(\omega)$ the complex noise component corrupting the signal.

Matched-field processing essentially is performing a sum of correlations between modeled and measured fields over elements. Typically, the complex field received on each hydrophone at one frequency is stacked in a (Nx1) vector, N being the number of elements in the array:

$$\boldsymbol{x}_\omega = \left[\; x_\omega^{(1)}, x_\omega^{(2)}, \ldots, x_\omega^{(N)} \; \right]^T, \tag{4.2}$$

where the notation ^{T} denotes the transpose operator. A modeled field on the array from a hypothetical source at (r, z) can be written in a (Nx1) vector as well, commonly called the replica vector, or weight vector $\boldsymbol{w}_\omega$.

The narrowband matched-field processor output is the correlation between received and modeled fields at various possible source positions along a grid in range and depth,

$$P\left(r, z\right) = \boldsymbol{w}_\omega^H\left(r, z\right) \boldsymbol{R}_\omega \boldsymbol{w}_\omega\left(r, z\right), \tag{4.3}$$

where $\boldsymbol{R}_\omega = E\{\boldsymbol{x}_\omega \boldsymbol{x}_\omega^H\}$ is the cross-spectral density matrix (CSDM) at angular frequency ω and the superscript H refers to the Hermitian transpose operation. In the conventional matched-field processor case, the weight vector is just the normalized Green's function

$$\boldsymbol{w}_\omega = \boldsymbol{d}_\omega = \frac{1}{\sqrt{\left(G_\omega^{(1)}\right)^2 + \ldots + \left(G_\omega^{(N)}\right)^2}} \left[\; G_\omega^{(1)}, \ldots, G_\omega^{(N)} \; \right]^T. \tag{4.4}$$

When the source emits a broadband signal, one can create an ensemble of single-frequency ambiguity surfaces. Because the position of the sidelobes is usually frequency dependent as opposed to the main lobe, a common approach proposed by Baggeroer *et al* is to incoherently average single-frequency ambiguity surfaces to suppress ambiguous sidelobes [1]. The conventional incoherent output can be written as:

$$P_{IC}\,(r,z) = \frac{1}{L} \sum_{k=1}^{L} 10log\left[\left|\boldsymbol{d}_k^H \boldsymbol{R}_k \boldsymbol{d}_k\right|\right]. \tag{4.5}$$

where L is number of frequencies processed.

Note that the frequency dependent phases of the source spectrum $S(\omega)$ in Eq. 4.1 cancel out in the process of forming the narrowband CSDMs, and do not need to be included in the replica vector for single-frequency and incoherent MFP in order to properly match the data represented by $\boldsymbol{R}_k$.

4.3.2 Coherent processing

To create a coherent processor, one can stack the narrowband signal vectors into one "supervector" of length $N \times L$.

$$\breve{\boldsymbol{x}} = \left[\; x_{\omega_1}^{(1)}, x_{\omega_1}^{(2)}, \ldots, x_{\omega_1}^{(N)}, \ldots, x_{\omega_L}^{(1)}, \ldots, x_{\omega_L}^{(N)} \; \right]^T. \tag{4.6}$$

From this supervector, a "super" CSDM can be constructed in the usual way, $\breve{\boldsymbol{R}} = E\{\breve{\boldsymbol{x}}\breve{\boldsymbol{x}}^H\}$. As opposed to incoherent processing, the extended cross spectral density matrix now exploits cross-frequency coherence as well. But because the signal emitted by the source has a characteristic signature in frequency represented by the complex term $S(\omega)$ in Eq. 4.1, the modeled field is now mismatched

with respect to the signal. To be fully-coherent, the processor has to first remove the phases of those complex terms for each frequency of the signal received.

$$\breve{\boldsymbol{x}} = \left[\; x_{\omega_1}^{(1)} e^{-j\,arg(S(\omega_1))}, \ldots, x_{\omega_L}^{(N)} e^{-j\,arg(S(\omega_L))} \; \right]^T. \tag{4.7}$$

The conventional MFP processor output can then be formulated as:

$$P_{FC}\,(r,z) = \breve{\boldsymbol{d}}^H \breve{\boldsymbol{R}} \breve{\boldsymbol{d}},$$

$$P_{FC}\,(r,z) = E\left[\left| \sum_{k=1}^{L} \boldsymbol{d}_k^H \boldsymbol{x}_k e^{-j\,arg(S(k))} \right|^2 \right]. \tag{4.8}$$

where FC stands for fully-coherent.

The position of the absolute value delimiters outside of the sum over frequencies as opposed to inside in Eq. 4.5 makes this algorithm fully coherent and generates cross-frequency terms.

In practice, the complex source spectrum is unknown, leaving the user with replicas mismatched with respect to the signal. Michalopoulou and Porter addressed this issue by scaling the phase of each single-frequency subvector $\boldsymbol{x}_k$ by the phase on the phone displaying the highest SNR, and normalizing the subvector to unit length [9, 10]. This compensation procedure effectively eliminates the unknown source terms in high SNR scenarios, but also equalizes the source level at different frequencies. To allow a comparison with the incoherent and fully-coherent algorithms, the method is slightly modified to keep the amplitude of the source terms, foregoing the subvector's normalization to unit length. The source phase cancellation is carried out and introduces the extra phase of the phone chosen to calibrate the other elements in the process. The algorithm is therefore not fully optimal, and will be referred to as semi-coherent in the rest of the paper.

If we denote the new subvector by $\overline{\boldsymbol{x}}_k$ and assume no contamination by noise and the first phone having the highest SNR:

$$\boldsymbol{x}_k = \begin{bmatrix} \left|S(k)G^{(1)}(k)\right| e^{j\left[arg(S(k))+arg(G^{(1)}(k))\right]} \\ \vdots \\ \left|S(k)G^{(N)}(k)\right| e^{j\left[arg(S(k))+arg(G^{(N)}(k))\right]} \end{bmatrix},$$

we have,

$$\overline{\boldsymbol{x}}_k = \begin{bmatrix} \left|S(k)G^{(1)}(k)\right| e^{j0} \\ \vdots \\ \left|S(k)G^{(N)}(k)\right| e^{j\left[arg(G^{(N)}(k)-arg(G^{(1)}(k))\right]}. \end{bmatrix}, \tag{4.9}$$

The semi-coherent conventional MFP output is given by:

$$P_{SC}\left(r,z\right) = E\left[\left|\sum_{k=1}^{L} \overline{\boldsymbol{d}}_{\boldsymbol{k}}{}^{H} \overline{\boldsymbol{x}}_{\boldsymbol{k}}\right|^2\right]. \tag{4.10}$$

When the amount of noise imbedded in the signal is not negligible, the phase normalization scheme described above carries an inherent mismatch due to the presence of the noise components [16]. Section 4.6 and 4.7 further discus the semi-coherent algorithm's performance versus signal-to-noise ratio.

4.3.3 Theoretical coherent gain

To better understand how much improvement one can expect from using the source spectrum's phases in the coherent processing, the gain obtained at the output of the diverse algorithms is investigated.

By definition, the processor's gain is the amount by which the signal is enhanced over the noise at the output of the processor. It is the ratio of the output SNR to the SNR at one sensor[21]. One way to estimate it is to divide the processor's output in the presence of signal only by its value in the presence of isotropic noise only and form the ratio of the quantity obtained by the mean input SNR over frequency at the elements.

In the incoherent broadband case, the individual single-frequency outputs are averaged:

$$P_{IC}\left(r,z\right) = \frac{1}{L}\sum_{k=1}^{L} |\frac{\boldsymbol{d}_k^H}{|\boldsymbol{d}_k|}\boldsymbol{x}_k\boldsymbol{x}_k^H\frac{\boldsymbol{d}_k}{|\boldsymbol{d}_k|}|, \tag{4.11}$$

where L is the number of frequencies processed.

Equation 4.11 is the same as Eq. 4.5 where the normalization of the weight vector has been written explicitly.

When the look position $\boldsymbol{d}$ coincides with the true source position, and assuming we can neglect mismatch between modeled and real environments, we have $\boldsymbol{x}_\omega = S(\omega)\boldsymbol{d}_\omega$ in the signal only case.

Equation 4.11 becomes:

$$P_{IC,signal\ only}(r,z) = \frac{1}{L}\sum_{k=1}^{L}|S(k)|^2|\boldsymbol{d}_k|^2. \tag{4.12}$$

When no signal is present in the data, but instead isotropic noise (*ie* spatially white), $E\left[\boldsymbol{x}_\omega \boldsymbol{x}_\omega^H\right] = |Q(\omega)|^2 I$, where I is the identity matrix.

$$P_{IC,noise\ only}(r,z) = \frac{1}{L}\sum_{k=1}^{L}|Q(k)|^2. \tag{4.13}$$

The mean input SNR at the elements is written as:

$$\begin{aligned} SNR_{input}(\omega) &= \frac{1}{N}\sum_{n=1}^{N}\frac{\left|S(\omega)d^{(n)}(\omega)\right|^2}{\left|Q^{(n)}(\omega)\right|^2}, \\ &= \frac{|\boldsymbol{d}_\omega|^2|S(\omega)|^2}{N|Q(\omega)|^2}, \end{aligned} \tag{4.14}$$

where N is the number of receivers. Finally, the mean input SNR over frequency at the elements takes the form:

$$\widetilde{SNR}_{input} = \frac{1}{NL}\sum_{k=1}^{L}\frac{|\boldsymbol{d}_k|^2|S(k)|^2}{|Q(k)|^2}, \tag{4.15}$$

where the operator $\widetilde{a}$ stands for averaging the quantity a over frequencies.

The incoherent broadband gain is given by:

$$\begin{aligned} Incoherent\ gain &= \frac{P_{Incoh,signal\ only}/P_{Incoh,noise\ only}}{\widetilde{SNR}_{input}}, \\ &= NL\frac{\left[\sum_{k=1}^{L}|S(k)|^2|\boldsymbol{d}_k|^2\right]/\left[\sum_{k=1}^{L}|Q(k)|^2\right]}{\sum_{k=1}^{L}|S(k)|^2|\boldsymbol{d}_k|^2/|Q(k)|^2}. \end{aligned} \tag{4.16}$$

If the noise level is assumed constant over frequencies, Eq. 4.16 reduces to:

$$Incoherent\ gain\ for\ flat\ noise\ spectrum = N. \tag{4.17}$$

In the particular case of isotropic, flat noise spectrum incoherent broadband gain is thus the same as the array gain. Averaging the frequency outputs does

not add any extra processing gain, but does decrease the level of the sidelobes significantly, rendering the localization more robust.

Similarly, the same type of reasoning can be applied in the fully and semi-coherent cases. The fully-coherent broadband output is given by:

$$\begin{aligned} P_{FC}(r,z) &= \left| \sum_{k=1}^{L} \frac{\boldsymbol{d}_k^H}{|\boldsymbol{d}_k|} \boldsymbol{x}_k e^{-jarg(S(k))} \right|^2, \\ &= \sum_{k=1}^{L} \sum_{q=1}^{L} \frac{\boldsymbol{d}_k^H}{|\boldsymbol{d}_k|} \boldsymbol{x}_k e^{-jarg(S(k))} \boldsymbol{x}_q^H e^{jarg(S(q))} \frac{\boldsymbol{d}_q}{|\boldsymbol{d}_q|}. \end{aligned} \tag{4.18}$$

In the absence of noise $\boldsymbol{x}_\omega = S(\omega)\boldsymbol{d}_\omega$, and since the signal is phase corrected, Eq. 4.18 becomes:

$$P_{FC,signal\ only}(r,z) = \sum_{k=1}^{L} \sum_{q=1}^{L} |S(k)||S(q)|\boldsymbol{d}_k||\boldsymbol{d}_q|. \tag{4.19}$$

When the signal is white noise, *i.e.* uncorrelated spatially and over frequency $E\left[\boldsymbol{x}_k \boldsymbol{x}_q^H\right] = |Q(k)||Q(q)|I\delta_{q,k}$, where δ is the Kronecker' function for which $\delta_{q,k} = 1$ if $q \neq k$ and $\delta_{q,k} = 0$ if $q = k$. Hence:

$$P_{FC,noise\ only}(r,z) = \sum_{k=1}^{L} |Q(k)|^2. \tag{4.20}$$

The fully-coherent broadband gain is given by:

$$\begin{aligned} Fully\ coherent\ gain &= \frac{P_{FC,signal\ only}/P_{FC,noise\ only}}{\widetilde{SNR}_{input}}, \\ &= NL \frac{\left[\sum_{k,q=1}^{L} |S(k)||S(q)|\boldsymbol{d}_k||\boldsymbol{d}_q|\right] / \left[\sum_{k=1}^{L} |Q(k)|^2\right]}{\sum_{k=1}^{L} |S(k)|^2 |\boldsymbol{d}_k|^2 / |Q(k)|^2} \end{aligned} \tag{4.21}$$

If the noise level is assumed constant over frequencies, Eq. 4.21 reduces to:

$$Fully\ coherent\ gain\ for\ flat\ noise\ spectrum = N \frac{\sum_{k,q=1}^{L} |S(k)||S(q)|\boldsymbol{d}_k||\boldsymbol{d}_q|}{\sum_{k=1}^{L} |S(k)|^2 |\boldsymbol{d}_k|^2}. \tag{4.22}$$

and

$$Fully\ coherent\ gain\ for\ flat\ noise\ and\ signal\ spectrums = NL, \tag{4.23}$$

when the signal's spectrum is flat as well.

Processing the frequencies coherently brings an extra-processing gain of L over the incoherent method when the signal's spectrum is flat.

The semi-coherent broadband output is written as:

$$\begin{aligned} P_{SC}(r,z) &= \left| \sum_{k=1}^{L} \frac{\left(\boldsymbol{d}_k e^{-jG^{(1)}(k)}\right)^H}{|\boldsymbol{d}_k|} \boldsymbol{x}_k e^{-j\left[arg\left(S(k)G^{(1)}(k)+Q^{(1)}(k)\right)\right]} \right|^2, \\ &= \sum_{k,q=1}^{L} \frac{\left(\boldsymbol{d}_k e^{-jG^{(1)}(k)}\right)^H}{|\boldsymbol{d}_k|} \boldsymbol{x}_k e^{-j\left[arg\left(S(k)G^{(1)}(k)+Q^{(1)}(k)\right)\right]} \qquad (4.24) \\ &\quad \boldsymbol{x}_q^H e^{j\left[arg\left(S(q)G^{(1)}(q)+Q^{(1)}(q)\right)\right]} \frac{\left(\boldsymbol{d}_q e^{-jG^{(1)}(q)}\right)}{|\boldsymbol{d}_q|}. \qquad (4.25) \end{aligned}$$

if the first phone is chosen in the normalization process.

Hence:

$$P_{SC,signal\ only}(r,z) = \sum_{k,q=1}^{L} S(k)S(q)^* |\boldsymbol{d}_k||\boldsymbol{d}_q| e^{j\phi_{k,q}} e^{-j\psi_{k,q}}, \qquad (4.26)$$

where $\phi_{k,q} = \left[arg\left(S(q)G^{(1)}(q) + Q^{(1)}(q)\right) - arg\left(S(k)G^{(1)}(k) + Q^{(1)}(k)\right)\right]$, $\psi_{k,q} = \left[arg\left(G^{(1)}(q)\right) - arg\left(G^{(1)}(k)\right)\right]$ and the asterix denotes the complex conjugate operation.

For white noise only:

$$P_{SC,noise\ only}(r,z) = \sum_{k=1}^{L} |Q(k)|^2. \qquad (4.27)$$

The semi-coherent broadband gain is given by:

$$\begin{aligned} Semi\ coherent\ gain &= \frac{P_{SC,signal\ only}/P_{SC,noise\ only}}{\widetilde{SNR}_{input}}, \\ &= NL \frac{\sum_{k,q=1}^{L} S(k)S(q)^* |\boldsymbol{d}_k||\boldsymbol{d}_q| e^{j\phi_{k,q}} e^{-j\psi_{k,q}} / \sum_{k=1}^{L} |Q(k)|^2}{\sum_{k=1}^{L} |S(k)|^2 |\boldsymbol{d}_k|^2 / |Q(k)|^2} \qquad (4.28) \end{aligned}$$

In presence of white, flat noise, the two extremes cases of high input SNR and low input SNR respectively yield:

$$Semi\ coherent\ gain\ at\ high\ SNR = N \frac{\sum_{k,q=1}^{L} |S(k)||S(q)|\boldsymbol{d}_k||\boldsymbol{d}_q|}{\sum_{k=1}^{L} |S(k)|^2 |\boldsymbol{d}_k|^2}, \qquad (4.29)$$

which is the same expression as the one obtained in Eq. 4.22 for the fully-coherent gain, and

$$\textit{Semi coherent gain at low } SNR = N\frac{\sum_{k,q=1}^{L}|S(k)||S(q)||\boldsymbol{d}_k||\boldsymbol{d}_q|e^{j\phi_{k,q}}e^{-j\psi_{k,q}}}{\sum_{k=1}^{L}|S\left(k\right)|^2|\boldsymbol{d}_k|^2}. \tag{4.30}$$

Thus the semi-coherent gain is between the incoherent and the fully-coherent gains.

Because of the phase scaling process detailed in Sec. 4.3.2, the semi-coherent processor's gain implicitly is a function of the input SNR, as opposed to the incoherent and fully-coherent techniques. Indeed, at SNRs such that the noise is not negligible compared to the signal, the noise at the receiver used to calibrate the other elements is introduced on all hydrophones via the phase correction scheme. At low input SNR, the replica therefore becomes mismatched with respect to the data, and in effect the expected gain at the output of the semi-coherent processor decreases.

Those theoretical considerations suggest that there is indeed an additional processing gain obtained by incorporating the source spectrum's phases into the coherent processing scheme. The rest of the paper will explore this assumption using simulated and experimental results.

4.4 Estimation of the source phases

As apparent in Eq. 4.7, the fully-coherent method requires knowledge of the frequency dependent source spectrum phases in order to fully match the replica field to the received one. In this section, a technique is proposed to estimate those unknown phases without any a priori information on the source's position.

The received field $\boldsymbol{x}_\omega$ and conventional replica vector $\boldsymbol{d}_\omega$ at the frequency ω are expressed as:

$$\boldsymbol{x}_\omega = \begin{bmatrix} S(\omega)G^{(1)}(0, z_1, R_s, Z_s, \omega) + Q^{(1)}(\omega) \\ \vdots \\ S(\omega)G^{(N)}(0, z_N, R_s, Zs, \omega) + Q^{(N)}(\omega) \end{bmatrix}, \tag{4.31}$$

and

$$\boldsymbol{d}_{\omega}(r,z) = \frac{1}{\beta}\begin{bmatrix} G^{(1)}(0,z_1,r,z,\omega) \\ \vdots \\ G^{(N)}(0,z_N,r,z,\omega) \end{bmatrix}, \tag{4.32}$$

where $\beta = \sqrt{|G^{(1)}(0,z_1,r,z,\omega)|^2 + \ldots + |G^{(N)}(0,z_N,r,z,\omega)|^2}$ is a coefficient of normalization.

If the noise is assumed negligible compared to the signal level, the phase of the inner product between the signal and replica at frequency ω is given by:

$$arg\left(\boldsymbol{d}_{\omega}^{H}\boldsymbol{x}_{\omega}\right) = arg\left(S(\omega)\right) + arg\left(\sum_{i=1}^{N} G^{(i)}(0,z_i,r,z,\omega)^{*} G^{(i)}(0,z_i,R_s,Z_s,\omega)\right). \tag{4.33}$$

Note that when the replica vector corresponds to a simulated signal coming from the true source position, *ie* $(r,z) = (R_s, Z_s)$, the phase of the inner product reduces to the desired phase of the signal's spectrum at frequency ω.

We now modify the fully-coherent algorithm in Eq. 4.8 by phase-correcting the signal by the phase of the inner product between the signal and the replica at (r,z) instead of the (in fact unknown) source phases.

$$Phase\ corrected\ coh\,(r,z) = E\left[\left|\sum_{k=1}^{L} \boldsymbol{d}_{k}^{H}(r,z)\boldsymbol{x}_{k} e^{-j\,arg\left(\boldsymbol{d}_{k}^{H}(r,z)\boldsymbol{x}_{k}\right)}\right|^{2}\right]. \tag{4.34}$$

The data matched to the bank of replica vectors is now different for each grid point in range and depth. When $(r,z) = (Rs, Zs)$, the data is phase-corrected by the frequency-dependent source phases, yielding a maximum in the output. The source phase estimate is therefore given by the phase of Eq. 4.33 at the range and depth of the maximum output of the phase estimator.

Note that the algorithm in Eq. 4.34 provides an estimate of the source location as well. But because the phase compensation introduced is a function of range and depth, it will affect the structure of the sidelobes. For comparison purposes with the incoherent and semi-coherent methods we will determine the source

phase from the peak of the "phase-corrected" coherent processor and implement a fully-coherent ambiguity surface with the estimated phase according to Eq. 4.8.

When the noise level is not negligible with respect to the signal, the phase of the inner-product at the appropriate range and depth is not just the source phases anymore, but a combination of the source, Green's function and noise phases.

Two scenarios can happen:

1. The contamination of the signal by noise is not significant enough to change the position of the peak of the phase estimator given by Eq. 4.34. In that case, the phase obtained from Eq. 4.33, despite being somewhat different from the source phases still allows maximum coherence over frequencies. Indeed, if we denote $\boldsymbol{d}_k^H(r,z)\boldsymbol{x}_k$ as $T_k(r,z)$, the "fully-coherent" algorithm given by Eq. 4.8 becomes:

$$P_{FC\_est}(r,z) = E\left[\left|\sum_{k=1}^{L} T_k(r,z)e^{-iarg(T_k(Rs,Zs))}\right|^2\right] \tag{4.35}$$

   When $(r,z) = (R_s, Z_s)$, the terms in the sum of Eq. 4.35 are real and sum optimally.

2. The power of the noise is such that the peak of the phase estimator if even existent is not at the true source position. In that case the output of the fully-coherent processor will give a wrong estimate of the source position.

The method of estimating the source phases is of interest from a practical standpoint only if it works at SNR sufficiently low to offer an advantage in using the fully-coherent processor versus the semi-coherent algorithm.

4.5 The detection index performance metric

Section 4.3 introduced different broadband algorithms exploiting cross frequency coherence to various degrees. We would like to quantify the benefit of using broadband versus narrowband, and coherent versus incoherent broadband methods as a function of input SNR at each element. The detection index metric is chosen as a measure of a processor's detection performance.

Detection theory literature addresses the question of whether the signal is present or not in an observation, and how to implement an optimum detector for a certain detection criterion [18, 19, 21]. Typically, if we call $x(n), n \in [1, N_{samples}]$ the received data we assume that there are two hypothesis:

$$\begin{aligned} \mathcal{H}_0 &: x(n) = w(n), \\ \mathcal{H}_1 &: x(n) = s(n) + w(n). \end{aligned} \tag{4.36}$$

$\mathcal{H}_0$ is the null hypothesis of noise only present in the observation, and $\mathcal{H}_1$ the hypothesis of signal present in noise.

The test statistic λ_T is defined as the ratio of the likelihood of x given that $\mathcal{H}_1$ is true over the likelihood of x given that $\mathcal{H}_0$ is true. The higher λ_T, the more detectable a signal will be. This ratio is commonly used in detection theory to maximize the probability of detection over the probability of false alarm. The deflection coefficient d_f is a measure of the change in the expected value of the test statistic when the signal is present as opposed to the noise-only case:

$$d_f^2 = \frac{\left(E\left[\lambda_T|\mathcal{H}_1\right] - E\left[\lambda_T|\mathcal{H}_0\right]\right)^2}{var(\lambda_T|\mathcal{H}_0)}. \tag{4.37}$$

When the observation is a power $I(n) = \dfrac{1}{N_{samples}}|x(n)|^2$ as is the case for the MFP processor output, the deflection coefficient becomes:

$$d_f^2 = \frac{E\left[\lambda_T^I|\mathcal{H}_1\right] - E\left[\lambda_T^I|\mathcal{H}_0\right]}{\sqrt{var(\lambda_T^I|\mathcal{H}_0)}}, \tag{4.38}$$

where λ_T^I is the ratio of the likelihood of I given that $\mathcal{H}_1$ is true over the likelihood of I given that $\mathcal{H}_0$ is true.

The detection index $D = 10log(d_f^2)$ gives a metric to compare the different processor's performance as the signal gets weaker and weaker. Simulated and experimental results are presented in Sec. 4.6 and 4.7 respectively.

4.6 Simulated detection index versus SNR

In this section, the localization performance of narrowband, broadband incoherent, semi-coherent and fully-coherent conventional MFP is investigated using

simulation. Specifically, the importance of incorporating the source term information into the coherent processing and the extra-processing gain associated with it is examined.

The SWellEx-96 experiment data set [22] has been chosen for use in this paper in part because of the extensive study of the environment conducted, providing us with an accurate description of the media, but also because of the low ocean variability over the duration of the experiment. The experiment also featured a source broadcasting tonals of various power level, allowing a study of the processor's performance versus input SNR. The SWellEx experimental environment is used in this section to create a synthetic signal for which the complex source terms are known exactly and can be exploited. Results from processing the data itself will be provided in Sec. 4.7.

The experiment took place in shallow water (216 m) off San Diego, California. Two acoustic sources were towed along an isobath, transmitting multitonal components at various strengths between 50 and 400 Hz, and the acoustic field was sampled by a vertical, tilted and two horizontal arrays. The acoustic signal received from the deep source (54 m) on the 21-element vertical array will be used in the rest of the paper. The SWellEx environment is illustrated in Fig. (4.1).

A simulated signal on the array consisting of 42-snapshots is created using a normal mode propagation model [23], such that SNR=-5dB at each element. The signal is composed of thirteen tones of frequencies 49, 64, 79, 94, 112 130, 148, 166, 201, 235, 283, 338 and 388 Hz, each associated with a known signal spectrum phase. The synthetic source is positioned 54 m deep, 4475 m away from the array.

Figure (4.2) displays the single-frequency conventional MFP output obtained at 49 Hz. The source is correctly localized, but the presence of high sidelobes renders the localization ambiguous. Incoherently averaging the ambiguity surfaces from 13 tonals shown in Fig. (4.3) lowers the sidelobes level to 5 dB below the main lobe, allowing for successful source localization. In Fig. (4.4), the cross-frequency coherence is now exploited in the processing, but the source spectrum's information in assumed unknown and cancelled out from the algorithm, as described in the semi-coherent case in Sec. 4.3.2. The extra processing gain

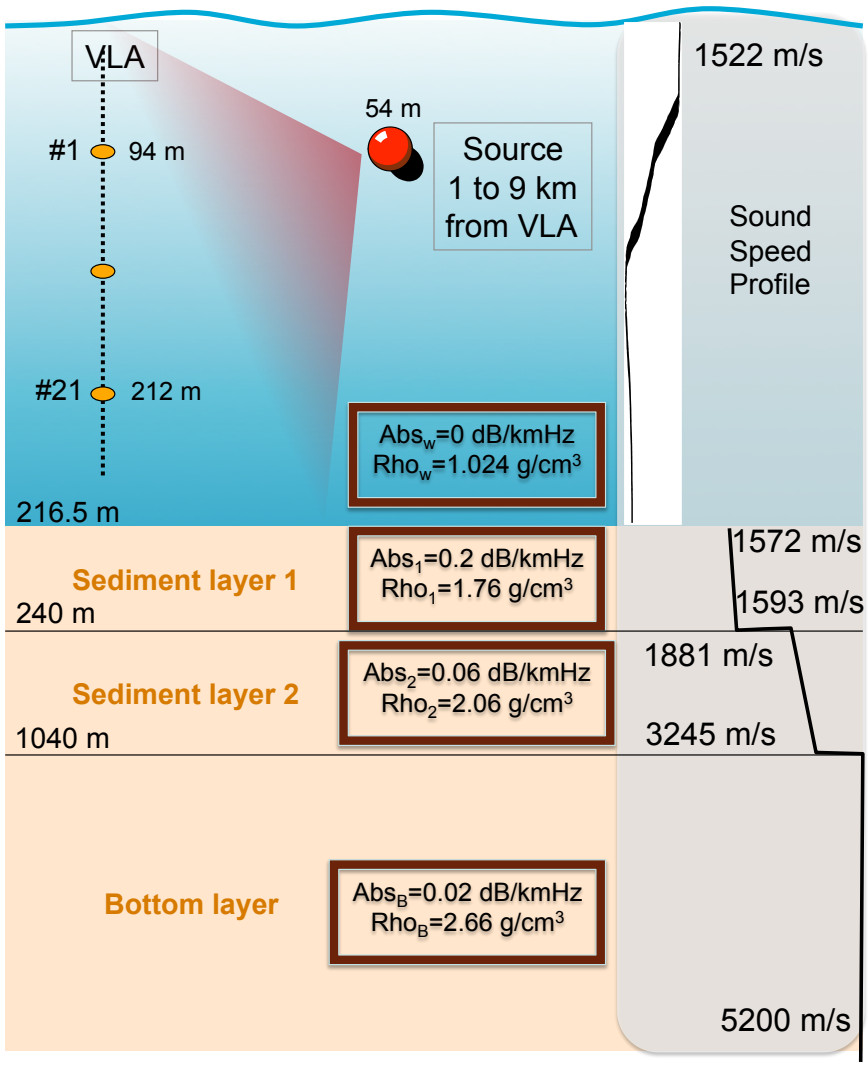

Figure 4.1: The SWellEx environment features a 21 element vertical array and an acoustic source towed at 54 m deep from 1 km to 9 km away from the array.

associated with the cross-frequency data space lowers the sidelobes to 6 dB below the maximum. The source's detectability over noise is greatly improved. Finally, adding the true source phase information to the processing significantly lowers the level of the sidelobes to 12 dB below the main-lobe level, as shown on Fig. (4.5) and (4.6).

The phase estimation technique described in Sec. 4.4 is now applied, and the fully-coherent MFP output obtained with the estimated source phases as in Equation 4.8 is presented in Fig. (4.7). Figure (4.6) shows the fully-coherent output with true source phases with an increased dynamic range of [-22 dB 0 dB] for comparison purposes. The ambiguity surfaces obtained with an estimate of the source phase versus knowledge of the true phase are similar.

The validity of the the theoretical gain predictions in Sec. 4.3.3 is now investigated. The basal noise level of an ambiguity surface is estimated in this study by averaging the lowest values of the surface. The main lobe level minus basal noise level obtained is referred to as peak-to-background level in the rest of the Chapter. Figure (4.8) shows the simulated peak-to-background output of the incoherent, semi-coherent, fully-coherent using the true source phases and fully-coherent using estimated source phases processors divided by the mean input SNR over elements and frequencies and the array gain as the number of frequencies included in the processing is varied. In other words, the plot's vertical axis shows the magnitude of the processor's gain due to using multiple frequencies. Fifteen iterations of 42 snapshots at 20, 5 and -5 decibels input SNR were created, and the average peak-to-background ratio over iterations computed. The noise added to the signal is white.

According to Eq. 4.17, 4.23 and 4.28, we expect the incoherent MFP output's dynamic range to be invariant with the number of frequencies used, and the fully-coherent case to be linearly increasing with frequency. The semi-coherent algorithm doesn't quite take advantage of the full cross-frequency information and is expected to show an extra gain versus number of frequencies processed somewhere in between the incoherent and fully-coherent cases. The lower the input SNR, the closer the gain to the incoherent processor. The simulated results confirm the

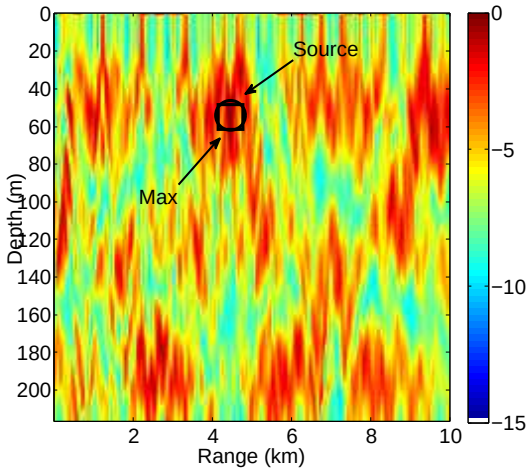

Figure 4.2: Simulated output from the single-frequency conventional MFP at 49 Hz, SNR=-5 dB.

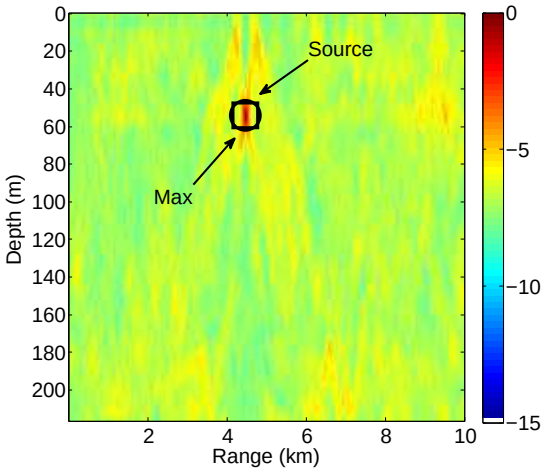

Figure 4.3: Simulated output from the incoherent broadband conventional MFP using 13 frequencies between 50 and 400 Hz, SNR=-5 dB.

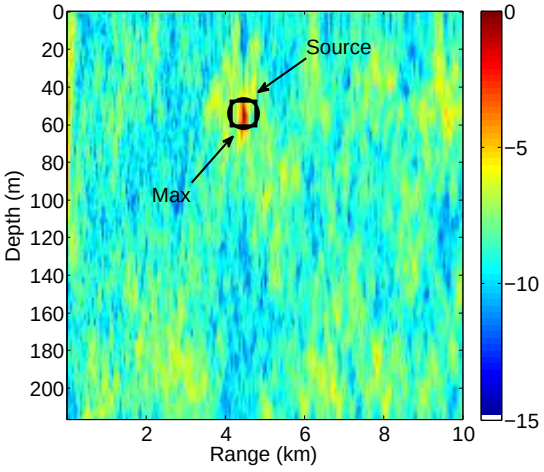

Figure 4.4: Simulated output from the "semi-coherent" broadband conventional MFP using 13 frequencies between 50 and 400 Hz, SNR=-5 dB.

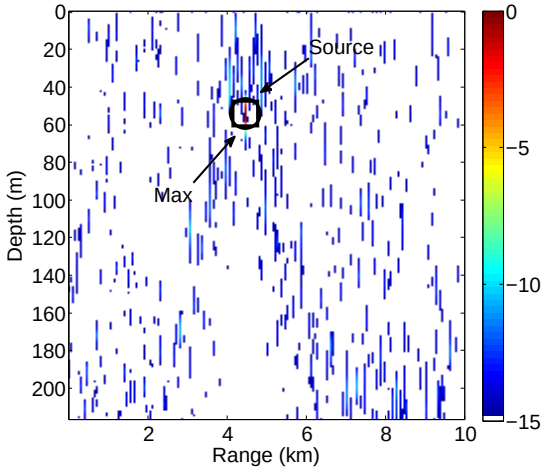

Figure 4.5: Simulated output from the "fully-coherent" broadband conventional MFP using 13 frequencies between 50 and 400 Hz, SNR=-5 dB. The true complex source phases are incorporated into the processing.

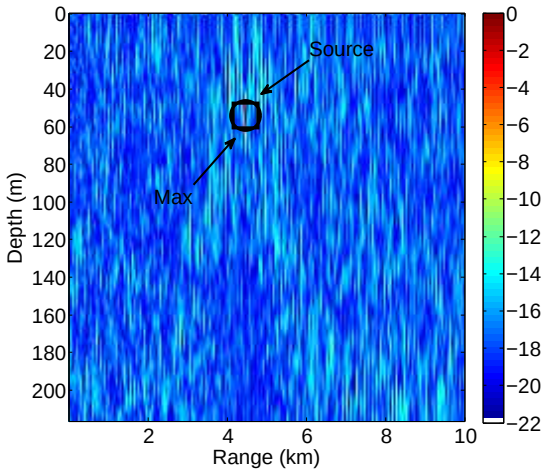

Figure 4.6: Simulated output from the "fully-coherent" broadband conventional MFP using 13 frequencies between 50 and 400 Hz, SNR=-5 dB. The true complex source phase is incorporated in the processing, which lowers the sidelobes to -12 dB, 5 dB lower than without use of the source spectrum information. The dynamic range is lowered to -22 dB to visualize the sidelobes and background noise.

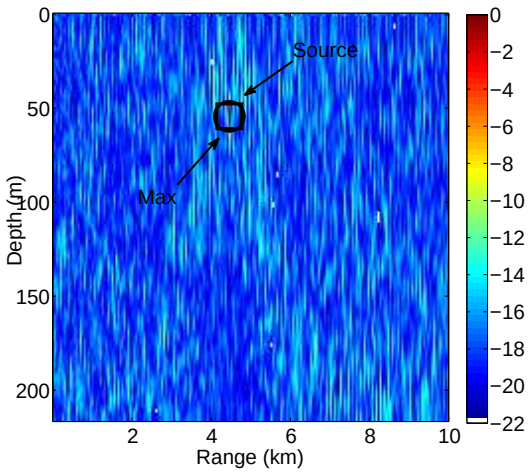

Figure 4.7: Simulated output from the "fully-coherent" broadband conventional MFP using 13 frequencies between 50 and 400 Hz, SNR=-5 dB. The estimated complex source phase is incorporated in the processing. The ambiguity surface is similar to the one obtained using the true source phase.

theoretical predictions.

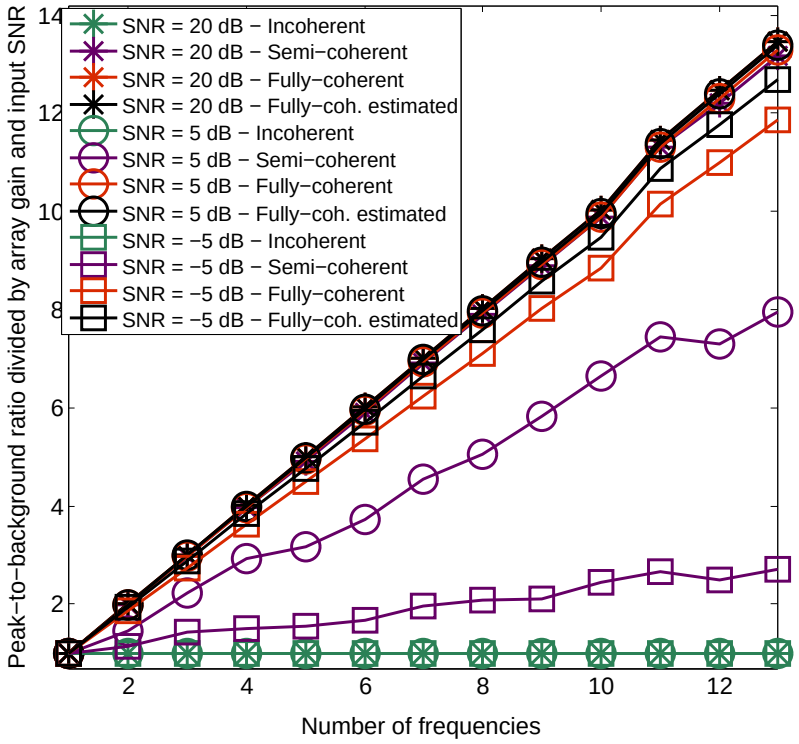

Figure 4.8: Function showing the evolution of each processor gain as a function of number of frequencies used in the algorithm. Three averaged input SNRs over frequencies and elements were compared; 20 dB, 5 dB and -5 dB at each element. As expected, the incoherent MFP does not display any extra gain as the number of frequencies utilized increased, the "fully-coherent" MFP coherent gain is proportional to the number of frequencies and the "semi-coherent" MFP coherent gain is close to the incoherent one at low SNR and "fully-coherent" one at high SNR.

This simple simulated case illustrates the improvement in detectability obtained when incorporating the source's spectrum information to the semi-coherent algorithm. Those results suggest that an extra processing gain over incoherent and semi-coherent methods is obtained when matching the frequency components corrected by the true source phases to the modeled pressure fields. Does this however imply that the fully coherent algorithm is able to detect weaker sources than the other types of broadband processors?

To answer this question, a comparison of the different processor's simulated performance as a function of input SNR at each element is performed using the detection index metric presented in Sec. **??**. The input SNR averaged over frequencies and elements is varied from -25 to 5 decibels in increments of 1 decibel. For each SNR, 20 iterations of 42 signal plus noise and noise only snapshots are created. The output of the processors at the correct source's range-depth obtained from a CSDM formed with signal plus noise snapshots gives the expected value of $\{\lambda_T^I|\mathcal{H}_1\}$. $\{\lambda_T^I|\mathcal{H}_0\}$ is given by the output of the processors at the same location using a noise-only CSDM. Likewise, $var(\lambda_T^I|\mathcal{H}_0)$ is given by the variance of the outputs in the noise-only case over the 20 iterations.

Figure (4.9) displays the simulated detection index obtained. As expected, the bigger the input SNR, the more detectable the signal is at the output of all processors. Broadband processing also improves detection over narrowband methods for all input SNRs. Interestingly, the semi-coherent algorithm displays a detection index lower than the incoherent one at all negative SNRs, despite the contrast between main lobe and sidelobe levels being larger on Fig. (4.4) than Fig. (4.3). This is due to the variance of the noise in the denominator of Eq. 4.38 being bigger at the output of the semi-coherent broadband processor than at the output of the incoherent processor. On the other hand, the detectability of the signal in the fully-coherent broadband processor case is the highest at all input SNRs, and its detection index is about 5 dB above the incoherent processor one, and 10 dB above the single-frequency and semi-coherent algorithms.

Those results suggest that the phase estimation technique provides us with estimates of the source phases good enough to implement a fully-coherent method, and that incorporating those phases into the semi-coherent algorithm, making it fully-coherent brings a noticeable improvement to the main lobe to sidelobe ratio and detectability of the signal.

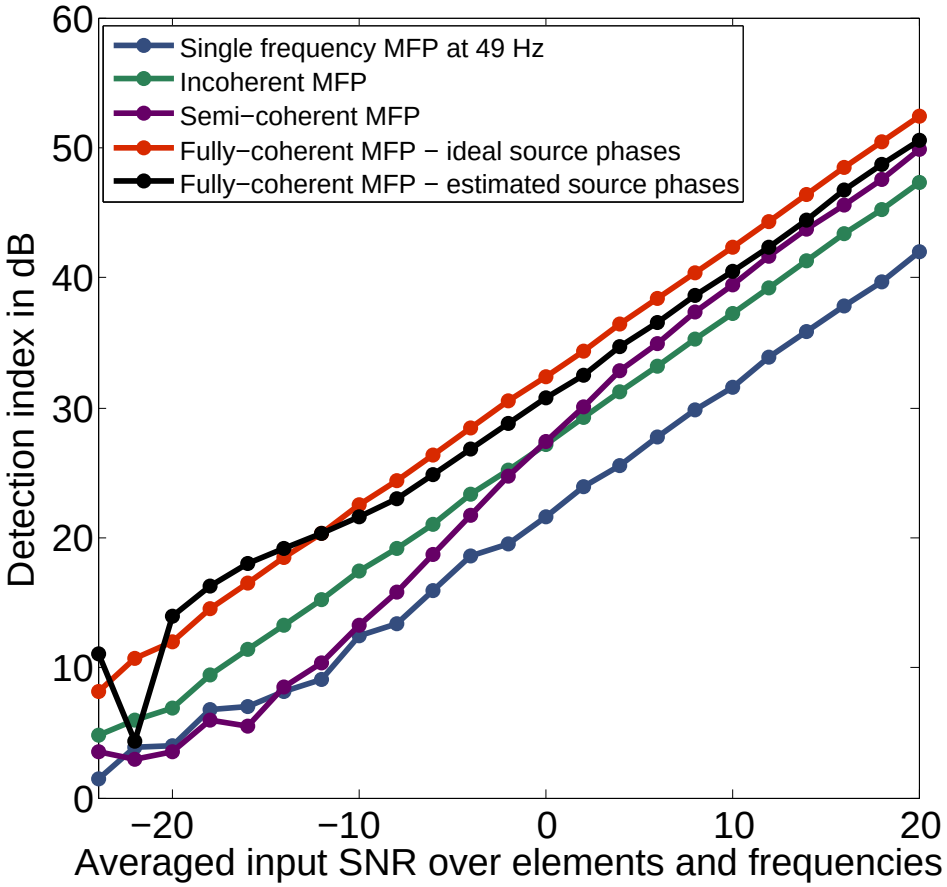

Figure 4.9: Simulated detection index of the single-frequency at 49 Hz, incoherent, semi-coherent, fully coherent with true source phase and fully-coherent with estimated source phase matched-field processors as a function of the averaged input SNR over frequencies and elements.

4.7 Experimental detection index versus SNR

Theory and simulation both show that incorporating the source phase information to the coherent processing scheme provides an additional "coherent" gain over the semi-coherent method. Is the phase estimation technique introduced in Sec. 4.4 robust enough to environmental mismatch to take advantage of the coherent gain using experimental data?

The SWellEx-96 experiment, described in Sec. 4.6 is well suited for broadband coherent algorithms comparison as a function of input SNR. The source transmitted 5 sets of 13 tonals at various levels spanning the frequencies between 49Hz and 400Hz. The first set of 13 tonals was projected with transmitted levels of about 158 dB for each tonal, the second set at approximately 132 dB, and each subsequent set 4 dB down from the previous set.

The source was towed along an isobath from 1 to 9 km away from the array. Despite each set of tonals being transmitted at a fixed level, the transmission loss occurring during the propagation in the waveguide provides us with incoming data at various input SNR on the receiver array, depending on the distance between the source and the array at the time of transmission.

The first step in creating an experimental detection index curve versus input SNR is to estimate the averaged SNR over frequencies and elements along the source track. The highest set of tones is loud enough (around 10 to 20 dB at each element depending on the source/array distance) to assume that the noise is negligible and we obtain an estimate of the signal and noise levels from the received field's spectrum every two minutes. Once the input SNR is estimated along the track for the powerful tones, the corresponding SNR for the weaker sets of tones is calculated knowing that the second set was projected 26 dB down the first one, then 4 dB down for each subsequent set.

The data is then grouped by input SNR and the single frequency, incoherent, semi-coherent and fully coherent with estimated source phase processors are implemented using the "signal plus noise" data and the "noise-only" data for those times. The "noise-only" data is obtained from the frequencies 62, 77, 92, 107 125, 143, 161, 179, 214, 248, 296, 351 and 401 Hz. An estimate of the experimental

detection index for each input SNR can then be determined.

Figure (4.10) shows the experimental curves obtained in dots. As expected, the fully-coherent algorithm with the estimated source phase integrated into the cross-frequency processing displays the highest level of detection index by 5 to 10 decibels above the next processor. The estimate of the source phase becomes inaccurate as the noise increases and the fully-coherent processor's detection index suddenly drops down to the level of the other processors around SNR=-10 dB. For SNR between -5 and -10 decibels, only the fully-coherent and incoherent processors successfully detect the source, with the fully-coherent detection index being 10 decibels above the incoherent one. The semi-coherent method shows a higher detectability than the incoherent one by a couple decibels for SNR above 10 dB, but drops 2 decibels below the incoherent one under 10 dB SNR. Incorporating the source phase to the processing therefore improves the detectability of the source over the semi-coherent method.

Note that a comparison between Fig. (4.9) and (4.10) shows that the simulated detection index curves in Fig. (4.9) are about 10 dB higher than the experimental ones. This is due to the nature of the noise added to the signal in the simulation. Indeed, snapshots of isotropic white noise at various SNR were implemented to create Fig. (4.9), however a closer inspection of the experimental noise cross-spectral density matrices showed the presence of spectrally and spatially colored noise in addition to white noise. To be consistent with the experimental environment, a new simulation was performed using noise snapshots which reproduced the experimental noise CSDM using the Cholevsky decomposition method [24], and varying the power of those noise snapshots to obtain the input SNR desired.

The new simulated detection index curves are superimposed to the experimental ones on Fig. (4.10). A number of differences between the curves obtained with white-noise snapshots in Fig. (4.9) and colored-noise snapshots in Fig. (4.10) are noticed. While the slopes of detection indexes versus input SNR remain mostly unchanged when changing from white to colored noise, the detection index curves obtained with colored noise are about 10 decibels lower than the corresponding

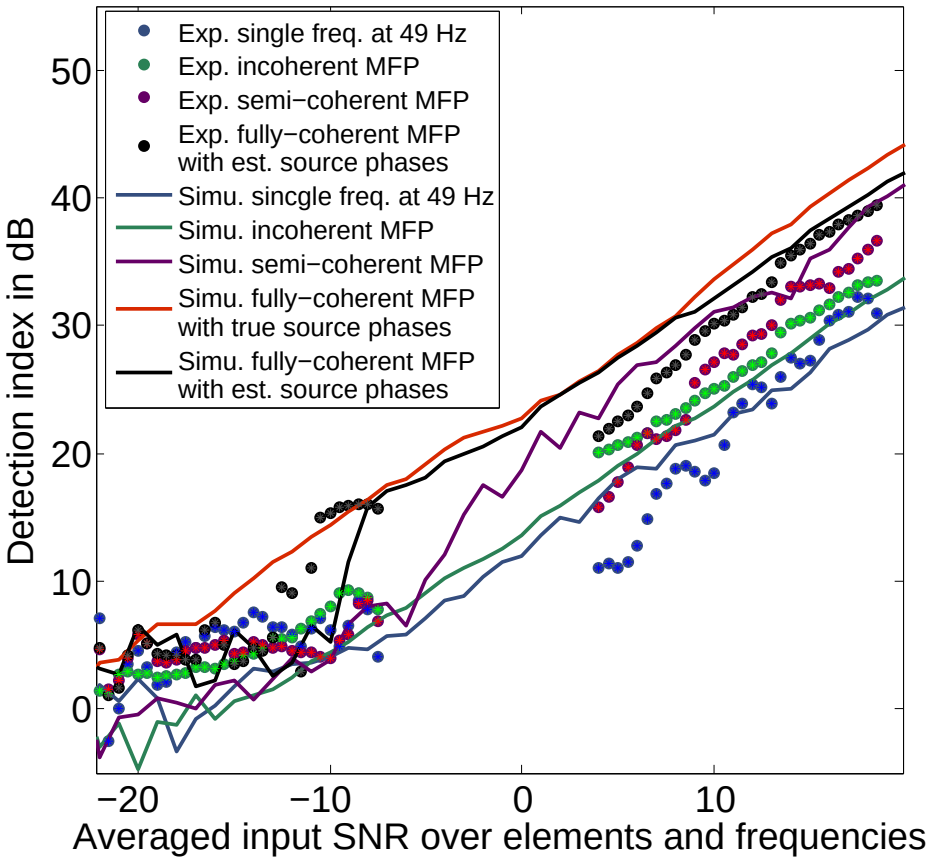

Figure 4.10: Experimental detection index of the single-frequency at 49 Hz, incoherent, semi-coherent and fully-coherent with estimated source phase matched-field processors as a function of the averaged input SNR over frequencies and element in dots, using data from the SWellEx-96 experiment. Simulated curves using noise snapshots created from the experimental noise CSDM are superimposed in plain lines.

white noise ones. This is because the variance of the noise apparent in the denominator of the detection index's formulation in Eq. 4.38 is larger for colored than white noise.

The discrepancy between the simulated semi-coherent and fully-coherent curves and the experimental ones for positive SNRs is likely due to the presence of environmental mismatch. Indeed, the experimental points between 5 and 20 dB input SNR were obtained from the highest level of tones along the source track. The closer the source was to the array, the higher the input SNR recorded. In the presence of mismatch between the environment used to create the synthetic field and the real ocean, we expect the simulated fields far from the array to be more affected by the mismatch present than close to the array. We also expect the coherent methods to be more sensitive to environmental fluctuations and modeling parameters errors than the narrowband and incoherent processors.

To validate the presence of environmental mismatch, we progressively add more and more data-derived colored noise to the signal obtained when the source is the closest to the array, corresponding to an averaged input SNR over frequencies and elements of 18 dB. According to our assumption that the slopes of experimental and simulated detection index versus SNR differ because of mismatch being more and more problematic as the source range increases, we expect that adding synthetic noise to the least affected by mismatch data recording should give results similar to the mismatch-free simulation. Figure (4.11) shows the experimental fully-coherent detection index curve versus SNR in dots, the mismatch-free simulated one in dotted line, and the one obtained by adding synthetic noise to the data of highest SNR in plain line with square markers. Two cases are considered for the fully-coherent method: (1) the source phase is estimated from the highest SNR data only, shown in grey and (2) the source phase is estimated from the noisy data at each SNR in black. The new hybrid curves do agree with the mismatch-free simulated ones, suggesting that there is indeed a non negligible amount of inaccuracies between our model of the environment and the true ocean. The fully-coherent detection index using source phases derived from the highest SNR data is a couple dB higher than the one using an estimate of the phase at each SNR. It

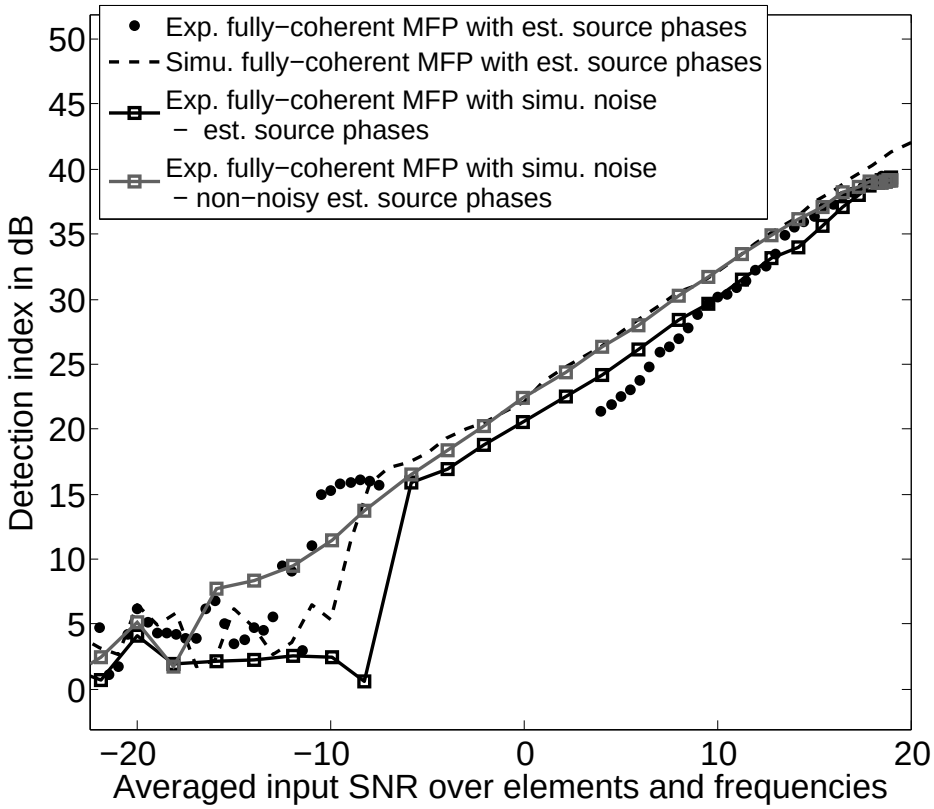

Figure 4.11: Experimental detection index of the fully-coherent with estimated source phase matched-field processor as a function of the averaged input SNR over frequencies and elements in dots, using data from the SWellEx-96 experiment. The simulated curve using noise snapshots generated from the experimental noise CSDM is superimposed in dotted line. The plain line with square markers represents the detection index obtained from gradually augmenting the amount of colored noise added to the data at 18 dB at mean input SNR. Tow cases are pictured: (1) the phase is evaluated from the noisy data shown in black, (2) the phase is evaluated from the data at 18 dB input SNR in grey.

also doesn't show a sudden drop around -8 dB SNR due to the phase estimation technique becoming problematic at low SNR, as expected.

Simulation and experimental results suggest that there is indeed an extra-processing gain and added detectability obtained by incorporating the source phase into the semi-coherent processor previously discussed in the literature. Does the fully-coherent broadband algorithm also exhibit better localization performance than the other processors?

Data from the two highest sets of tonals is processed along the source track, and the main lobe minus highest sidelobe level is determined for cases when the source was localized with an accuracy of 250 m in range and 15 m in depth. Figure (4.12) displays the results obtained using the single-frequency, incoherent, semi-coherent and fully-coherent with estimated source phase processors. Only successful localization are represented. These results show that the fully-coherent method displays the highest peak-to-sidelobe ratio for all mean input SNR (between 4 and 8 dB main lobe to sidelobe level). The incoherent and semi-coherent methods peak-to-sidelobe levels decrease with input SNR at a faster rate than with the fully-coherent processor (from 5 to 1 dB for the semi-coherent and 4 to 0 dB main lobe to sidelobe level for the incoherent processor). The single-frequency processor displays sidelobes nearly as high as the main lobe, and is therefore not suited for practical purposes. Moreover, for input SNR lower than 0 dB, only the fully-coherent and incoherent methods localize the source correctly, but the incoherent processor's sidelobes are less than a dB below the main-lobe, rendering localization ambiguous.

Adding the source phases into the processing therefore improves not only the signal's detectability, but also its localization at the right place.

4.8 Summary and conclusion

The benefit of broadband versus narrowband processing on acoustic source localization and detection has been evaluated for different input SNRs. As previously shown, exploiting the information across frequency is essential to detect

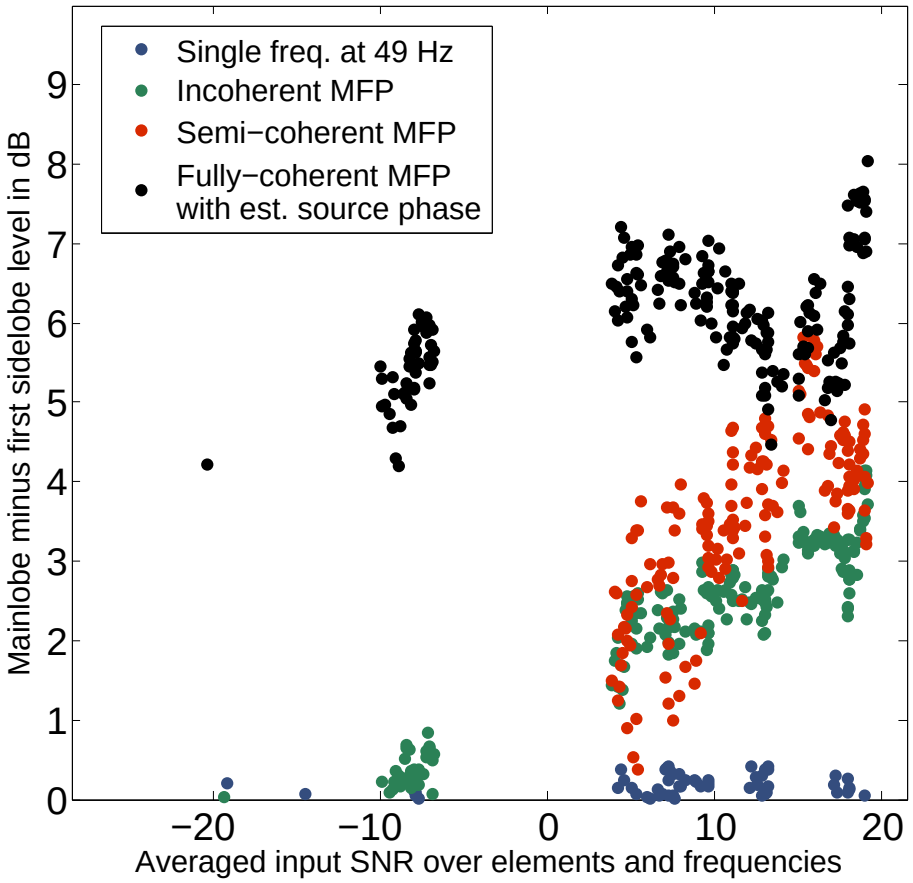

Figure 4.12: Experimental main lobe versus first sidelobe level in dB of the single-frequency at 49 Hz, incoherent, semi-coherent and fully-coherent with estimated source phase matched-field processors as a function of the averaged input SNR over frequencies and elements, using data from the SWellEx-96 experiment. Only the frames localizing the source with an accuracy of 250 m in range and 15 m in depth are displayed.

the source at low input SNR. Three broadband conventional MFP techniques were compared. The first consists in incoherently averaging the information across frequencies, the second, developed by Michalopoulou and Porter, treats the multiple frequencies coherently but removes the unknown source phase information making it a semi-coherent method, and the third is a fully-coherent technique where the source spectrum's phase is incorporated in the processing. The processing gain associated with each method was formally derived, and the semi-coherent processor's performance was shown to approach the fully-coherent one only for very high input SNRs. The detectability of each method versus input SNR was assessed using the detection index performance metric on simulated data. It was shown through theory and simulation that broadband methods were more proficient at detecting a source than single-frequency processing, and that processing the frequencies coherently provided an additional gain in source detectability.

Detection index curves versus SNR were obtained using the SWellEx-96 experiment. The unknown source phase first was estimated from the data using a somewhat exhaustive search procedure. Simulated curves were matched to the experimental ones using colored noise snapshots extracted from the noise part of the data itself. As in the simulated case, the fully-coherent method was shown to perform best at all SNRs, and allow source localization at input SNRs for which the semi-coherent technique failed to localize the source.

4.9 Acknowledgments

This work was funded by ONR. The authors would also like to thank Heechun Song for his helpful comments and discussions.

The text of this chapter is a full reprint of the material of the material soon to be submitted to the J. Acoust. Soc. Am., Claire Debever, William A. Kuperman and William S. Hodgkiss, "Fully coherent matched-field processing using a source phase estimation technique". The dissertation author was the primary researcher and author, and the co-author listed in this publication directed and supervised the research which forms the basis for this chapter.

Bibliography

[1] A. B. Baggeroer, W. A. Kuperman, and H. Schmidt. Matched-field processing: Source localization in correlated noise as an optimum parameter estimation problem. *J. Acoust. Soc. Am.*, 83:571–587, 1988.

[2] N. Booth and P. Schey. Broadband matched-field processing of low level signals in shallow water. *J. Acoust. Soc. Am.*, 97:3291 (A), 1995.

[3] N. O. Booth, P. A. Bacley, J. A. Rice, P. W. Schey, W. S. Hodgkiss, G. L. D'Spain, and J. J. Murray. Source localization with broad-band matched-field procesing in shallow water. *IEEE Journal of Oceanic engineering*, 21(4):402–412, October 1996.

[4] E. K. Westwood. Broadband matched-field source localization. *J. Acoust. Soc. Am.*, 91(5):2777–2789, May 1992.

[5] C. S. Clay and S. Li. Optimum time domain signal transmission and source localization in a waveguide: Matched filter and deconvolution experiments. *J. Acoust. Soc. Am.*, 83:1377–1383, 1988.

[6] C. S. Clay. Optimum time domain signal transmission and source localization in a waveguide. *J. Acoust. Soc. Am.*, 81:660–664, 1987.

[7] S. Li and C. S. Clay. Optimum time domain signal transmission and source localization in a waveguide: Experiments in an ideal wedge waveguide. *J. Acoust. Soc. Am.*, 82:1409–1417, 1987.

[8] S. P. Czenszak and J. L. Krolik. Robust wideband matched-field processing with a short vertical array. *J. Acoust. Soc. Am.*, 101(2):749–759, February 1997.

[9] Z.-H. Michalopoulou and M. B. Porter. Matched-field processing for broad-band source localization. *IEEE Journal of Oceanic engineering*, 21:384–392, 1996.

[10] Z.-H. Michalopoulou. Robust multi-tonal matched-field inversion: A coherent approach. *J. Acoust. Soc. Am.*, 104:163–170, 1998.

[11] R. K. Brienzo and W. S. Hodgkiss. Broadband matched-field processing. *J. Acoust. Soc. Am.*, 94:2821–2831, 1993.

[12] W. S. Hodgkiss and R. K. Brienzo. Broadband source detection and range/depth localization via full-wavefield (matched-field) processing. *Proc. ICASSP-90*, (2743-2747), April 1990.

[13] L. N. Frazer and P. I. Pecholcs. Single-hydrophone localization. *J. Acoust. Soc. Am.*, 88:995–1002, 1990.

[14] P. Hursky, M. B. Porter, and M. Siderius. High frequency (8-16 hz) model-base source localization. *J. Acoust. Soc. Am.*, 115:3021–3032, 2004.

[15] J. L. Krolik. Matched-field minimum variance beamforming in a random ocean channel. *J. Acoust. Soc. Am.*, 92:1408–1419, 1992.

[16] Claire Debever and W. A. Kuperman. Robust matched-field processing using a coherent broadband white noise constraint processor. *J. Acoust. Soc. Am.*, 122 (4):1979–1986, October 2007.

[17] G. J. Orris, M. Nicholas, and J. S. Perkins. The matched-phase coherent multi-frequency matched-field processor. *J. Acoust. Soc. Am.*, 107(5):2563–2575, 2000.

[18] H. L. Van Trees. *Detection, Estimation and Modulation Theory*, volume Part III. John Wiley Sons, 1971.

[19] S. M. Kay. *Fundamentals of Statistical Signal Processing:Vol II Detection Theory*. Prentice Hall, January 1998.

[20] R. J. Urick. *Principles of Underwater Sound*. p 106. McGraw-Hill, New-York, 1983.

[21] R. O. Nielsen. *Sonar signal processing*. Artech House, 1991.

[22] N. O. Booth, A. R. Abawi, P. W. Schey, and W. S. Hodgkiss. Detectability of low-level broad-band signals using adaptive matched-field processing with vertical aperture arrays. *IEEE Journal of Oceanic engineering*, 25(3):296–313, July 2000.

[23] M. B. Porter. The kraken normal mode program (sm245). *SACLANT Undersea Research Center, La Spezia, Italy*, 1991.

[24] F. B. Jensen, W. A. Kuperman, M. B. Porter, and H. Schmidt. *Computational ocean acoustics*, volume chapter 10. Modern Acoustics and Signal Processing, edition 2 edition, 2010.

Chapter 5

Mitigating the effect of environmental fluctuations on higher frequency matched-field processing

5.1 Abstract

Matched-field processing is typically problematic in the kHz frequency regime. Higher frequencies require an accurate, finely sampled knowledge of the environmental parameters involved in the signal's propagation model. The design of a processor robust to sound speed fluctuations is investigated using 3.5 kHz data to construct both the cross-spectral density matrices and the weight vectors. Conventional, minimum variance distortionless response and white-noise constraint weight vectors are produced as a function of time measured around the cross-spectral density matrix construction time. If source and receiver arrays are assumed motionless, the only parameter changing over the course of the experiment is the water channel sound speed. Therefore a comparison of each processors' sensitivity to fluctuations can be performed. Broadband and principal component methods are investigated to increase MFP's robustness to environmental uncertainties. The results obtained using data-derived weight vectors are applied to the traditional model-based matched-field techniques in an effort to successfully locate the source at high-frequency.

5.2 Introduction

Matched-field processing (MFP) techniques provide range/depth localization of acoustic sources and/or information on the propagating media itself by correlating or "matching" the data received on an array to modeled pressure fields coming from an hypothetical source position [1, 2]. While simple in concept, successful source tracking requires the use of an adequate propagation model along with the knowledge of acoustical environmental parameters of interest, and a source signal sufficiently loud to be detected over the noise. Because low-frequency signals are usually minimally affected by model inaccuracies, matched-field processing (MFP) has been successfully applied experimentally to locate a source in range and depth, despite a somewhat simplified knowledge of the propagating environment [3, 4, 5]. Higher frequency MFP on the order of the kHz, however, is much less forgiving to model mismatch and requires a detailed characterization of the en-

vironmental parameters involved in the generation of synthetic fields. Indeed, a 100 Hz signal will be sensitive to features roughly the size of its fifteen meters wavelength, while a 3500 Hz signal will be affected by changes on the order of half a meter. For the same reason, sound speed fluctuations are problematic and usually prevent adequate reproduction of the measured pressure field. While the ultimate MFP's goal is the characterization of the source range and depth, on a practical standpoint however, the ability to differentiate between submerged and non-submerged targets, along with an estimate of the distance between the source and receivers is already an important achievement.

Recently, *et al* [6] investigated the performance of time domain MFP at high frequency (above 1 kHz). They showed that tracking the source successfully required averaging successive experimental impulse responses, using the envelope of the data (discarding the phase information) and articially increasing the bandwidth of the synthetic signal to minimize the effect of mismatch. Soares *et al* [7] experimentally localized a source transmitting a 800 to 1500 Hz broadband signal up to 10 km away from the receivers, using frequency domain MFP. However, this required prior estimation of the environmental parameters giving the best fit between received data and modeled replicas using a genetic algorithm optimization procedure.

Single-frequency literature provides a class of matched-field processors designed to increase the signal's detectability and/or robustness to model inaccuracies. Adaptive methods involve a constrained optimization problem and are often preferred to conventional ones because of the higher resolution ensued, better peak-to-background levels and cancellation of potential interferers. However, such techniques as the minimum variance distortionless response (MVDR) are extremely sensitive to environmental mismatch[3, 8, 9]. A considerable amount of work has been done to mitigate the sensitivity of matched-field adaptive processors to modeling errors [9, 10, 11, 12, 13]. These adaptive methods were shown to be efficient in localizing sources in challenging environments and robust to presence of environmental mismatch. On the other hand, they are more computationally intensive and require a threshold SNR under which the output isn't improved over

conventional methods[14].

High-frequency tracking ability of the conventional, minimum variance and white-noise constraint methods [13] will be investigated in this paper.

Localization performance can also be enhanced by implementing broadband as opposed to narrowband processing. Indeed, broadband methods take advantage of the temporal complexity of the signal and therefore offer an additional gain over single-frequency processing by augmenting the dimension of the data space.

There typically are two ways to combine information across frequency.

1. One can do an incoherent broadband type of processing [14, 15, 16], where single frequency power outputs are averaged linearly or in dB in an effort to lower the sidelobes and increase the robustness of MFP to environmental uncertainties. The sum increases the detectability of the signal and robustness to mismatch when the environmental uncertainties cause a frequency-independent shift of the main lobe as opposed to the sidelobes.

2. Or one can exploit the cross-frequency complex information enlarging the data space and providing an extra-processing gain, with the drawback that these processors have to deal with the typically unknown complex spectral properties of the signal sent.

Broadband coherent matched-field processing was first developed in the time domain [17, 18, 19]. Since adaptive MFP methods operate in the frequency domain, coherent processors involving discrete frequencies are of particular interest. Westwood [20] developed an algorithm matching cross correlated measured impulse responses between pairs of receivers against modeled ones, the resulting complex function being summed coherently over frequencies. The unknown source phases cancel out by design. The information coming from auto-spectra, or in other words the diagonal terms of the single frequencies cross-spectral density matrix (CSDM) was discarded, because potentially overpowering the off-diagonal complex entries without contributing positively to the localization. The method was applied successfully to a shallow water experimental data set characterized by strong multipath. Czenszak and Krolik [21], on the other hand kept the auto-spectra information and formulated the algorithm in a quadratic form similar to

single frequency MFP. A previously developed adaptive method, the environmental perturbation constraint method [11], was applied to mitigate the higher sensitivity to mismatch obtained from the increased number of degrees of freedom.

Michalopoulou and Porter [22, 23] introduced a coherent algorithm based on matching received and modeled fields rather than cross-correlated pair sof fields. It is chosen in this paper because its formulation builds on standard single frequency algorithms. Since the unknown source phases across frequency do not cancel out anymore, the authors resorted to a normalization and cancellation scheme to remove the source amplitudes and phases. The resulting processor is therefore better described as semi-coherent. The method tested on a real data set was shown to significantly improve the minimum variance distortionless response (MVDR) tracking accuracy in comparison to incoherent broadband techniques. Debever and Kuperman [24] combined it with the adaptive white noise constraint algorithm to enhance its robustness to environmental mismatch and snapshot deficiency.

This paper evaluates the extent of high-frequency MFP's sensitivity to environmental variability and explores the possibility of designing a robust processor in the frequency domain, able to locate the source experimentally without use of a focalization technique. The issue is whether simplified range and time independent environmental models can be sophisticated enough to reproduce the received signal somewhat accurately. In Sec. 5.3, we first provide MFP tracking results obtained using a single-frequency conventional processor on two high-frequency data sets, the Focused-Acoustic Field (FAF) experiments 2003 and 2005. Because reproducing an accurate ocean channel to construct synthetic fields is problematic at such frequencies, 3.5 kHz data is used to construct both the cross-spectral density matrices and the weight vectors in Sec. 5.4. This way, model mismatch is nonexistent, and assuming source and receiver arrays motionless, the only variability comes from the water channel sound speed. The robustness of conventional, minimum variance and white noise constraint methods for the single-frequency, broadband incoherent and broadband semi-coherent cases is investigated in absence of mismatch, but presence of sound speed fluctuations. A singular value decomposition method is also introduced in the construction of the "data weight

vector" in an effort to further mitigate the effect of fluctuations. Sec. 5.5 builds on the mismatch-free results of Sec. 5.4 to improve model-based MFP in high-frequency scenarios. Finally, Sec. 5.6 provides a summary and discussion.

5.3 Narrowband conventional matched-field processing at high frequency

High frequency sources on the order of a kHz or more are notoriously hard to locate accurately because of the temporal and spatial variability of the environment [25, 26, 7]. Data from two experiments conducted in 2003 and 2005 North of Elba Island, the Focused Acoustic Field (FAF) 03 and 05 are processed to illustrate the effect of oceanic variability on the localization's performance of narrowband conventional MFP.

5.3.1 The FAF 03 experiment

The FAF 03 experiment was conducted in 2003 by the SACLANT Undersea Research Centre and the Marine Physical Laboratory, Scripps Institution of Oceanography North of Elba Island, Italy [27]. A series of 3.5 kHz chirps with 1.4 kHz bandwidth were sent successively by each of the 29 sources deployed in a vertical array (SRA). The emitted signals were recorded on a 32-element vertical receiver (VLA) array located 1.3 km away from the source array. The VLA spanned the water column between 32 m and 98.2 m by increments of 2 m, and the SRA between 23.4 m and 101.8 m by increments of 2.7 m. The water depth was 110 m, and the bathymetry and deployment setup is schematized in Fig. (5.1). Conductivity-temperature-depth (CTD) measurements were performed over the course of the experiment. Sound speed variability obtained in a 14 hour window around the data recording time is represented on Fig. (5.2). The biggest fluctuations (+/- 2m/s) were found in the first 15 m of the water column, the rest of the water column exhibiting +/- 0.5 m/s at most. The mean sound speed profile obtained is chosen to model the pressure field using the KRAKEN normal mode

package [28].

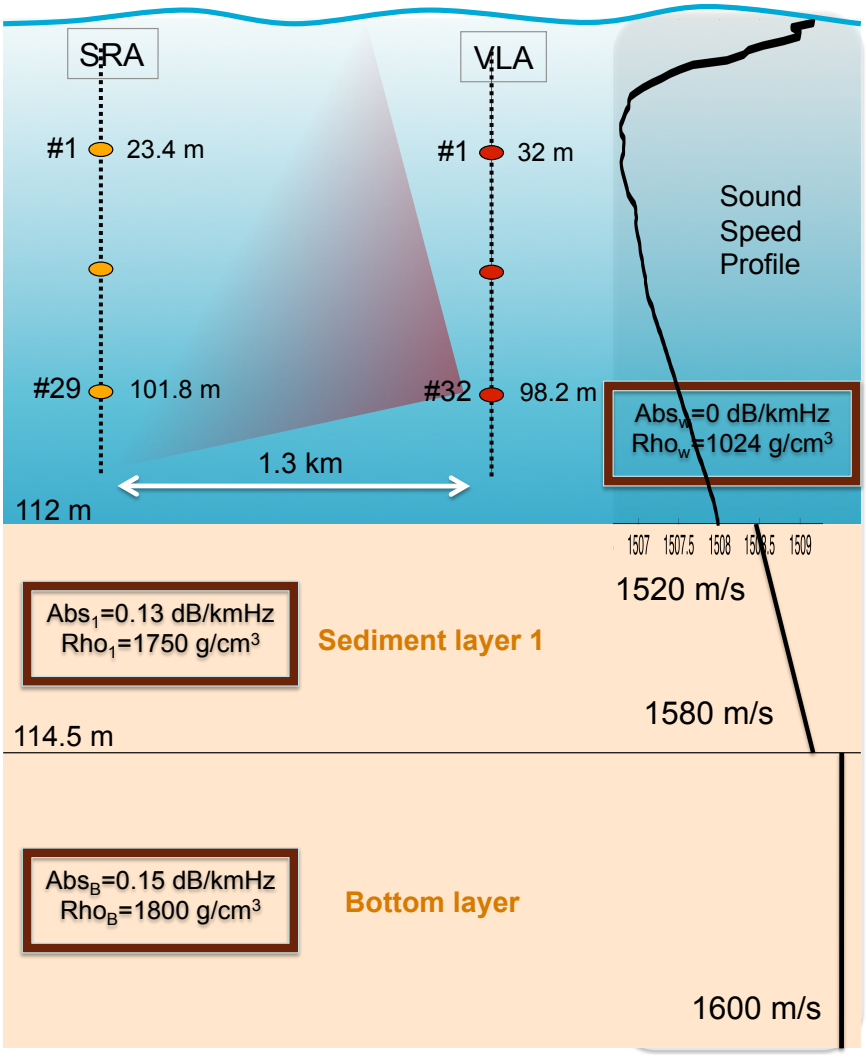

Figure 5.1: The FAF 03 environment, featuring a 29-element source line array (SRA) and 32-element receiver line array (VLA) about 1.3 km appart.

Let $x_\omega^{(i)}$ denote the complex field received on the hydrophone i at angular

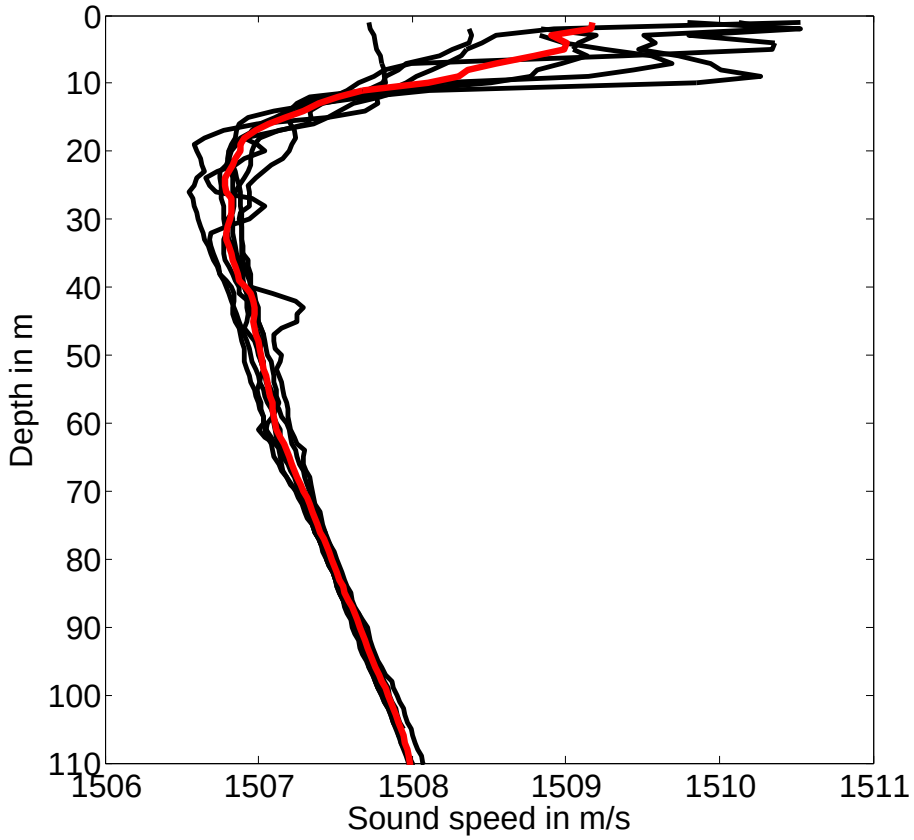

Figure 5.2: Sound speed variability over 14 hours during the FAF 03 experiment obtained from conductivity-temperature-depth (CTD) casts.

frequency ω from a source at (R_s, Z_s) .

$$x_\omega^{(i)} = S(\omega)G^{(i)}(0, z_i, R_s, Z_s, \omega) + Q^{(i)}(\omega), \tag{5.1}$$

where $S(\omega)$ is the frequency dependent complex source spectrum, the expression $G^{(i)}(0, z_i, R_s, Z_s, \omega)$ the ocean waveguide's Green's function between the source location and the element i of the receiving array, and $Q^i(\omega)$ the complex noise component corrupting the signal.

Matched-field processing is essentially performing a sum of correlations between modeled and measured fields over elements. Typically, the complex field received on each hydrophone at one frequency is stacked in a (Nx1) vector, N being the number of elements in the array:

$$\boldsymbol{x_\omega} = \left[\; x_\omega^{(1)}, x_\omega^{(2)}, \ldots, x_\omega^{(N)} \; \right]^T, \tag{5.2}$$

where the notation ^{T} denotes the transpose operator. A modeled field on the array from a hypothetical source at (r, z) can be written in a (Nx1) vector as well, commonly called the replica vector, or weight vector $\boldsymbol{w}_\omega$.

The narrowband matched-field processor output is the correlation between received and modeled fields at various possible source positions along a grid in range and depth,

$$B\left(r, z\right) = \boldsymbol{w}_\omega^H\left(r, z\right) \boldsymbol{R}_\omega \boldsymbol{w}_\omega\left(r, z\right), \tag{5.3}$$

where $\boldsymbol{R}_\omega = E\{\boldsymbol{x}_\omega \boldsymbol{x}_\omega^H\}$ is the cross-spectral density matrix (CSDM) at angular frequency ω and the superscript H refers to the Hermitian transpose operation. In the conventional matched-field processor case, the weight vector is just the normalized Green's function

$$\boldsymbol{w}_\omega = \boldsymbol{d}_\omega = \frac{1}{\sqrt{\left(G_\omega^{(1)}\right)^2 + \ldots + \left(G_\omega^{(N)}\right)^2}} \left[\; G_\omega^{(1)}, \ldots, G_\omega^{(N)} \; \right]^T. \tag{5.4}$$

The narrowband conventional matched-field processor is implemented using the center frequency 3505 Hz and one data snapshot only to form the CSDM. As seen on Fig. (5.3), the source 29 is successfully localized in range and depth despite using a simple range/time independent environment and a single frequency.

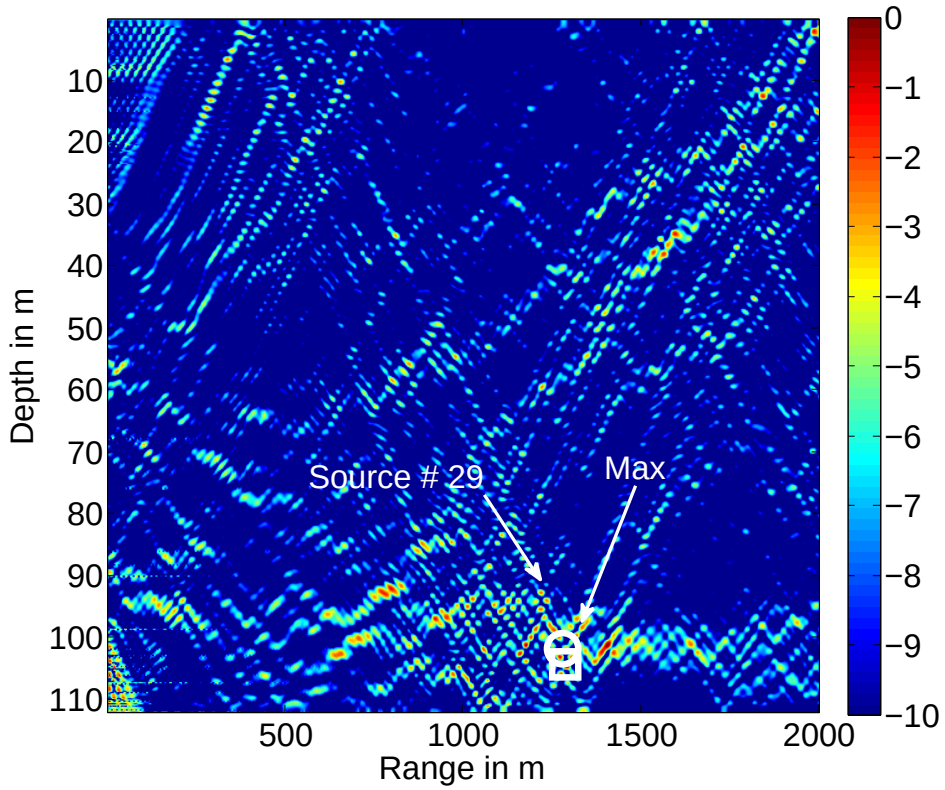

Figure 5.3: Narrowband conventional MFP output at 3505 Hz. The circle represent the position of the source, and the square the position of the conventional algorithm's maximum. The source 29 is correctly localized despite using a simple range/time independent environment and a single frequency.

Higher frequency MFP seem practical when the source array is relatively close to the receiver array (around 1 km). However, a study of the evolution of the MFP's localization performance over time would be necessary to confirm this hypothesis. Also, the question of whether MFP's performance would degrade at larger ranges is of importance, and the main motivation to apply MFP to the FAF 05 data set.

5.3.2 The FAF 05 experiment

The FAF 05 experiment was conducted two years later around the same location, with a comparable experimental setup but this time the distance between the source and receiver arrays was increased to 4 km [29]. The receiver vertical line array (VLA) spanned the water column between 34 m and 112.6 m by increments of 2.5 m and the source vertical line array (SRA) between 48 m and 110 m by increments of 2.1 m. A series of 3.5 kHz chirps with 1 kHz bandwidth were sent successively by each of the 29 sources with a 200 ms channel to channel delay. The process was repeated every 20 s. This time, the signal was recorded over 9 hours, allowing the environment to change during the scope of the experiment. Figure (5.4) shows a schematic representation of the experimental environment. As in FAF 03, CTD measurements were performed over the course of the experiment. Sound speed variability obtained in a 14 hour window around the data recording time is represented on Fig. (5.5), as well as the output of a CTD chain over 70 min. The largest fluctuations of about +/- 5 m/s happened around the 40 m deep thermocline.

Note that the sound speed profile's shape changed considerably between the FAF 03 and FAF 05 experiment, and the FAF 05' s conditions exhibit the presence of a sub channel in the first 40 m of the water column. Fig. (5.6) displays the spread of arrival of each mode on the array, evaluated from the minimum and maximum group speeds associated with each mode. It reveals that in FAF 03, the lowest modes arrive first, while in FAF 05 the first arrivals are modes 54 to 100, who travel predominantly through the surface sub-channel. Modes 1 to 53 are delayed by 20 ms. The sound propagation process is therefore more complex

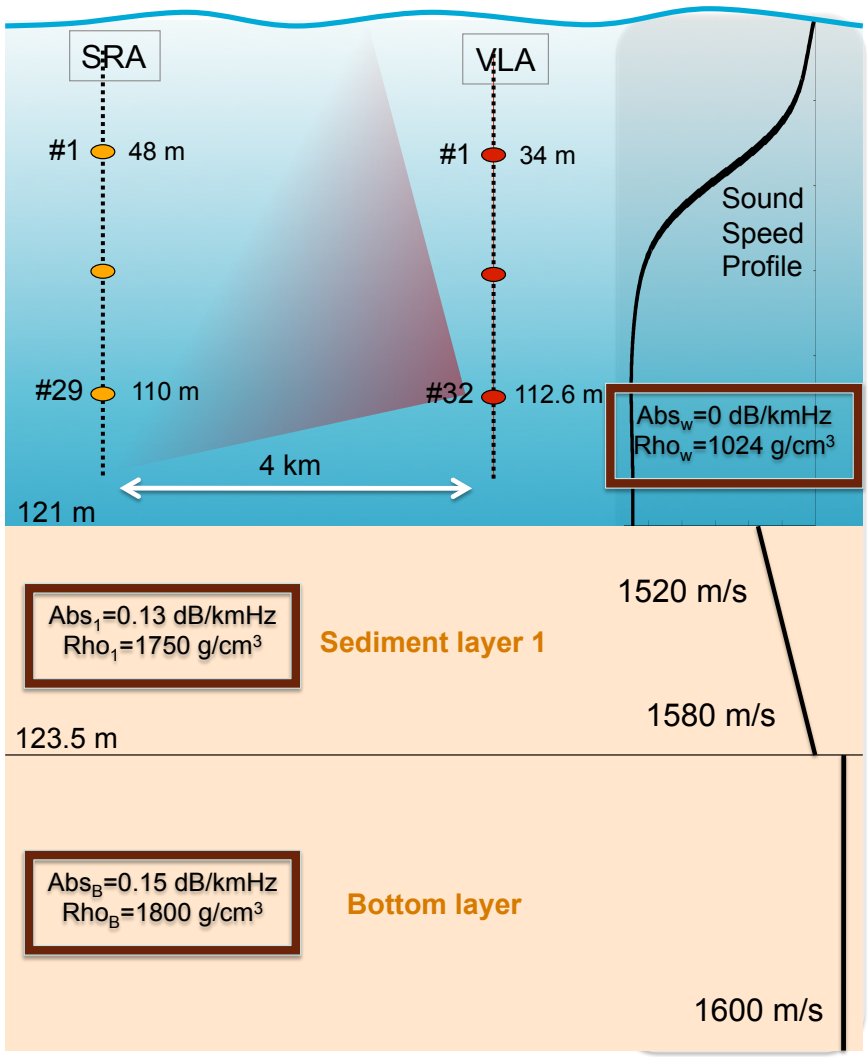

Figure 5.4: The FAF 05 environment, featuring a 29-element source line array (SRA) and 32-element receiver line array (VLA) about 4 km appart.

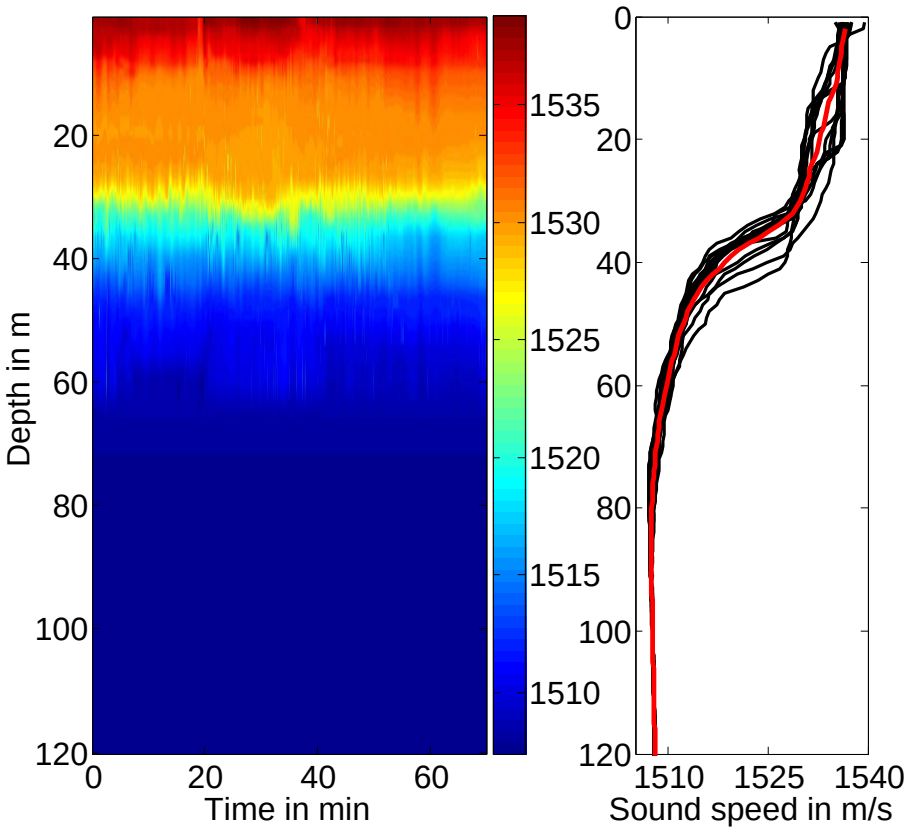

Figure 5.5: Sound speed variability over 14 hours during the FAF 05 experiment obtained from conductivity-temperature-depth (CTD) casts.

in FAF 05 medium than in FAF 03.

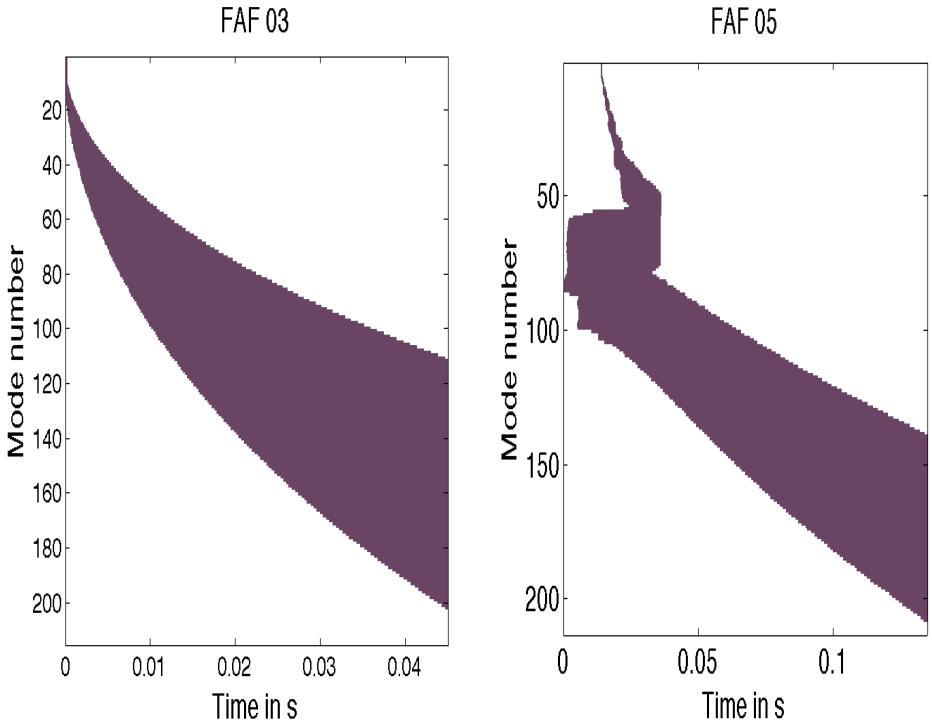

Figure 5.6: Modal spread of arrival on the array for the FAF 03 and FAF 05 experiments in s.

As done with FAF 03 experiment, the narrowband conventional matched-field processor is implemented using the center frequency 3505 Hz and one data snapshot only to form the CSDM. This time, as seen on Fig. (5.7), the source 29 is incorrectly localized. Increasing the source-receiver distance from 1.3 km to 4 km is enough to destruct the match between synthesized and received fields. Larger propagation distance scenarios are more sensitive to environmental uncertainties than shorter range ones.

Since each source sent a chirp every 20 s, successive recordings can be processed to study the narrowband 3.505 KHz conventional matched-field processor's tracking performance over a 6 hour-long time window. For each frame, the ambiguity surface is computed and the position of the maximum determined. Figures (5.8) (a) and (b) represent the depth and range slices obtained at the main-lobe

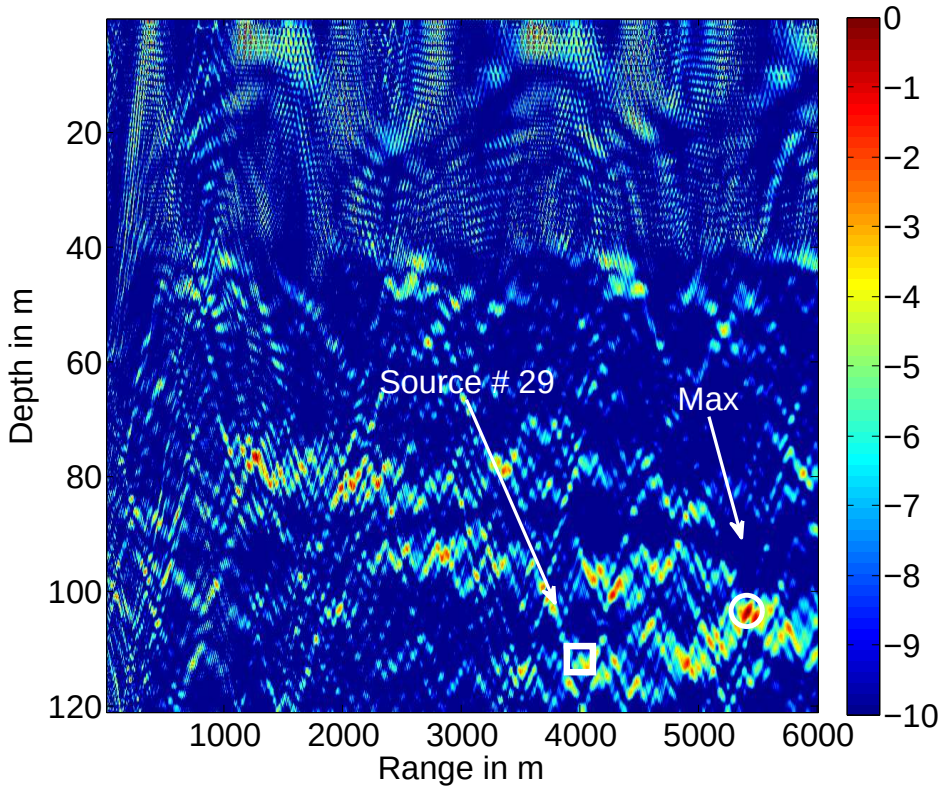

Figure 5.7: Narrowband conventional MFP output at 3505 Hz. The circle represent the position of the source, and the square the position of the conventional algorithm's maximum. The source 29 is incorrectly localized due to the increase in source-receiver distance rendering the algorithm more sensitive to model mismatch.

position as a function of time. The position of the source 29 is represented by the arrows, at 112 m deep and 4 km in range. The single-frequency conventional processor does not localize the source at all, not counting the two successful frames around the five hour mark.

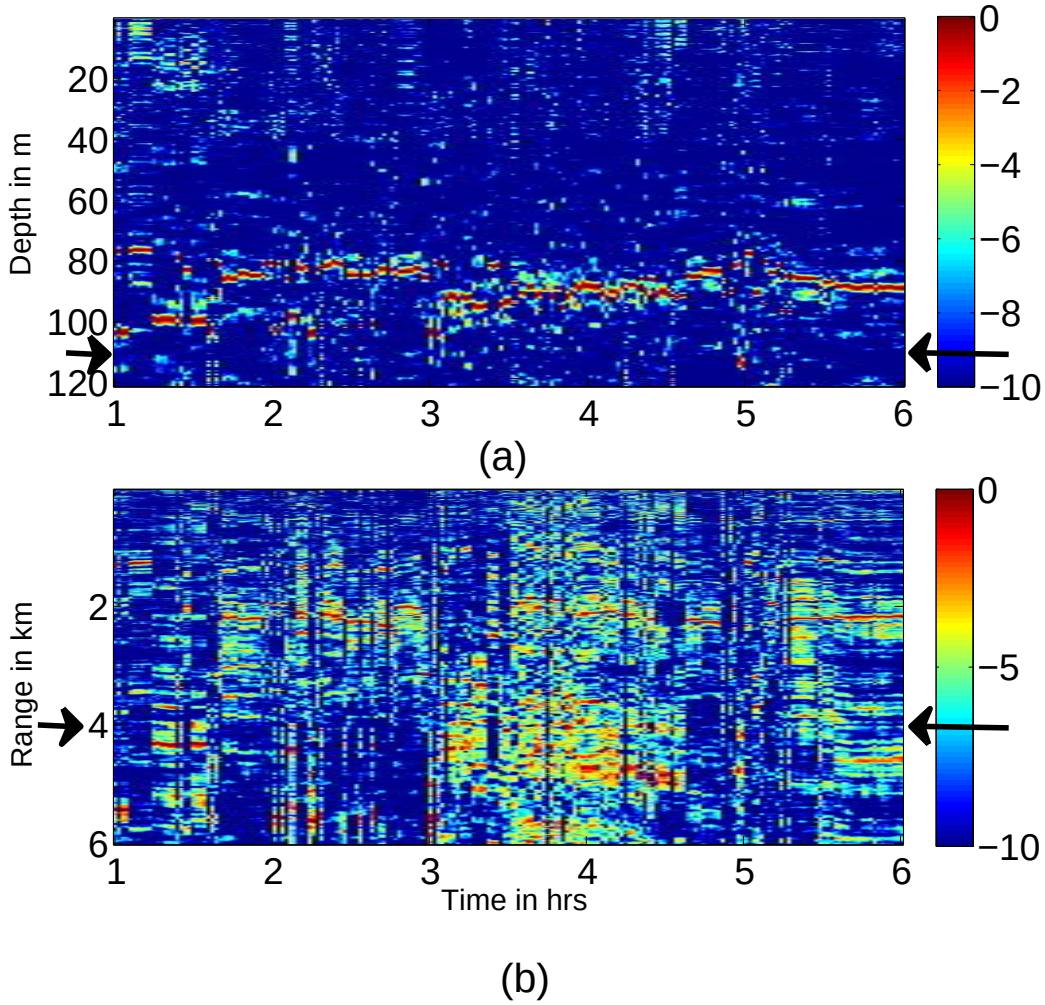

Figure 5.8: Narrowband conventional MFP's variability over 6 hours from successive recordings of chirps sent by the source 29 every 20 s. (a) and (b) represent the depth and range slices respectively obtained at the main lobe's position as time evolved. The position of the source at 112 m deep and 4 km in range is given by the arrows. Environmental uncertainties prevent the single-frequency conventional method from localizing the source.

The issue is to know whether a range and time independent model is just too simplified to give a good localization result at such ranges and frequencies, or if it could be sufficient if combined with robust broadband methods and introduction of the sound speed variability in the creation of the replica vector.

5.4 Investigation of MFP's sensitivity using data derived replica vectors

5.4.1 Narrowband results

Since modeling the propagating environment accurately is problematic in the 3.5 kHz regime at 4 km ranges, a study of the processor's sensitivity to sound-speed fluctuations is performed using the data itself to construct the replica vectors. A bank of 1600 recorded transmissions from each of the 29 sources spanning a 9 h time window is available. If we choose the deep source at time t_o to construct a 1-snapshot CSDM, and the recordings at t_o obtained from the other sources to create replica vectors, we can evaluate the mean sidelobe level at t_o. We can also use transmissions from each sources at $t_o + \Delta t$ to create the replica vectors, and get the corresponding mean sidelobe level at $t_o + \Delta t$. Therefore, this method allows us to study the evolution of the mean sidelobe level obtained by different types of processors as a function of time around the CSDM's construction time.

Note the absence of environmental mismatch since the data itself is used to match data at a different time. The only variability in the system comes from the source and receiver arrays' motion and the sound-speed fluctuations. Hence, the results obtained can be considered to be the best-case scenario, for which we could somehow model an accurate range-dependent environment but introduce various levels of sound-speed variability.

Also, the value of the side-lobe level is only available at the position of the sources along the array, which gives a partial picture of the sidelobe level's evolution over time. Nevertheless, it constitutes a great tool to study various algorithm's robustness to environmental fluctuations.

For ease of representation, the mean sidelobe level is evaluated with respect to a 0 dB main lobe. Hence positive values of the sidelobe level mean that the source would be incorrectly localized. Figure (5.9) represents the mean sidelobe level obtained using the the single-frequency (at 3505 Hz) conventional MFP. The horizontal axis represents the time offset between the data used to create the CSDM and the one used to construct the replica vector. The vertical axis represents the CSDM's construction time. The algorithm yields a successful source localization (*ie* sidelobes lowers than - 4 dB) over a 15 min window.

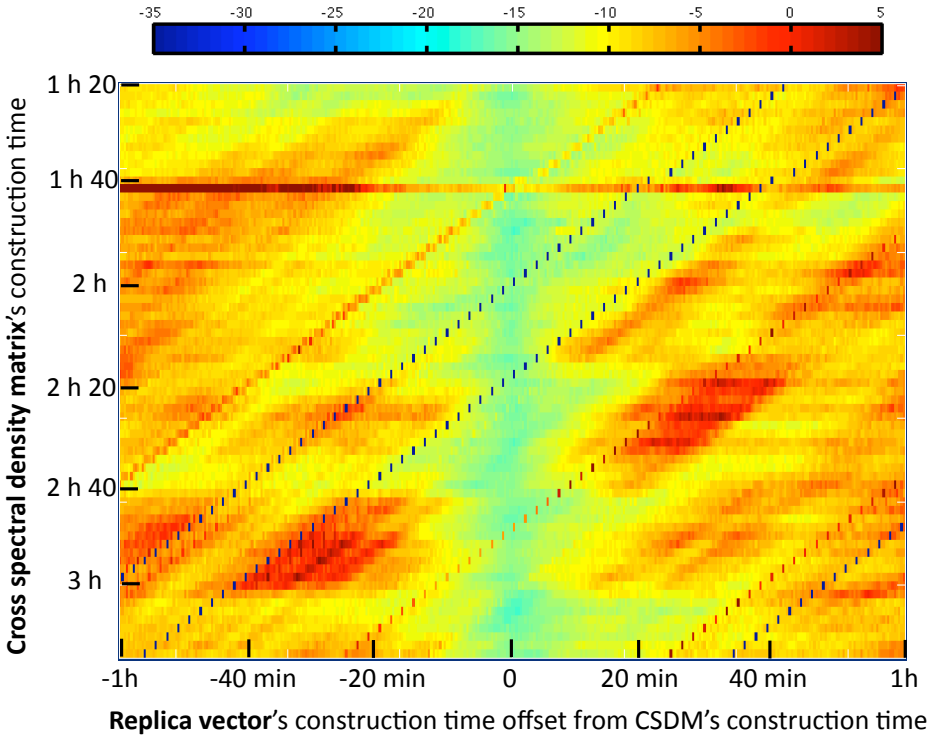

Figure 5.9: Mean sidelobe level in dB obtained with the single frequency conventional MFP at 3505 Hz. The horizontal axis represents the time offset between the data used to create the CSDM and the one used to construct the replica vector. The vertical axis represents the CSDM's construction time.

5.4.2 Broadband results

Four frequencies are now processed (3.1, 3.3, 3.5 and 3.7 KHz) in an effort to increase the conventional algorithm's robustness to fluctuations.

Because the position of the sidelobes is usually frequency dependent as opposed to the main lobe one, a common approach proposed by Baggeroer *et al* is to incoherently average single-frequency ambiguity surfaces to suppress ambiguous sidelobes [14]. The conventional incoherent output can be written as:

$$P_{IC}\left(r,z\right)=\frac{1}{L}\sum_{k=1}^{L}10log\left[\left|\boldsymbol{d}_k^H\boldsymbol{R}_k\boldsymbol{d}_k\right|\right]. \tag{5.5}$$

where L is number of single tones processed.

Coherent broadband processing is also investigated using the algorithm developed by Z-H. Michalopoulou and M. Porter [22, 23].

The narrowband signal vectors are stacked into one "supervector" of length $N \times L$.

$$\breve{\boldsymbol{x}}=\left[\begin{array}{c} x_{\omega_1}^{(1)},x_{\omega_1}^{(2)},\ldots,x_{\omega_1}^{(N)},\ldots,x_{\omega_L}^{(1)},\ldots,x_{\omega_L}^{(N)} \end{array}\right]^T. \tag{5.6}$$

From this supervector, a "super" CSDM can be constructed in the usual way, $\breve{\boldsymbol{R}}=E\{\breve{\boldsymbol{x}}\breve{\boldsymbol{x}}^H\}$. As opposed to incoherent processing, the extended cross spectral density matrix $\breve{\boldsymbol{R}}$ now exploits cross-frequency coherence as well. But because the signal sent by the source has a characteristic signature in frequency represented by the complex term $S(\omega)$ in Equation 5.1, the modeled field is now mismatched with respect to the signal. To be fully-coherent, the processor has to first remove the phases of those complex terms for each frequency of the signal received.

$$\breve{\boldsymbol{x}}=\left[\begin{array}{c} x_{\omega_1}^{(1)}e^{-jarg(S(\omega_1))},\ldots,x_{\omega_L}^{(N)}e^{-jarg(S(\omega_L))} \end{array}\right]^T. \tag{5.7}$$

The conventional MFP processor output can then be formulated as:

$$P_{Coh}\left(r,z\right)=\breve{\boldsymbol{d}}^H\breve{\boldsymbol{R}}\breve{\boldsymbol{d}},$$

$$P_{Coh}\left(r,z\right)=E\left[\left|\sum_{k=1}^{L}\boldsymbol{d}_k^H\boldsymbol{x}_ke^{-jarg(S(k))}\right|^2\right]. \tag{5.8}$$

where FC stands for fully-coherent.

In practice, the complex source spectrum is unknown, leaving the user with replicas mismatched with respect to the signal. Michalopoulou and Porter addressed this issue by scaling the phase of each single-frequency subvector $\boldsymbol{x}_k$ by the phase on the phone displaying the highest SNR, and normalizing the subvector to unit length [22, 23]. This compensation procedure effectively eliminates the unknown source terms in high SNR scenarios, but introduces the extra phase of the phone chosen to calibrate the other elements in the process. The algorithm is therefore semi-coherent.

If we denote the new subvector by $\overline{\boldsymbol{x}}_{\boldsymbol{k}}$ and assume no contamination by noise and the first phone having the highest SNR:

$$\boldsymbol{x}_k = \begin{bmatrix} \left|S(k)G^{(1)}(k)\right| e^{j\left[arg(S(k))+arg(G^{(1)}(k))\right]} \\ \vdots \\ \left|S(k)G^{(N)}(k)\right| e^{j\left[arg(S(k))+arg(G^{(N)}(k))\right]} \end{bmatrix},$$

we have,

$$\overline{\boldsymbol{x}}_{\boldsymbol{k}} = \frac{1}{\alpha} \begin{bmatrix} \left|G^{(1)}(k)\right| e^{j0} \\ \vdots \\ \left|G^{(N)}(k)\right| e^{j\left[arg(G^{(N)}(k)-arg(G^{(1)}(k))\right]} \end{bmatrix}, \tag{5.9}$$

where $\alpha = \sqrt{|G^{(1)}(k)|^2 + \ldots + |G^{(N)}(k)|^2}$ is a coefficient of normalization.

Figures (5.10) and (5.11) represent the mean sidelobe level obtained using the the incoherent and coherent broadband conventional MFP respectively.

Applying a broadband type of processor, especially the coherent one increases the contrast of the output. Localization is good in a 15 minute-long window around the CSDM's construction time, and features lower mean sidelobe levels than obtained using narrowband or incoherent processing (-17 dB for the single frequency and incoherent broadband outputs and -20 dB for the incoherent and coherent broadband algorithms). However, the mean sidelobe level is bigger outside of the window, and the coherent broadband method isn't robust to fluctuations occurring over a longer period of time than the narrowband method.

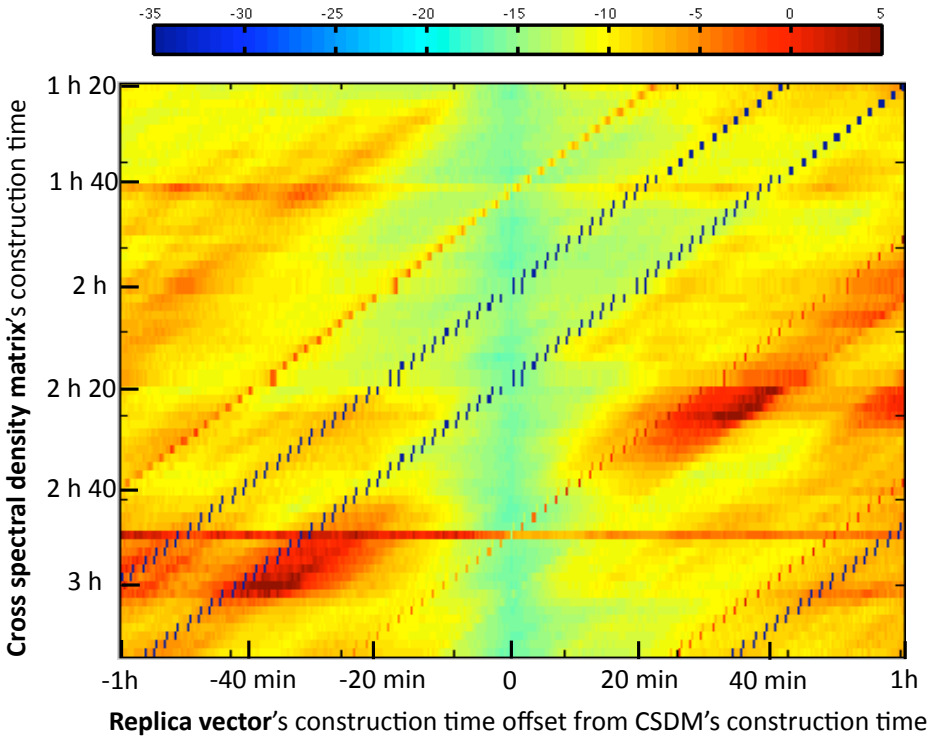

Figure 5.10: Mean sidelobe level in dB obtained with the incoherent broadband conventional MFP at 3.1, 3.3, 3.5 and 3.7 KHz. The x-axis represents the time offset between the data used to create the CSDM and the one used to construct the replica vector. The y-axis represents the CSDM's construction time.

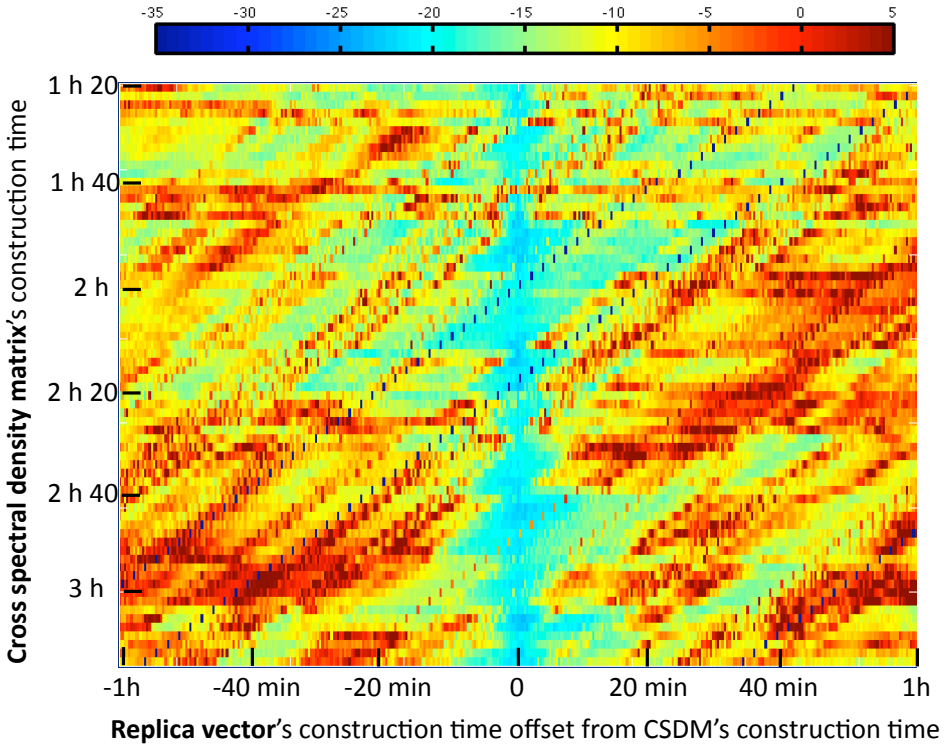

Figure 5.11: Mean sidelobe level in dB obtained with the coherent broadband conventional MFP at 3.1, 3.3, 3.5 and 3.7 KHz. The horizontal axis represents the time offset between the data used to create the CSDM and the one used to construct the replica vector. The vertical axis represents the CSDM's construction time.

5.4.3 Application of the singular value decomposition over environments

In an effort to increase robustness to sound speed fluctuations in the medium, a matrix is formed with replicas vectors obtained from continuous recordings as column vectors. A singular value decomposition (SVD) of the replica matrix is performed and the resulting singular vector corresponding to the highest singular value, herein referred as the "first singular vector" is kept as the new replica vector. Indeed, performing a singular value decomposition extracts the most stable features of the columns or lines of a matrix. The first singular vector is therefore representative of the set of replicas over the time window considered and likely to be more robust to fluctuations occurring over that time period.

This method is related to the minimum variance environmental perturbation constraint technique developed by Krolik [11], where a set of linear constraints is applied to modeled fields obtained from randomly perturbed environments. The main difference with what is proposed here is the type of algorithm applied to the environmentally averaged replicas. Krolik used a multiple constraint method, while this paper investigates the conventional, minimum variance and white noise constraint algorithms.

To understand the effect of using the SVD technique on the conventional MFP's robustness to sound speed variability, replica matrices encompassing an increasingly larger number of replica vectors from continuous recordings are formed, decomposed into singular values and vectors, and the first singular vector obtained is matched to the data used to create the CSDM. Note that the CSDM is constructed using the data at the center of the ensemble of consecutive replicas, so that the environment has not drastically changed from the CSDM's construction time to the multiple replica times. However, the actual chirp recording used to create the CSDM is removed from the replica matrix to avoid any effect due to matching the data by its exact self. The format of the figures presented in previous sub-sections 5.4.1 and 5.4.2 is modified such that the horizontal axis represents the width of the replica matrix centered on the CSDM's construction time. For instance, an x-value of $\pm$ 20 min means that the first singular vector of a replica

matrix composed of successive transmissions received 20 minutes on either side of the CSDM's construction time (minus the center one used to create the CSDM) is matched to the CSDM.

Figures (5.12), (5.13) and (5.14) represent the mean sidelobe levels obtained by combining SVD to single-frequency, incoherent and coherent broadband conventional algorithms. A comparison with Figs. (5.9), (5.10) and (5.11) show that the SVD technique did increase considerably the conventional method's robustness to sound-speed variability. The main-lobe is at the right position for most of the whole hour window as opposed to 15 minutes only on either side of the CSDM's construction time. As mentioned in the last section, broadband/SVD yields lower mean sidelobe levels than the narrowband/SVD method.

5.4.4 Adaptive methods results

The previous subsections showed that applying a singular value decomposition over changing environments efficiently stabilized the conventional replica vector with respect to sound speed fluctuations, and that broadband processing further lowered the mean sidelobe level obtained. In this subsection, we would like to investigate the robustness of the minimum variance distortionless response [30, 1] (MVDR) and white noise constraint adaptive methods [13] (WNCM).

The MVDR weight vector is determined by solving

$$\min_{\boldsymbol{w}} \boldsymbol{w}^H \boldsymbol{R} \boldsymbol{w} \quad \textit{subject to } \boldsymbol{w}^H \boldsymbol{d} = 1, \tag{5.10}$$

where $\boldsymbol{d}$ is the conventional weight vector at (r, z).

This optimization problem can be interpreted as a filter which passes the look direction signal undistorted while rejecting noise and interferers.

Using the method of the Lagrange multiplier, we obtain the well known solution:

$$\boldsymbol{w}_{\boldsymbol{mvdr}} = \frac{\boldsymbol{R}^{-1}\boldsymbol{d}}{\boldsymbol{d}^H \boldsymbol{R}^{-1} \boldsymbol{d}}. \tag{5.11}$$

and the MVDR power output is:

$$\boldsymbol{P}_{\boldsymbol{mvdr}}(r, z) = \frac{1}{\boldsymbol{d}(r, z)^H \boldsymbol{R}^{-1} \boldsymbol{d}(r, z)}. \tag{5.12}$$

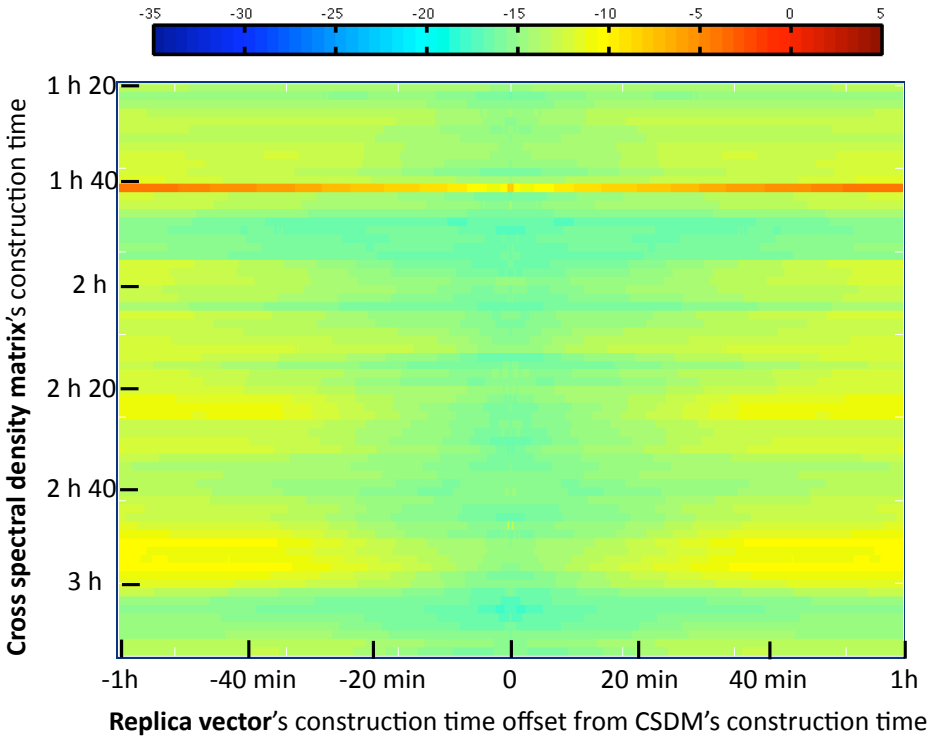

Figure 5.12: Mean sidelobe level in dB obtained with the singular-value-derived single frequency conventional MFP at 3.5 KHz. The horizontal axis represents the time offset between the data used to create the CSDM and the one used to construct the replica vector. The vertical axis represents the CSDM's construction time.

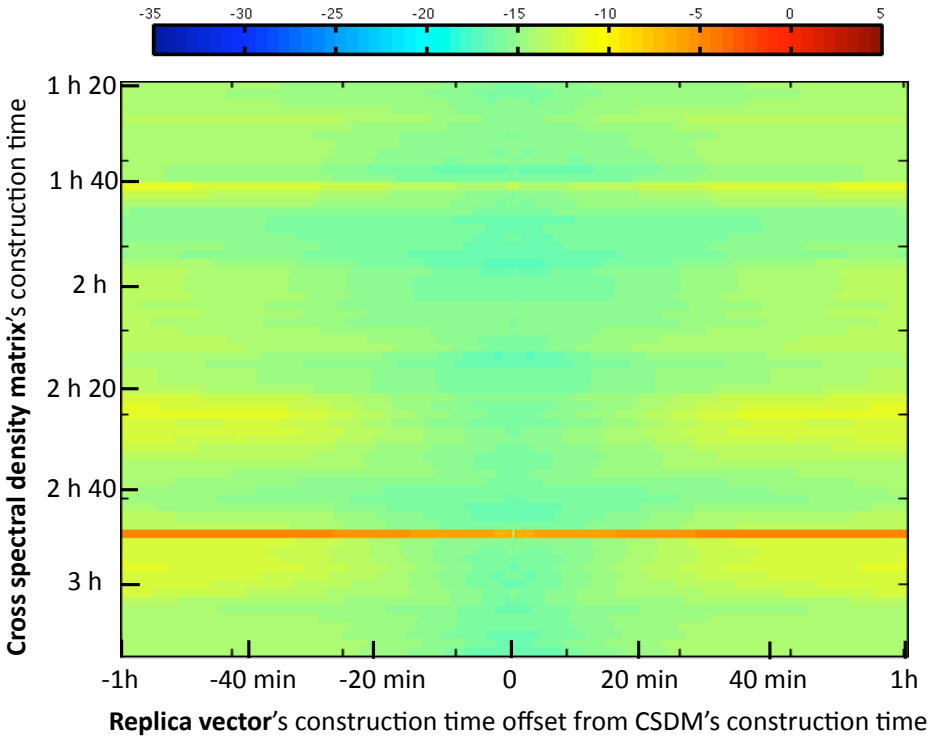

Figure 5.13: Mean sidelobe level in dB obtained with the singular-value-derived incoherent broadband frequency conventional MFP at 3.1, 3.3, 3.5 and 3.7 KHz. The horizontal axis represents the time offset between the data used to create the CSDM and the one used to construct the replica vector. The vertical axis represents the CSDM's construction time.

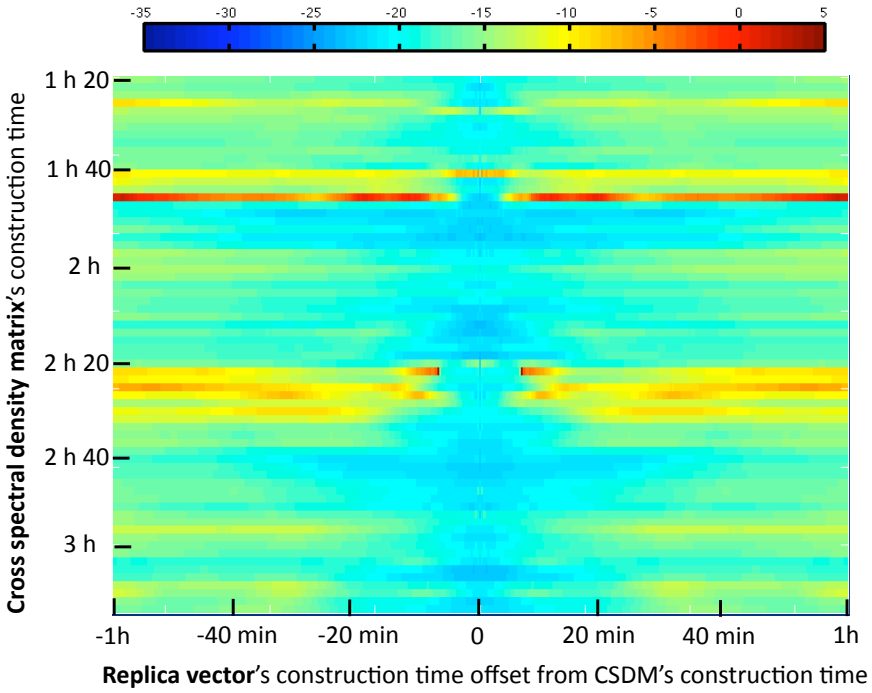

Figure 5.14: Mean sidelobe level in dB obtained with the singular-value-derived coherent broadband frequency conventional MFP at 3.1, 3.3, 3.5 and 3.7 KHz. The horizontal axis represents the width of the replica matrix centered on the CSDM's construction time. The vertical axis represents the index of the received signal used to create the CSDM.

This algorithm enhances the resolution considerably in comparison to the conventional processor, however this exceptional resolution capability comes with an increased sensitivity to slight mismatch between the modeled and actual environment [3, 9, 8].

Figure (5.15) represents the mean sidelobe level obtained using the narrowband, incoherent and coherent broadband MVDR processors. As expected, the MVDR algorithm is extremely sensitive to mismatch. Narrowband MVDR is problematic as soon as the ocean channel changes, while broadband MVDR remains stable over a 5 minutes-long time window.

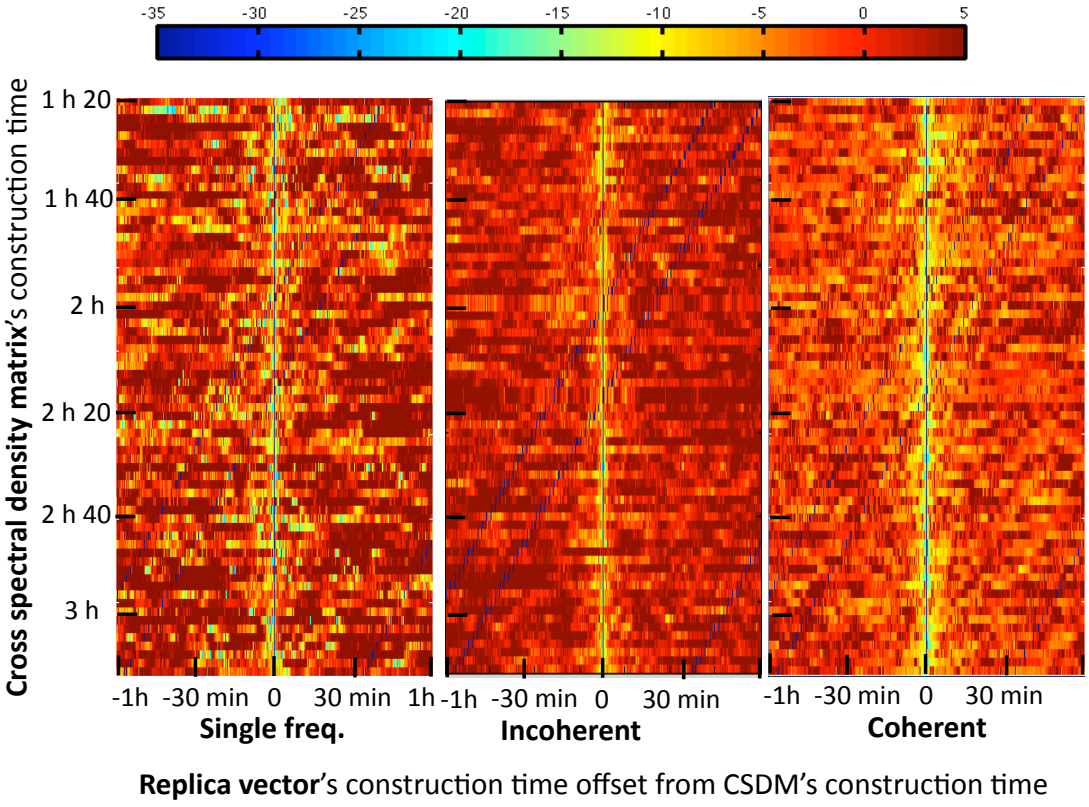

Figure 5.15: Mean sidelobe level in dB obtained with the narrowband, incoherent and coherent broadband MVDR processors. The horizontal axis represents the width of the replica matrix centered on the CSDM's construction time. The vertical axis represents the index of the received signal used to create the CSDM.

Applying a singular decomposition to a set of MVDR replicas obtained from

consecutive chirp recordings, as detailed in the previous section and shown on Fig. 5.16, renders the algorithm robust to sound speed fluctuations occurring over a 8 min window. In any case, this adaptive method is just too sensitive to ocean variability to be practical for high frequency scenarios.

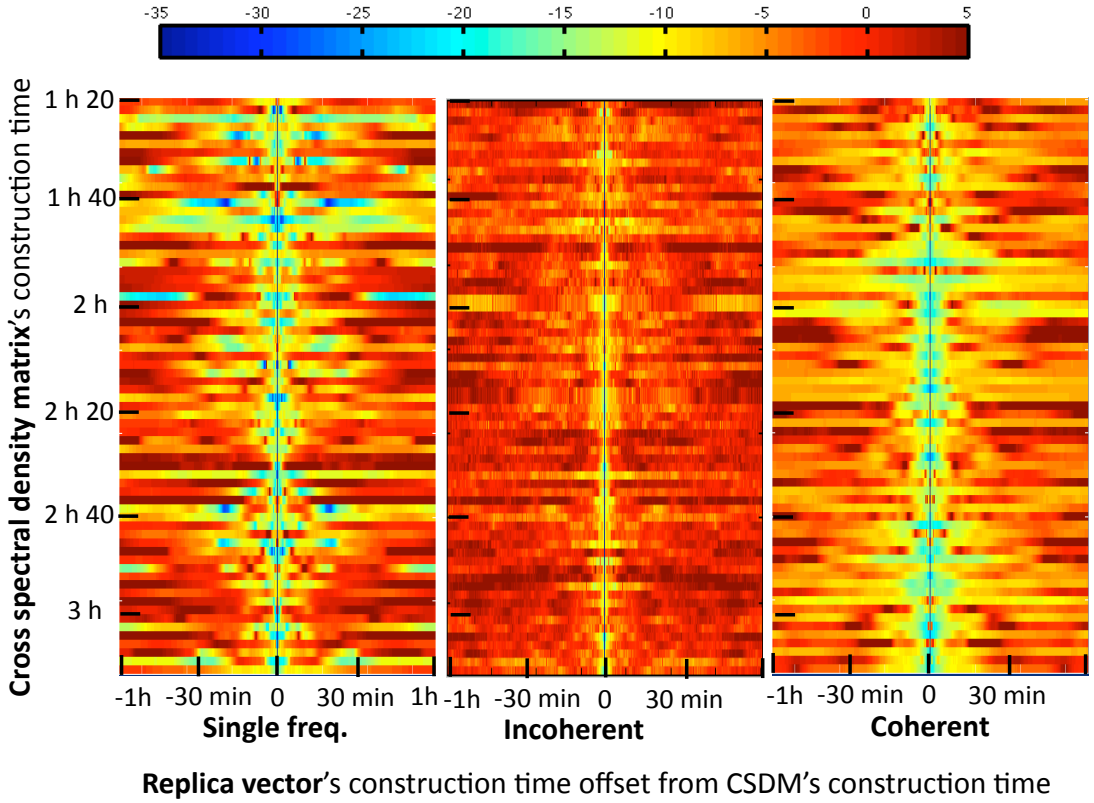

Figure 5.16: Mean sidelobe level in dB obtained with the singular-value-derived narrowband, incoherent and coherent broadband MVDR processors. The horizontal axis represents the width of the replica matrix centered on the CSDM's construction time. The vertical axis represents the index of the received signal used to create the CSDM.

The white noise constraint adaptive method developed by Cox *et al* [13] builds on the MVDR formulation and introduces an inequality constraint on the gain against spatially white noise. This extra-constraint relaxes the super-resolution characteristic of the MVDR along with its requirement for very precise knowledge of the environment.

The new optimization problem is written as:

$$\min_{\boldsymbol{w}} \boldsymbol{w}^H \boldsymbol{R} \boldsymbol{w} \;\; subject\, to \;\; \boldsymbol{w}^H \boldsymbol{d} = 1 \;\; and \;\; \boldsymbol{w}^H \boldsymbol{w} \leq \delta^{-2}, \tag{5.13}$$

which yields:

$$\boldsymbol{w}_{\boldsymbol{wncm}}(r,z) = \frac{(\boldsymbol{R} + \epsilon \boldsymbol{I})^{-1} \boldsymbol{d}}{\boldsymbol{d}^H (\boldsymbol{R} + \epsilon \boldsymbol{I})^{-1} \boldsymbol{d}}. \tag{5.14}$$

The value of ϵ is such that the third inequality of Eq. 5.13 is satisfied.

Figure (5.17) represents the mean sidelobe level obtained using the white noise constraint algorithm. A comparison with Figs. (5.9), (5.10) and (5.11) show that the WNCM's robustness to fluctuations is comparable if not better than the conventional one, but the mean sidelobe level is also 10 to 15 decibels lower.

The SVD technique applied to the WNCM algorithm, shown in Fig. (5.18) surpasses the conventional method by generating a replica vector robust to fluctuations occurring over the whole hour-long window on either side of the CSDM's construction time, in addition to very low sidelobe levels (less than -35 dB).

5.4.5 Investigation of the singular value decomposition method over larger environmental variations

Since the replicas vectors were obtained from recordings on either side of the CSDM's construction time, one can wonder if the same level of robustness could be expected from "averaging" replicas from data not centered on the CSDM's construction time.

To answer this question, the replica vectors used to create the matrix are chosen further and further away from the CSDM's construction time. This time, ten frequencies were used in the study, spanning 2.8 KHz to 3.34 KHz by steps of 60 Hz. The lowest frequency is chosen for the narrowband algorithm.

Figures (5.19) and (5.20) display the mean sidelobe level obtained using narrowband and broadband conventional and WNCM matched-field processors. The CSDM was created from data recorded at time 2h 15 min. The horizontal axis represents the center of the replica window in hours, and the vertical axis the duration of that window. The area on the left of the black dotted line represents

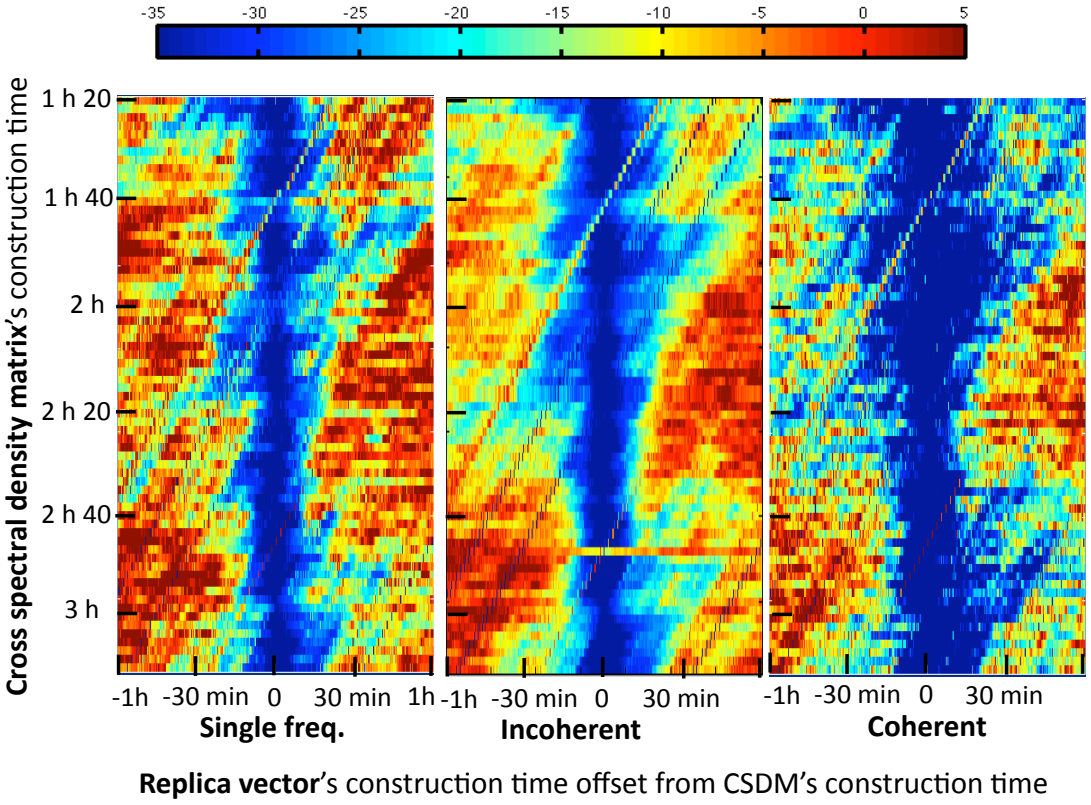

Figure 5.17: Mean sidelobe level in dB obtained with the narrowband, incoherent and coherent broadband WNCM processors. The x-axis represents the width of the replica matrix centered on the CSDM's construction time. The y-axis represents the index of the received signal used to create the CSDM.

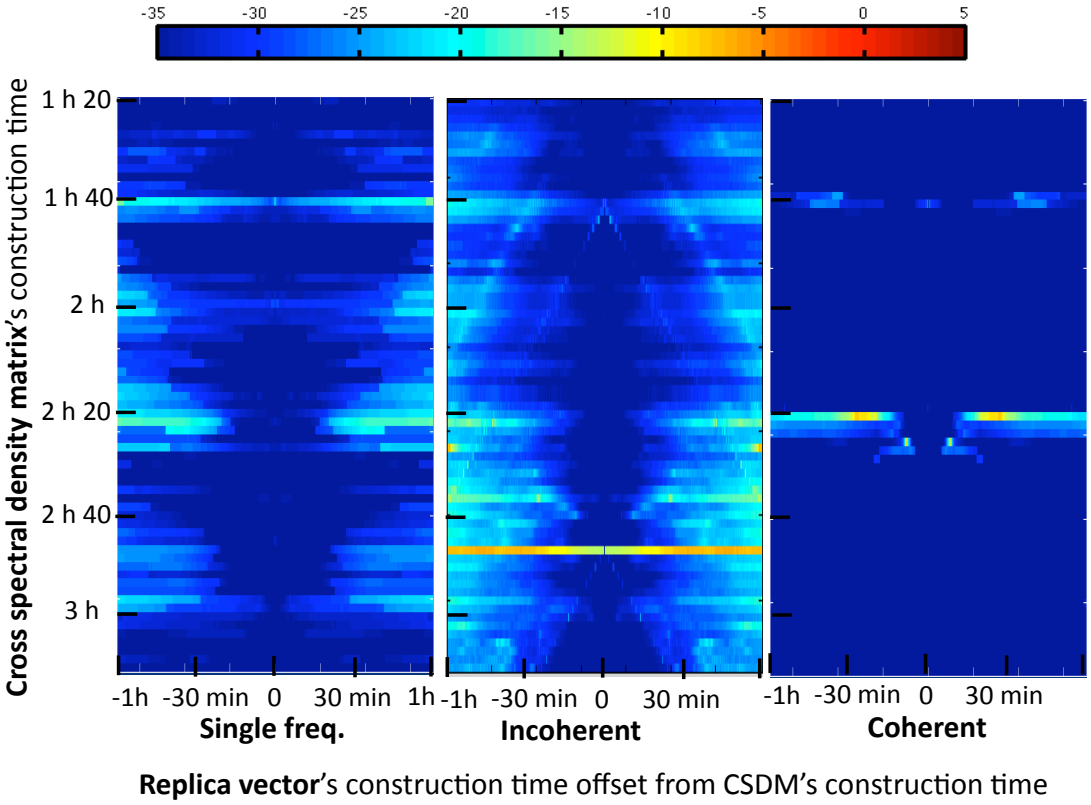

Figure 5.18: Mean sidelobe level in dB obtained with the singular-value-derived narrowband, incoherent and coherent broadband WNCM processors. The horizontal axis represents the width of the replica matrix centered on the CSDM's construction time. The vertical axis represents the index of the received signal used to create the CSDM.

cases for which the CSDM's construction time is contained in the replica time window.

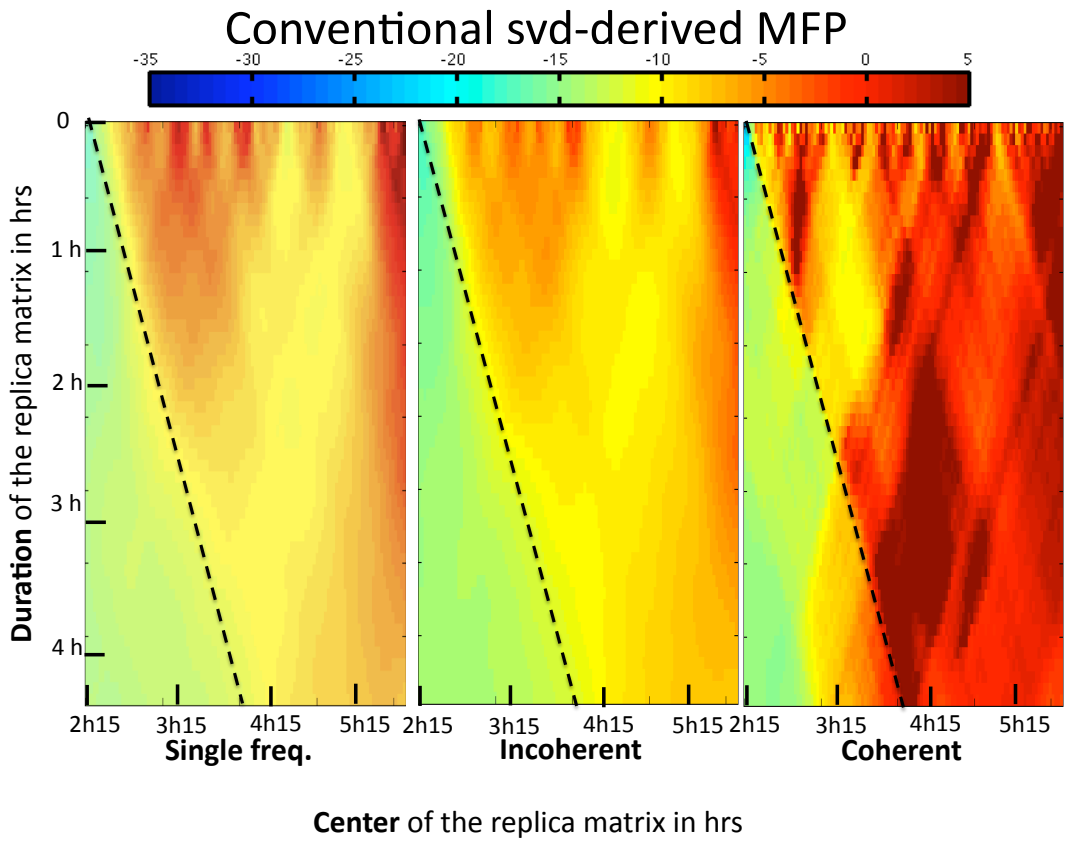

Figure 5.19: Mean sidelobe level in dB obtained with the singular-value-derived narrowband, incoherent and coherent broadband conventional processors.The horizontal axis represents the center of the replica window in hours, and the vertical axis the duration of that window. The area on the left of the black dotted line represents cases for which the CSDM's construction time is contained in the replica time window.

Inspection of the figures shows that for most cases, the SVD technique yields a replica vector robust to sound speed fluctuations even when the "right" ocean is not included in the average. The bigger the replica window, the more stable the result is. As noticed in the previous section, the WNCM is much more stable to ocean's variability than the conventional algorithm. In fact, forming the aver-

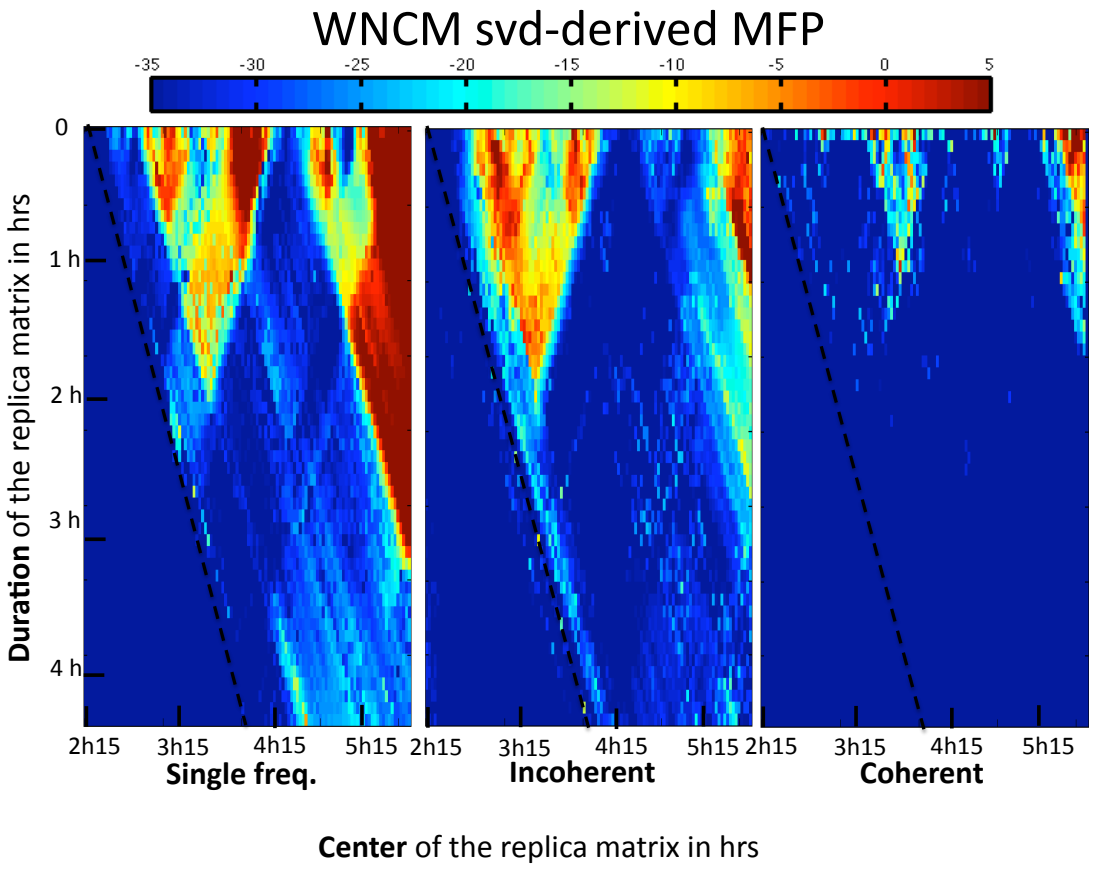

Figure 5.20: Mean sidelobe level in dB obtained with the singular-value-derived narrowband, incoherent and coherent broadband WNCM processors.The x-axis represents the center of the replica window in hours, and the y-axis the duration of that window. The area on the left of the black dotted line represents cases for which the CSDM's construction time is contained in the replica time window.

age of replicas spanning a 2 hour-long window ensures correct localization at any point in time for the broadband methods. An interesting result was obtained with the coherent broadband processor. Indeed, it seems like the replica vectors must be chosen around the CSDM's construction time for the conventional broadband coherent method to successfully localize the source, making it the least robust of the three options, while at the contrary, the coherent broadband WNCM proved to be the most stable of the three to fluctuations.

Using data-derived replica vectors is thus a valuable tool for comparing different algorithm's robustness in scenarios for which creating accurate synthetic replicas is not an option. The coherent broadband WNCM averaged over environments seem to be the most promising technique for high frequency MFP. Would this technique be robust enough to localize a high-frequency source in presence of sound-speed fluctuations and model mismatch?

5.5 High frequency MFP using model derived replica vectors

The FAF-05 data set introduced in Sec. 5.3.2 is used to test the five conventional algorithms. Ten frequencies are processed from 2.8 KHz to 4.14 KHz by increments of 70 Hz. Narrowband results are obtained by processing the lowest frequency.

Conductivity-temperature-depth casts over six hours are used to infer the empirical orthogonal functions (EOF) of the water sound speed. These eigenfunctions provide a description of the spatial and temporal variability of the sound speed profile [31]. They allow us to create eleven sound speed profiles by perturbing the mean profile according to the EOFs of the data. A set of replica fields is then synthesized on the array for each sound-speed perturbed environment. For each grid point in range and depth, the eleven modeled fields on the array incoming from an hypothetical source placed at that grid point are stacked in a replica matrix. A singular value decomposition of the matrix is performed, and the singular vector associated with the highest singular value is kept as the conventional

SVD-derived replica vector.

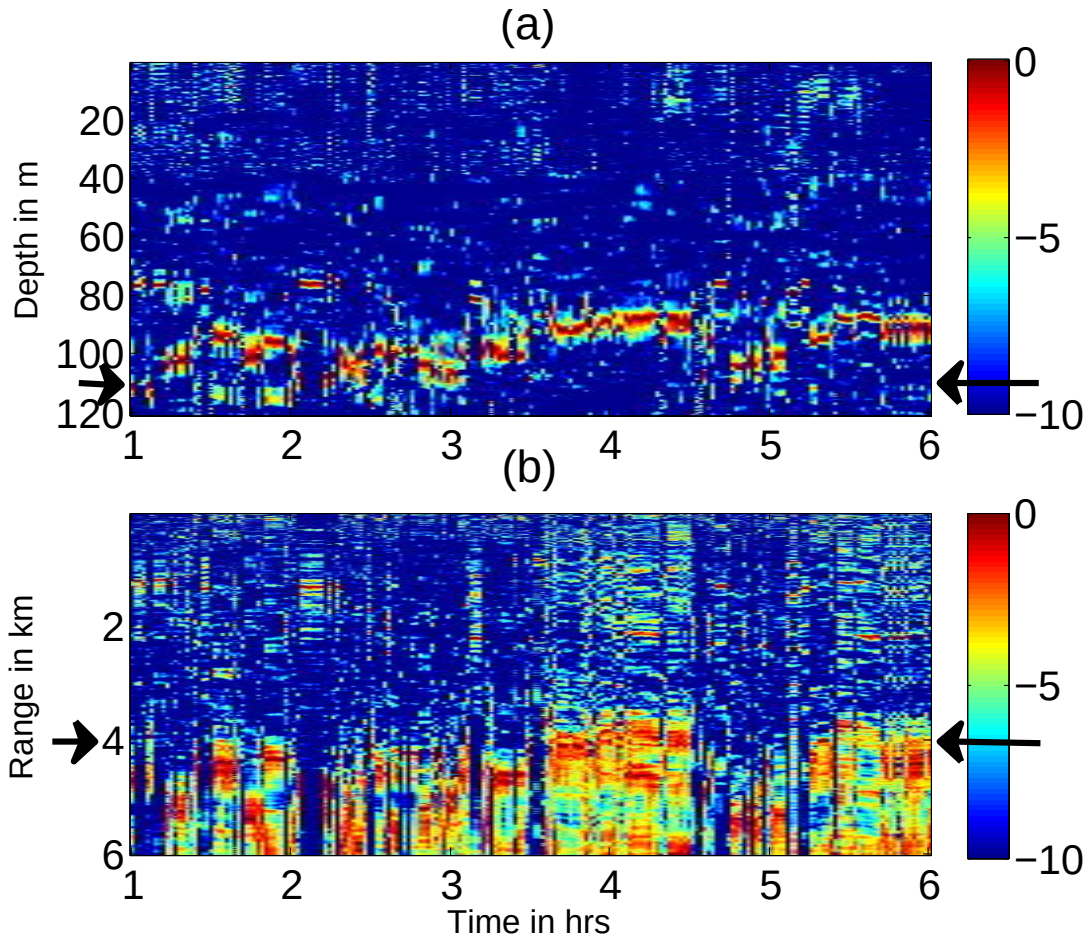

Figure 5.21: Narrowband, SVD-derived conventional MFP's variability over 6 hours from successive recordings of chirps sent by the source 29 every 20 s. (a) and (b) represent the depth and range slices respectively obtained at the main lobe's position as time evolved. The position of the source at 112 m deep and 4 km in range is given by the arrows. Environmental uncertainties prevent the single-frequency svd-derived conventional method from localizing the source.

As in Section 5.3.2, successive recordings are processed to study the narrowband, SVD-derived conventional matched-field processor's tracking performance over a 6 hour-long time window, at 3.5 kHz. Figures (5.21) (a) and (b) represent the depth and range slices obtained at the main lobe position as a function of time.

The position of the source 29 is represented by the arrows, at 112 m deep and 4 km in range. Both traditional in Fig. (5.8) and SVD-based single-frequency in Fig. (5.21) conventional processors do not localize the source at all.

The broadband incoherent and coherent conventional MFP are now implemented, and the results obtained are displayed in Figs. (5.22) and (5.23). Processing multiple frequencies, especially coherently is essential to high-frequency MFP, since the source is now localized 14 % of the time for the incoherent case (corresponding to 50 minutes) and 29 % of the time (or 1h 45 minutes) for the coherent broadband one.

The last step consists in combining broadband methods with the SVD technique. Figures (5.24) and (5.25) respectively show the incoherent and coherent SVD-derived MFP's output. Performing a singular value decomposition over replicas from perturbed environments enhances conventional incoherent MFP's tracking performance at high frequency. The source is localized 32% of the time (or in other words for 2 hours out of the 6 hours processed) versus 14% (or 50 minutes) without application of the SVD technique. In the coherent broadband case, the percentage of successful localization did not vary between the SVD and non-SVD derived conventional algorithms.

It is interesting to note that the data frames leading to successful source localization are not necessarily contiguous. Indeed, in the incoherent broadband SVD-derived case, presented on Fig. (5.24), the source is localized over most of the first hour, then again twenty-five minutes later for another twenty minutes, and finally four hours later for a little more than half an hour. This suggest the presence of cyclical perturbations in between which the ocean returns to its original state. Extending the study over longer periods of time would be necessary to gain more insight on the nature of the sound-speed fluctuations.

While still problematic, MFP's localization performance at high-frequency is improved by the use of robust broadband processing techniques and by performing a singular value decomposition over replicas coming from sound speed perturbed environments.

However, another more forgiving but of importance application of MFP is

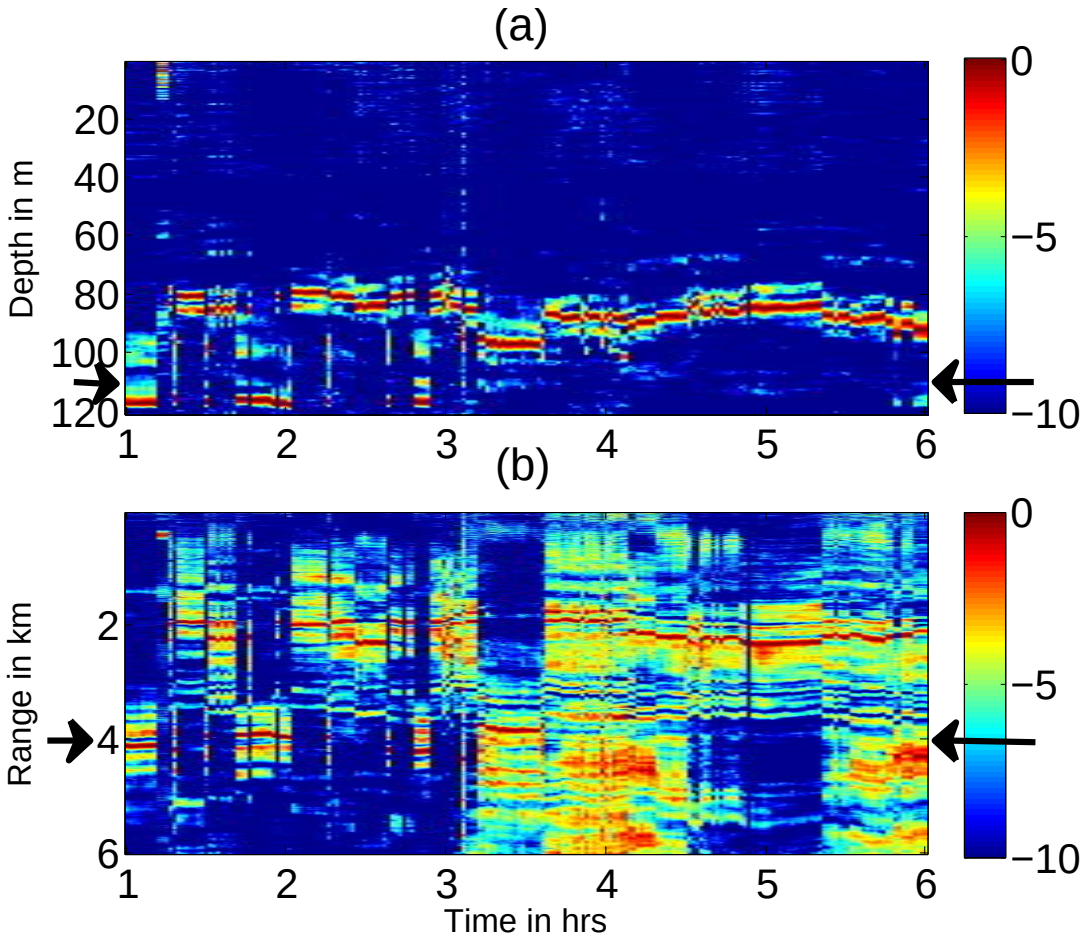

Figure 5.22: Incoherent broadband conventional MFP's variability over 6 hours from successive recordings of chirps sent by the source 29 every 20 s. (a) and (b) represent the depth and range slices respectively obtained at the main-lobe position as time evolved. The position of the source at 112 m deep and 4 km in range is given by the arrows. The source is successfully localized 14% of the time, which corresponds to 50 minutes.

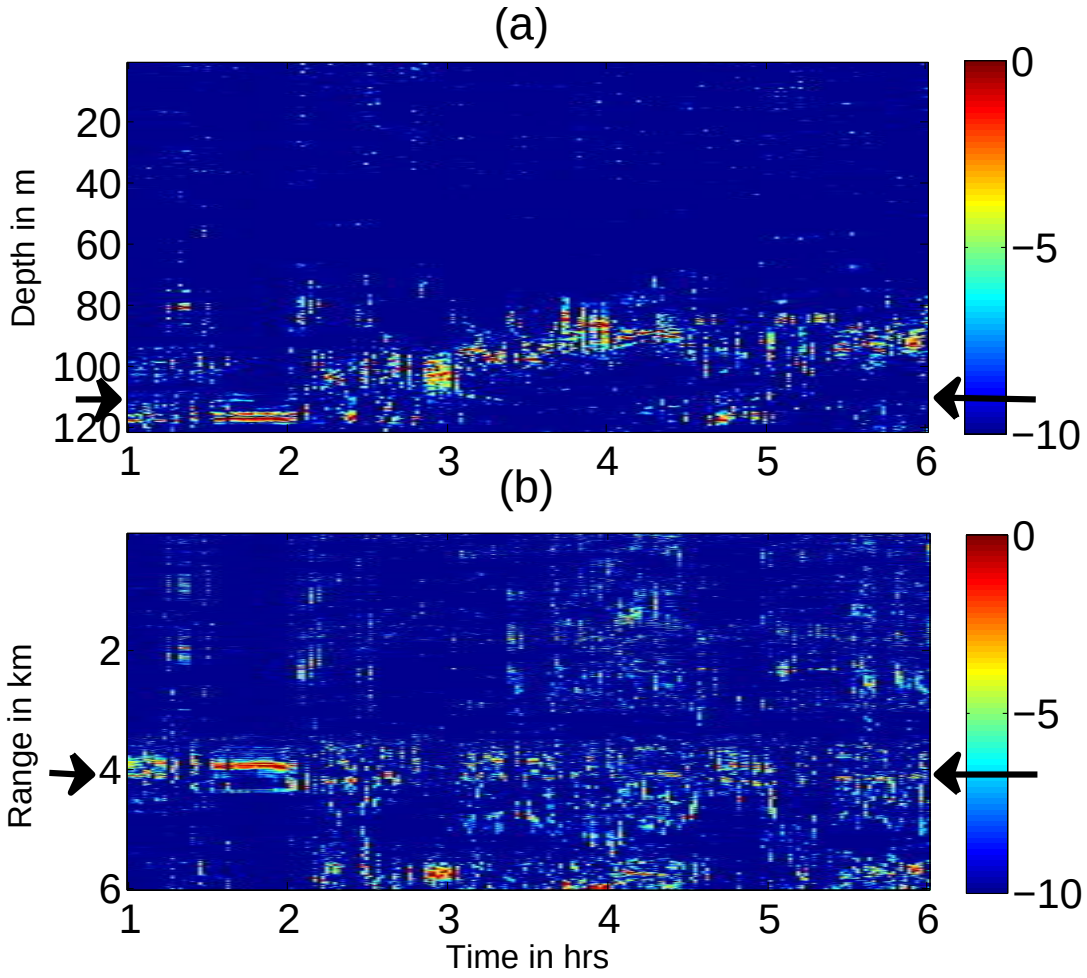

Figure 5.23: Coherent broadband conventional MFP's variability over 6 hours. (a) and (b) represent the depth and range slices respectively obtained at the main lobe position as time evolved. The position of the source at 112 m deep and 4 km in range is given by the arrows. The source is successfully localized 29% of the time, which corresponds to 1h 45 minutes.

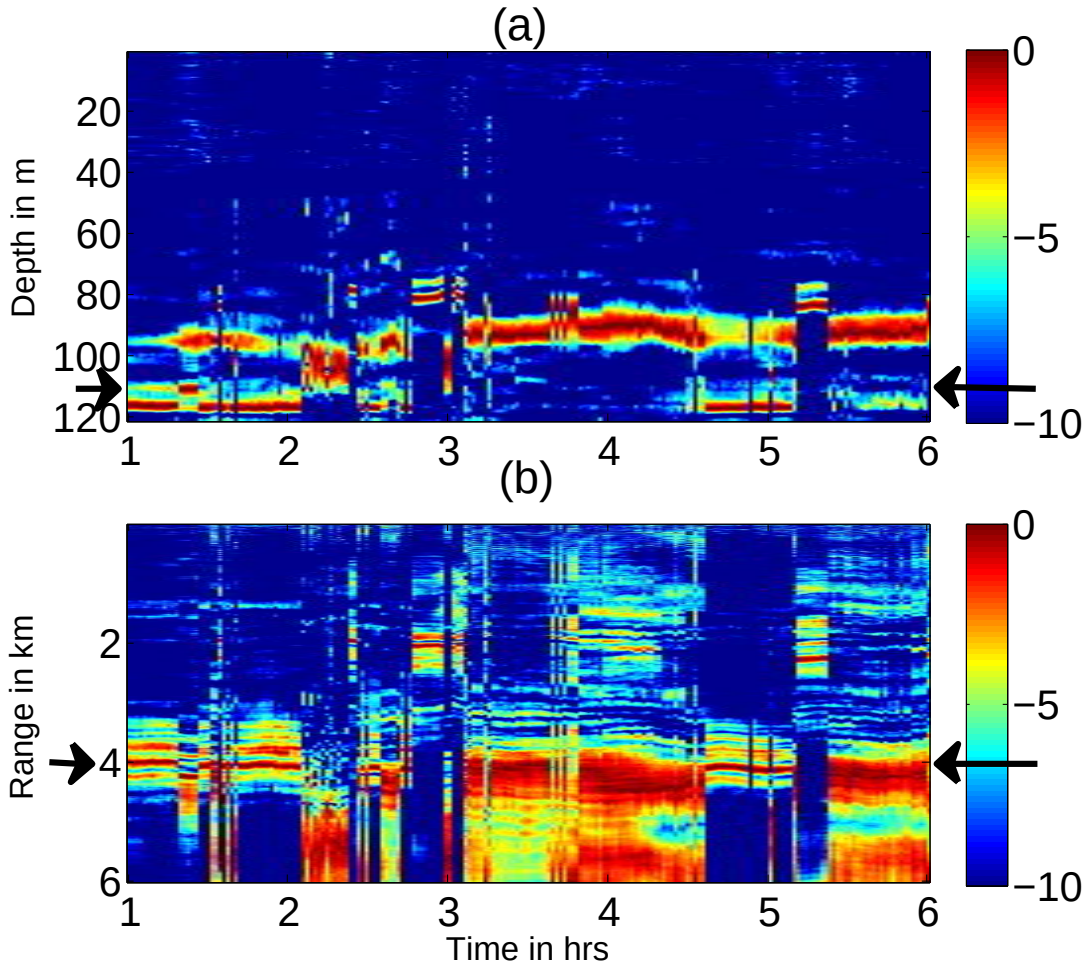

Figure 5.24: Incoherent broadband SVD-derived conventional MFP's variability over 6 hours from successive recordings of chirps sent by the source 29 every 20 s. (a) and (b) represent the depth and range slices respectively obtained at the main lobe position as time evolved. The position of the source at 112 m deep and 4 km in range is given by the arrows. The source is successfully localized 32% of the time, which corresponds to 2 hours.

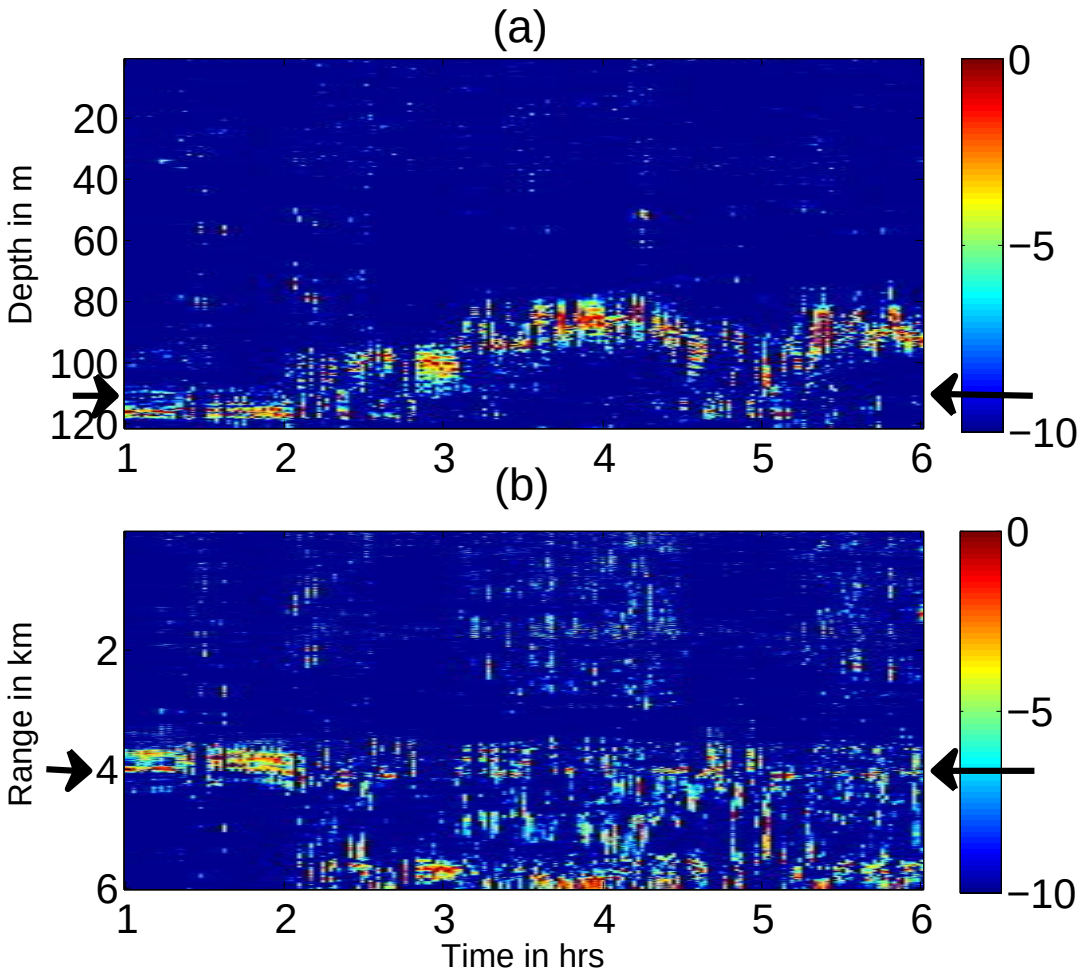

Figure 5.25: Coherent broadband SVD-derived conventional MFP's variability over 6 hours from successive recordings of chirps sent by the source 29 every 20 s. (a) and (b) represent the depth and range slices respectively obtained at the main lobe position as time evolved. The position of the source at 112 m deep and 4 km in range is given by the arrows. The source is successfully localized 29% of the time, chich corresponds to 1h 45 minutes.

the classification of sources into the categories submerged versus non-submerged, along with an estimate of the distance between receivers and sources. Applying simple narrowband, incoherent or coherent conventional MFP shown on Figs. (5.8), (5.22) and (5.23) is enough to confirm that the source sits deeper than 80 m in the water column, but not enough to get a range estimate of the target. In contrast, the SVD-derived technique shown in Figs. (5.21), (5.24) and (5.25) exhibits considerably better ranging capability since the source is shown at 4 km away from the receiver over most of the six hour-long window, along with the fact that it is submerged deeper than 80 meters.

5.6 Summary and conclusion

Source localization at high frequency is typically problematic because of the increased sensitivity of processors to model inaccuracies and environmental variability. The performance of various frequency-domain matched-field processing techniques was evaluated on experimental data in the best case scenario of mismatch-free environment. Because the experimental setup featured 29 sources emitting chirps successively over an 8 hour-long window while an array of hydrophones 4 km away recorded the signal continuously, it was possible to use the data emitted from various sources at different times to construct replica vectors, and investigate the processor's mean sidelobe level as a function of time. Hence, the only variables fluctuating in the system between the replica and cross-spectral density matrix's construction time were the source and receiver elements position and the water sound speed between the arrays. It was found that exploiting the information across frequency, especially in a coherent way and using a robust adaptive technique like the white noise constraint method is essential to perform a successful localization at high frequencies. Replicas obatined from successive recordings were also "averaged" using a singular value decomposition technique to extract the most stable features of the ensemble of replicas. Doing so increased considerably the robustness of algorithms to sound speed fluctuations, rendering the coherent broadband white noise constraint processor robust to fluctuations

occurring during a several hour-long time window.

The same techniques were then applied to traditional model-based conventional matched-field processing. A set of replica vectors was generated using a simplified range-independent environment and sound-speed profiles perturbed according to the EOF of the data. The results obtained are consistent with those provided by data-derived replica vectors. The combination of incoherent broadband processing and the SVD technique localizes the source 32% of the time, or two hours over a six hours long window, while the narrowband equivalent fails to localize it on the entire window. Most techniques were found to differentiate between surface or submerged targets, but only application of the SVD technique gave an accurate range estimate over most of the window. However, this enhancement in performance comes at the cost of processing time, since each degree of complexity (adaptive versus conventional, broadband versus narrowband, coherent versus incoherent, multi-environments versus single-environment) increases the number of calculations to perform.

5.7 Acknowledgments

This work was funded by ONR.

The text of this chapter is a full reprint of the material of the material soon to be submitted to the J. Acoust. Soc. Am., Claire Debever and William A. Kuperman "Mitigating the effect of environmental fluctuations on higher frequency matched-field processing". The dissertation author was the primary researcher and author, and the co-author listed in this publication directed and supervised the research which forms the basis for this chapter.

Bibliography

[1] F. B. Jensen, W. A. Kuperman, M. B. Porter, and H. Schmidt. *Computational Ocean Acoustics*. Springer-Verlag New York, Inc., 2000.

[2] D. H. Johnson and D. E. Dudgeon. *Array signal processing*. Prentice Hall signal processing series, 1993.

[3] A. B. Baggeroer, W. A. Kuperman, and P. N. Mikhalevsky. An overview of matched field methods in ocean acoustics. *IEEE Journal of Oceanic engineering*, 18(4):401–424, october 1993.

[4] Renhe Zhang, Zhenglin Li, Jin Yan, Zhaohui Peng, and Fenghua Li. Broadband matched-field source localization in the east china sea. *Journal of Oceanic Engineering, IEEE*, 24(4):1049–1054, October 2004.

[5] G. C. Chen and W. S. Hodgkiss. Vlf source localization with a freely drifting acoustic sensor array. *Journal of Oceanic Engineering, IEEE*, 18, issue 3:209–223, July 1993.

[6] P. Hursky, M. B. Porter, and M. Siderius. High frequency (8-16 hz) model-base source localization. *J. Acoust. Soc. Am.*, 115:3021–3032, 2004.

[7] cristiano Soares, Martin Siderius, and Sergio M. Jesus. Source localization in a time-varying ocean waveguide. *J. Acoust. Soc. Am.*, 112(5):1879–1889, Nov 2002.

[8] A. Tolstoy. *Matched Field Processing for Underwater Acoustics*. World Scientific, Singapore, 1992.

[9] J. N. Maksym. A robust formulation of an optimum cros-spectral beamformer for line arrays. *J. Acoust. Soc. Am.*, 65(4):971–975, April 1979.

[10] H. S. Schmidt, A. B. Baggeroer, W. A. Kuperman, and E. K. Scheer. Environmentally tolerant beamforming for high-resolution matched-field processing: Deterministic mismatch. *J. Acoust. Soc. Am.*, 73:813–825, 1979.

[11] J. L. Krolik. Matched-field minimum variance beamforming in a random ocean channel. *J. Acoust. Soc. Am.*, 92:1408–1419, 1992.

[12] J. V. Candy and J. Sullivan. Model-based identification: An adaptive approach to ocean-acoustic processing. *IEEE Journal of Oceanic engineering*, 21:273–289, 1996.

[13] H. Cox, R. M. Zeskind, and M. M. Owen. Robust adaptive beamforming. *IEEE Transactions on Acoustics, Speech and Signal Processing*, 35(10):1365–1376, October 1987.

[14] A. B. Baggeroer, W. A. Kuperman, and H. Schmidt. Matched-field processing: Source localization in correlated noise as an optimum parameter estimation problem. *J. Acoust. Soc. Am.*, 83:571–587, 1988.

[15] N. Booth and P. Schey. Broadband matched-field processing of low level signals in shallow water. *J. Acoust. Soc. Am.*, 97:3291 (A), 1995.

[16] W. S. Hodgkiss, K. H. Kim, J. J. Murray, and J. L. Krolik. Robust mfp processor performance with swellex data. Esquimalt Defense Research Detachment, Victoria, BC, 12-14 June 1996. presentation at the 8th International Workshop on MFP and Model-Based Signal Processing.

[17] C. S. Clay. Optimum time domain signal transmission and source localization in a waveguide. *J. Acoust. Soc. Am.*, 81:660–664, 1987.

[18] C. S. Clay and S. Li. Optimum time domain signal transmission and source localization in a waveguide: Matched filter and deconvolution experiments. *J. Acoust. Soc. Am.*, 83:1377–1383, 1988.

[19] S. Li and C. S. Clay. Optimum time domain signal transmission and source localization in a waveguide: Experiments in an ideal wedge waveguide. *J. Acoust. Soc. Am.*, 82:1409–1417, 1987.

[20] E. K. Westwood. Broadband matched-field source localization. *J. Acoust. Soc. Am.*, 91(5):2777–2789, May 1992.

[21] S. P. Czenszak and J. L. Krolik. Robust wideband matched-field processing with a short vertical array. *J. Acoust. Soc. Am.*, 101(2):749–759, February 1997.

[22] Z.-H. Michalopoulou and M. B. Porter. Matched-field processing for broadband source localization. *IEEE Journal of Oceanic engineering*, 21:384–392, 1996.

[23] Z.-H. Michalopoulou. Robust multi-tonal matched-field inversion: A coherent approach. *J. Acoust. Soc. Am.*, 104:163–170, 1998.

[24] Claire Debever and W. A. Kuperman. Robust matched-field processing using a coherent broadband white noise constraint processor. *J. Acoust. Soc. Am.*, 122 (4):1979–1986, October 2007.

[25] Zhenglin Li, Guihua Ji, and Qiongxing Dai. temporal correlation of mfp with the presence of internal waves (a). *J. Acoust. Soc. Am.*, 123(5):3589, May 2008.

[26] J. M. Ozard, M. L. Yeremy, and M. A. Price. Simulations and efficient prediction of matched-field processing degradation from mismatch in shallow water (a). *J. Acoust. Soc. Am.*, 95(5):2980–2980, May 1994.

[27] P. Roux, W. A. Kuperman, W. S. Hodgkiss, H. C. Song, T. Akal, and M. Stevenson. A non-reciprocal implementations of time reversal in the ocean. *J. Acoust. Soc. Am.*, 116:1009–1015, 2004.

[28] M. B. Porter. The kraken normal mode program. Technical report, SACLANT Undersea Research Center, November 1992.

[29] P. Roux, B. D. Cornuelle, W. A. Kuperman, and W. S. Hodgkiss. The structure of raylike arrivals in a shallow-water waveguide. *J. Acoust. Soc. Am.*, 124:3430–3439, 2008.

[30] H. L. Van Trees. *Optimum Array Processing, part IV of Detection, Estimation, and Modulation Theory.* Wiley-interscience, 2002.

[31] W. J. Emery and R. E. Thomason. *Data Analysis Methods in Physical Oceanography.* Elsevier, New York, 2nd and revised ed. edition, 2001.

Chapter 6

Conclusions and Future Work

6.1 Conclusions

Matched-field processing (MFP) is a promising passive technique to localize and track submerged acoustic sources in complex, noisy environments. However, its lack of robustness to an assortment of important scenarios has made it problematic. In this thesis we have extended the viability of MFP for some of these difficult scenarios. Further, an alternative but important metric for MFP is its potential ability to find the range of a source while simultaneously determining whether or not it is submerged. For this latter, relaxed requirement, the results of this thesis indicate that MFP is a viable processing method for operational applications.

While known to be successful in favorable scenarios, the technique's performance is impaired by a number of factors. Experimental data featuring these characteristic have been isolated for the purpose of studying and improving MFP's performance. These limiting factors can be summarized as follows:

1. Presence of environmental mismatch. A good knowledge of the water channel and sediment properties, array elements' location, sufficient aperture and use of adequate propagation model are essential to reproduce the signal received on the array with enough accuracy to allow a coherent summation of the complex fields at the output of the processor. This is especially important in high-frequency scenarios for which the sound propagation becomes increasingly sensitive to smaller features or variability in the waveguide.

2. Snapshot deficiency. When the target of interest or loud interferers are moving across resolution cells faster than the time required to accumulate a sufficient number of snapshots (at least twice the number of elements), the cross-spectral density matrix (CSDM) is not full rank, hence not invertible. This is problematic for adaptive algorithms whose formulation involves the CSDM's inverse matrix.

3. Low signal-to-noise ratio. A certain amount of gain dependent on the number of elements in the array and the processor implemented is available to localize weak sources buried in noise. When the signal's power drops below a threshold, MFP's detection performance declines abruptly.

4. Higher frequencies. As the emitted signal's frequency increases, so does the sensitivity of the algorithm to model inaccuracies or environmental fluctuations, like sound-speed profile's perturbation by internal waves for example. The sound propagation is altered by features roughly the size of its wavelength.

The contributions of this dissertation can be classified broadly into the following three parts.

6.1.1 Localizing low signal-to-noise ratio sources

Most of this thesis work from Chapter 2 to 4 is devoted to the development of a processor able to localize weak sources buried in noise. The main contributions and accomplishments are listed below:

- Investigating ways to increase the gain at the output of the processor without increasing the size of the array led to the use of coherent broadband MFP. The coherent methods available in the literature were reviewed and the semi-coherent one developed by Michalopoulou and Porter was chosen as basis for this Ph. D. work.

- Localization and tracking performance of the semi-coherent processor combined with conventional, minimum variance and white-noise constraint methods was compared to the narrowband and incoherent broadband processors, using simulated and experimental data. It was found that processing the frequencies coherently increased the dynamic range between the main lobe and the background level at the output of the processor.

- A technique was developed to extract the unknown frequency-dependent phases of the source's signal spectrum from the data itself. The semi-coherent algorithm was then modified to include those phases in the reconstitution of the pressure fields, making it a fully-coherent algorithm.

- The extra processing gain provided by the fully-coherent method versus semi-coherent and incoherent as a function of number of frequencies included in

the processing was evaluated using theory and simulation. The fully-coherent algorithm was found to have an extra processing gain equal to the number of frequencies over the incoherent one. The semi-coherent algorithm, on the other hand provides a gain in between the incoherent and fully-coherent's one, depending on the value of the SNR at each element. The higher the input SNR, the closer the semi-coherent gain is to the fully-coherent one.

- The detection index metric was introduced to compare the processors' ability to detect a weak source. Its evolution versus input SNR at each array element was computed using simulated and experimental data. The fully-coherent algorithm displayed a detection index ten decibels larger than the narrowband one at all input SNRs, five decibels larger than the incoherent one and between zero and ten decibels larger than the semi-coherent one. The fully-coherent method was also found experimentally to detect and localize sources up to ten decibels weaker than the other broadband algorithms.

6.1.2 Mitigating model mismatch and snapshot deficiency

Chapters 2, 3 and 5 introduce the adaptive white noise constraint processor to enhance MFP's robustness to model mismatch, environmental fluctuations and mitigate the snapshot deficiency issue.

- The increased sensitivity of coherent broadband processing to model mismatch and sound speed variability was recognized. The larger data space due to the incorporation of cross-frequency terms also comes with a bigger snapshot requirement. The white noise constraint method, typically used for narrowband processing, is applied to the semi-coherent algorithm to mitigate those two issues.

- When the sources and interferers' motion prevent the acquisition of a sufficient number of snapshots, the semi-coherent white noise constraint algorithm was shown to exhibit a dynamic range bias. This bias was shown to be consistent with that previously presented in the literature for a single-frequency.

6.1.3 Improving higher frequency matched-field processing

Chapter 5 is considering the extreme case of MFP at high frequency (above 1 kHz), for which small environmental fluctuations and model mismatch are usually problematic.

- A technique is developed to compare algorithms' robustness to fluctuations in the propagation medium using experimental data only, implementable whenever multiple sources are emitting a signal successively and a receiver array is recording them over an extended period of time. Data itself is used to create replica vectors, allowing a study of the mean sidelobe level as a function of time between the data used to create the replica vector and the cross-spectral density matrix's construction time.

- The data-derived weight vector technique confirmed the fact that the white noise constraint method is considerably more robust to environmental fluctuations than the minimum variance one since it successfully localizes the source for about twenty minutes on either side of the cross-spectral density matrix's construction time, versus a couple minutes in the minimum variance algorithm's case. A comparison with the conventional algorithm shows that the white noise constraint is a little more robust to sound speed fluctuations, and features a better detectability of the signal by lowering the mean sidelobe level by ten to fifteen decibels. Using a semi-coherent type of processor increased the dynamic range between main lobe and sidelobe levels, but did not provide an improvement in robustness to environmental variability in the conventional and minimum variance case. However the combination of semi-coherent processing and white noise constraint method decreases the sensitivity of the algorithm to fluctuations in comparison to narrowband and incoherent broadband processing. Localization is found stable over thirty minutes on either side of the cross-spectral density matrix's construction time.

- A singular value decomposition method over perturbed environments is also introduced in the construction of the "data weight vector" in an effort to

further mitigate the effect of fluctuations. It involves concatenating replicas vectors obtained from continuous recordings into a replica matrix, evaluating the singular value decomposition of the matrix, and extracting the singular vector corresponding to the highest singular value as the "perturbation-averaged" replica vector. Doing so was found to considerably increase the robustness of the conventional and white noise constraint algorithms. Its application to the semi-coherent broadband white noise constraint algorithm was especially beneficial since the localization was found stable over more than four hours.

- The results obtained with the data-derived weight vector approach are applied to the traditional model-derived one. It was found that incoherent broadband processing combined with the SVD technique improved localization at high frequency. The source is now localized 32% of the time, or two hours out of the six hour-long window, while the narrowband processor does not localize the source at all.

6.2 Future Work

This section contains some of the possible extensions to the work done throughout this dissertation.

- The white noise constraint method combined with the semi-coherent processing technique was shown to increase the dynamic range at the output of the processor, enhancing the source's detectability over noise and interferers. Also, extracting the signal's spectrum phases and incorporating them in the semi-coherent processing allowed detection of weaker sound sources. Combining both methods by implementing a fully-coherent broadband white noise constraint processor, not done in this study because of the larger processing time associated would be of interest.

- In this dissertation, various promising modifications are applied to the basic MFP algorithm as going from narrowband to broadband processing, from

incoherent broadband to semi-coherent then fully-coherent broadband processing, from conventional to adaptive methods and finally implementing a singular value decomposition technique over perturbed environments. Each of those additions comes with an extra computational burdens, rendering the combination of all too computationally intensive for practical applications. Therefore a useful if not necessary addition to this work would be to increase the computational efficiency of the processing to make it more applicable to near real time source tracking.

- Additional investigation of the optimal number and spread of frequencies versus input signal-to-noise ratio and bandwidth available would improve the efficiency of coherent broadband methods. Indeed, selecting too few frequencies or closely spaced frequencies would not take full advantage of the coherent method's added processing gain. Selecting too many frequencies would eventually decrease the spread between frequencies such that little additional information would be inputted in the processor per frequency.

- The technique developed in this dissertation to extract the frequency-dependent source's spectrum phases from the data involves a slow alteration of the cross-spectral density matrix for each grid point in range and depth. Investigating a more efficient or elegant way to access those phases would make the technique more suitable to near real-time applications.

- Finally, the computationally expensive assessment of the "singular-value derived" coherent broadband white noise constraint processor's robustness to environmental fluctuations in high frequency scenarios could be performed using a synthetic environment to generate the replica vectors.